Charge Storage Mechanisms of High Surface Area Carbides and Nitrides for Supercapacitors

by

Abdoulaye Djire

A dissertation submitted in partial fulfillment
of the requirements of the degree of
Doctor of Philosophy
(Chemical Engineering)
in the University of Michigan
2016

Doctoral Committee:

Professor Levi Theodore Thompson Jr., Chair
Professor Mark A. Barteau
Professor James E. Penner-Hahn
Professor Timothy Scott

Dedication

To my parents Lassana Djire and Mama Sissoko

Acknowledgements

First and foremost, I would like to thank my advisor and mentor, Professor Levi Thompson for everything he has done for me. Levi saw my potential, and challenged me in every way to become a better scientist and engineer. As he always says, advising and mentoring a student is like making a sauce, and never to serve it until it's done and ready to be served. Thank you for the time and effort you have invested in preparing me for the world. I shall carry on your legacy!

I must also thank Dr. Alice Sleightholme, Dr. Krista Hawthorne, Professor Emeritus Paul Rasmussen, Dr. Saemin Choi, Dr. Jason Siegel, Dr. Aniruddha Deb, Dr. Lilin He, Dr. Priyanka Pande, and Dr. Jason Gaudet for their help and mentoring. I owe to them what I have achieved during my PhD. I would also like to thank the students that I worked with, whom have contributed to this project. These include Olabode Ajenifujah, Jean Yves Ishimwe, Shintaro Oyama, and Avery Jones.

Also, I would like to thank members of my dissertation committee: Prof. Penner-Hahn, Prof. Barteau, Prof. Scott, and Prof. Monroe. I am most grateful for the opportunity of working and interacting with each one of you. I thank Prof. Penner-Hahn for his help and guidance with X-ray absorption spectroscopy and solid-state electrochemistry. I am thankful to Prof. Barteau for his valuable contribution to the dissertation and for all the recommendation letters he has written for me. When I found out that I needed one more faculty for my committee, I knew it had to be Prof. Scott.

Thank you for the help and inspiration. I would like to thank Prof. Monroe for his help and guidance. Prof. Monroe taught me the fundamentals of electrochemistry, and for that, I am most grateful.

I would like to thank the talented students from the Thompson research group. These include all former and present members. My professional and social interactions with them have helped me in becoming a better researcher, colleague, and friend.

This dissertation work would not be possible without the help from my funding sources, including Army Tank Command, Army Research Office, the Automotive Research Center, and the University of Michigan Energy Institute. Thank you for the opportunity.

I also would like to thank all the staff from the Chemical Engineering department. Thank you for your help and assistance. I greatly appreciated it.

Last but not least, I would like to dedicate this dissertation to my mother, the bravest, kindest, nicest, and most generous woman I have ever known. Thank you Mama for everything. To my father, Djire, you are my hero. And to my brothers and sisters, I could not wish for better siblings. Thank you guys for the support and love always. Finally, to my fiancée, Fatoumata, thank you for being there for me. You make me better.

Table of Contents

List of Figures

List of Tables

Chapter 1

Introduction

1.1. Motivation

As of March 2016, the world population has reached 7.4 billion people and is estimated to reach 11.2 billion by 2100 [1], and is consuming energy each and every second [2-4]. Energy has become central to modern day life [5]. The current worldwide electric generation capacity is estimated to be 23 terawatt hours [5,6]. Approximately 68% of today's electrical energy is supplied from fossil fuels: coal (42%), natural gas (21%), oil (5%), nuclear (14%), hydro (15%), and the remaining 3% from renewable energy technologies [2]. The worldwide electricity demand is increasing at a faster pace than overall energy consumption and is predicted to double by the middle of the century and triple by the end of the century [7-10]. Coal has been the dominant source of electricity generation in the world [7-10]; abundant coal reserves may maintain current consumption levels longer than oil and gas. However, every kWh of electricity generated by burning coal coproduces an average 1000 g lifecycle CO_2 emission, a greenhouse gas that is widely considered as the primary contributor to global warming [8]. In the United States alone, coal power plants emit 1.5 billion tons of CO_2 per year, and emissions from developing countries are accelerating [8]. Despite the abundance of coal, there are hundreds of millions of people in the world that do not have access to a constant source of energy [9]. The environmental concerns over the use of fossil fuels and their resource

constraints, combined with energy security concerns, have stimulated great interest in generating electrical energy from renewable sources such as solar and wind [7,8], as well as the development of electric vehicles or hybrid electric vehicles with low CO_2 emissions [11,12]. Because the sun does not shine during the night, wind does not blow on demand and we all expect to drive our car with at least a few hours of autonomy, energy storage systems are starting to play a major role in our lives. At the forefront of these are electrical energy storage systems, such as batteries and electrochemical supercapacitors [13-21]. Batteries have been the energy-storage technology of choice for most applications including portable electronics and electric vehicles because they can convert large amounts of stored chemical energy into electrical energy in a relatively small volume and weight, and provide suitable levels of power [19-21]. Lithium-ion batteries exhibit the highest performance in terms of energy density that can reach up to 180 Wh kg^{-1} [19-21]. However, the lower power density (0.1 kW kg^{-1}) and short cycle life caused by slow kinetic, transport limitations, and structural degradation of the electrode materials have become problems for batteries [13-17]. Faster and higher-power energy storage systems are needed in a number of applications ranging from portable electronics to hybrid electric vehicles and large industrial equipment, and this role has been assigned to electrochemical supercapacitors.

Electrochemical supercapacitors are being developed as an alternative and complementary technology to batteries. As shown in Figure 1.1, supercapacitors offer high power densities (up to 15 kW kg^{-1}) [18-21], long cycle life (can be more than 1,000,000 cycles) [18-21], and moderate energy densities (5 Wh kg^{-1}) [18-21]. They fill the gap between conventional capacitors (which have high power densities) and batteries

(which have high energy densities), and can be used in conjunction with the primary energy-storage devices to minimize stresses by managing short, high power pulses [18-26].

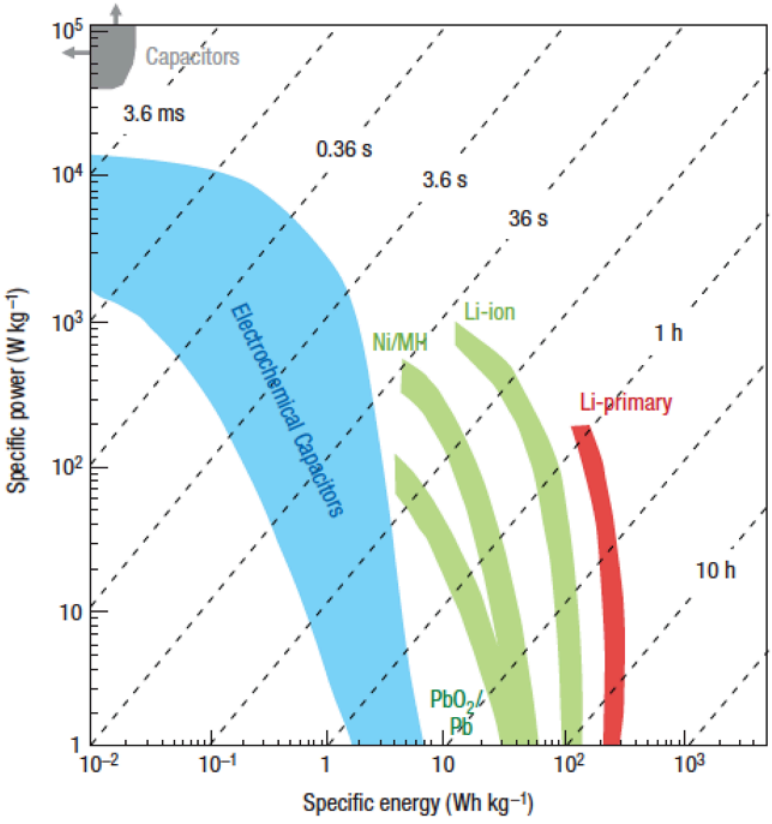

Figure 1.1: Ragone plot: power density versus energy density for various electrochemical energy storage systems, from reference 20.

Supercapacitors are attractive for use in a number of applications including back-up devices, portable electronics, uninterruptible power supplies, electrified vehicles, and large-scale grid energy storage [20-24]. Supercapacitors also find applications in regenerative braking for cars and trucks, expanding the functionality of consumer products such as gaming and multitasking, and buffering the peak power associated with renewable energy sources such as wind turbines [25,26]. There are also a number of

defense applications ranging from powering devices for the modern soldier to electromagnetic armor [25,26].

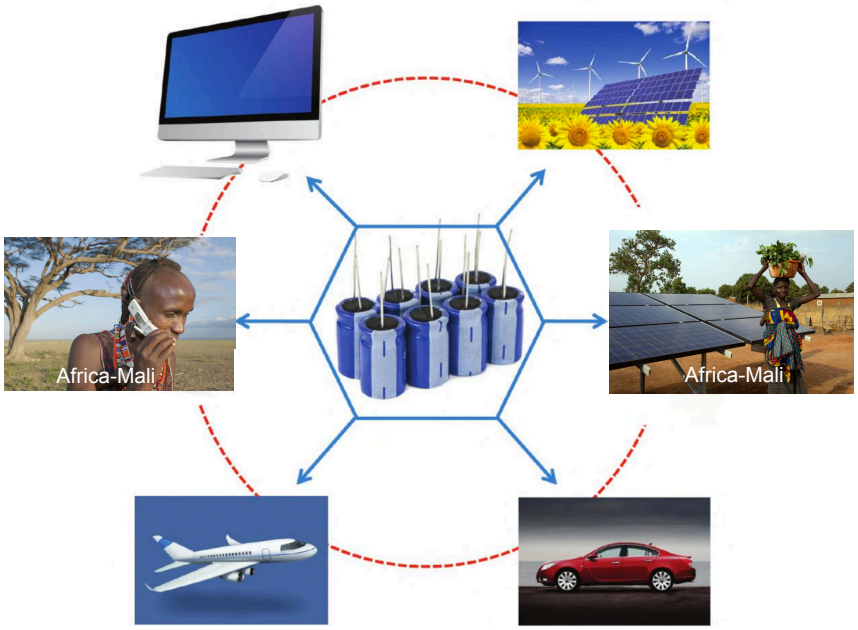

Figure 1.2: Electrochemical supercapacitors applications, adapted from reference 18.

Currently, the high cost ($2,400 to $6,000 per kWh of energy storage compared to $500 to $1,000 per kWh for lithium-ion batteries) and moderate energy density of supercapacitors limit their use [27-31]. Research in this field has focused on increasing energy density without sacrificing cycle life or power density. In order to increase the energy density and lower the cost, either the capacitance and/or the operating voltage must be increased according to the following equation [20,21]:

$$E = \frac{1}{2}CV^2 \quad (1)$$

where E is the energy density, C is the capacitance, and V is the operating voltage.

The key components to increase the energy density are the active material (electrode) and the electrolytic solution used in the system [18,21]. The requirements for the electrolyte include a wide stable voltage window for charge storage and good ionic conductivity for easy mobility of ions to the electrode surface [18-21]. Both non-aqueous (organic and ionic liquids) and aqueous electrolytes have been used in supercapacitors [18-21]. In general, aqueous electrolytes have several advantages over non-aqueous electrolytes including higher ionic conductivities and lower viscosities [18-21]. However, the voltage window of aqueous-based systems is limited by water electrolysis, which is typically ~1.2 V [21]. Another way to increase the energy is through increasing the capacitance, which is dependent on the electrode material. The electrode materials need to be electrochemically stable within the range of operating voltage of the electrolyte used in the system [18-21]. Also, they should have accessible high surface areas for charge accumulation, high electronic conductivity, and low cost [18-21].

1.2. Materials and Charge Storage Mechanisms

1.2.1. Double-Layer Storage Mechanism: Non-Electroactive Materials

Supercapacitors can be classified into two major types based on their charge-storage mechanisms as shown in Figure 1.3 [21].

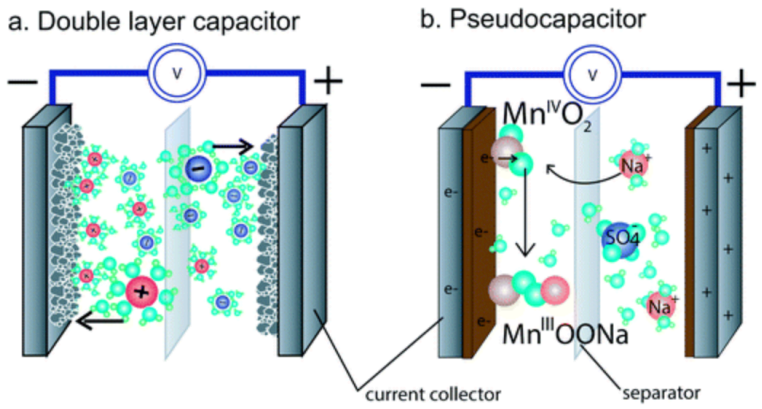

Figure 1.3: Basic schematics for an (a) all carbon double-layer capacitor, and (b) MnO_2 pseudocapacitor, all devices have an active material (e.g., carbon, MnO_2), a current collector, a separator and electrolyte, (e.g., Na_2SO_4 solutions), adapted from reference 21.

Activated carbons, the most commonly used material in commercial supercapacitors, store charge via the accumulation of charge at the electrode/electrolyte interface (see Figure 1.3a) [18,21, 32-34]; this results in the formation of an electrostatic double layer, and as such capacitances are typically limited to 100-125 F g^{-1} (less than 50 µF cm^{-2}) with an energy density of only 5 Wh kg^{-1} in the 2.7 V operating voltage window [32,33]. A representative of the current response (in terms of capacitance) as a function of applied voltage for activated carbons is shown in Figure 1.4 in the form of cyclic voltammogram [20]. The rectangular shape of the voltammogram and the lack of faradaic redox reactions peaks suggest that charge is stored via double-layer charge storage mechanism [18-21]. Typically, the areal specific capacitance from this type of charge storage is 20-50 µF cm^{-2} [18,21]. Additionally, the scan rate does not affect significantly the total capacitance according to this formula, introduced by Helmholtz in 1853 as the double-layer capacitance [21]:

$$C_{dl} = \frac{\varepsilon_r \varepsilon_o}{d} A \quad (2)$$

where C_{dl} is the double-layer capacitance, $\boldsymbol{\varepsilon}_r$ is the electrolyte dielectric constant, $\boldsymbol{\varepsilon}_o$ is the

dielectric constant of the vacuum, *d* is the effective thickness of the double layer (charge separation distance) and *A* is the electrode surface area.

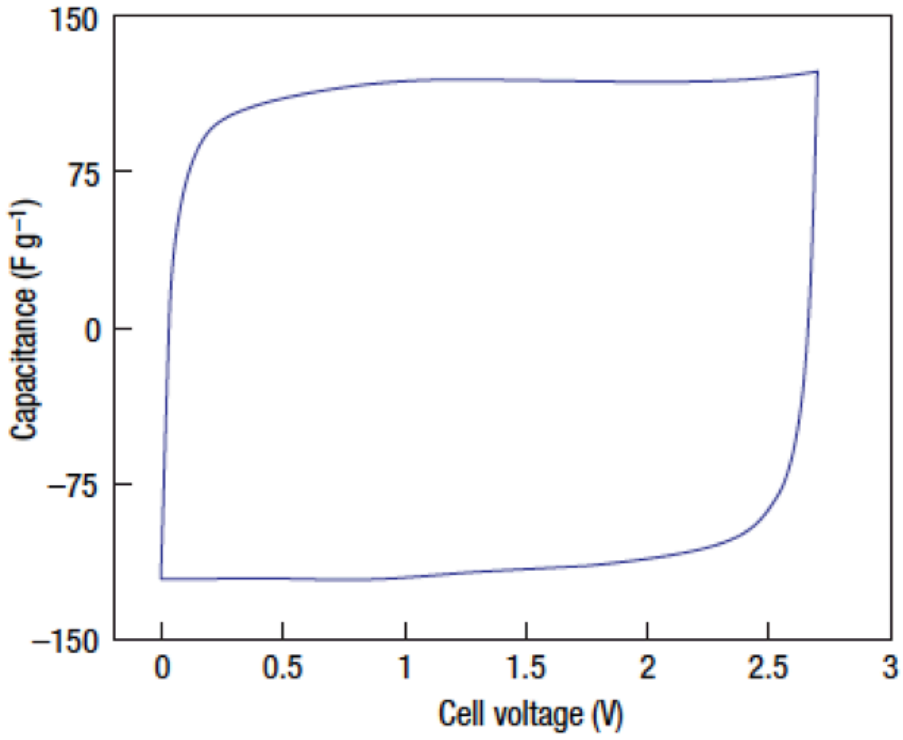

Figure 1.4: Cyclic voltammogram of activated carbon powder coated on aluminum in 1.5 mol dm^{-3} tetraethylammonium tetrafluoroborate (NEt_4^+ BF_4^-) in acetonitrile; scan rate 20 mV s^{-1}, taken from reference 20.

1.2.2. Pseudocapacitive Storage Mechanism: Electroactive Materials

Pseudocapacitive materials are electroactive materials that store charge via fast and reversible surface redox reactions or faradaic reactions involving electron transfer between the electrode and the electrolyte across the interface (see Figure 1.3b) [18-24], allowing these materials to possess capacitances in excess of 1000 F g^{-1} [18,21]. Typically, the areal specific capacitance from this type of charge storage is 10-100 times more than that of double layer storage (50 μFcm^{-2}) [20,21]. Capacitance from this charge storage is called pseudocapacitance, and is a function of the charge accumulated, *Q*

(which depends on the scan rate), and the differential operating voltage dV, and is given by [18,21]:

$$C_p = \frac{dQ}{dV} \quad (3)$$

The electrochemical processes that give rise to the pseudocapacitance include [21]:

Redox reaction: $Ox + ze^- \leftrightarrow Red$

Electrosorption: $M^{z+} + S + ze^- \leftrightarrow SM\ (S = surface\ sites, M = metal)$

Intercalation: $Li^+\ into\ MA_2\ (i.e.\ Li^+\ into\ TiS_2)$

All of these can be characterized by the Nernst equation, which is given by [3]:

$$E = E^0 + \frac{RT}{zF} ln \frac{R}{1-R} \quad (4)$$

where R is the concentration of the oxidizing species in the case of redox reaction and the fraction of site occupancy or layer lattice in the case of electrosorption and intercalation. Table 1.1 compares the essential features of double-layer capacitance behavior with that of pseudocapacitance, adapted from reference 21.

Table 1.1: Comparison between double-layer capacitance and pseudocapacitance.

Double-layer Capacitance	**Pseudocapacitance**
Non-faradaic (electrostatic)	Faradaic (involves electron transfer)
20-50 μFcm^{-2}	>>50 μFcm^{-2}
Capacitance fairly constant with potential	Capacitance varies with potential
Capacitance fairly constant with scan rate	Capacitance varies with scan rate
Highly reversible charging/discharging	Less reversible charging/discharging
Mirror-image voltammograms	No mirror-image voltammograms (except for some materials such as RuO_2 and MnO_2)

Materials exhibiting pseudocapacitance include conducting polymers such as polyaniline, polypyrrole, polythiophene and their derivatives, oxide based materials such as Ru and Mn [34-42] and early transition metal nitrides and carbides [43-59]. The high cost and toxicity of Ru limit its large-scale use in practical devices [19-21]. The other pseudocapacitive oxides, such as MnO_2, IrO_2, TiO_2, and V_2O_5 offer advantages over RuO_2 with respect to cost, environmental impact, and theoretical capacitances; however, their lower electronic conductivities and short cycle lives have limited their application [38-40]. Conductive polymers are more electronically conductive and typically possess wider voltage window than oxide materials [19-21]; however, swelling and shrinking of polymers during charge storage leads to degradation of the materials and capacitance fading [18-21].

Recently early transition-metal carbides and nitrides have attracted attention for use in electrochemical energy storage applications due to their chemical and electrical properties [60-62]. These materials are characterized by the presence of small non-metal atoms like carbon and nitrogen in the interstitial sites formed by the metal lattice [60-62]. The carbide and nitride materials can be produced with high accessible surface areas, high electronic conductivities, and lower cost [60,63]. They possess high capacitances and are electrochemically stable in a variety of aqueous and non-aqueous electrolytes [43-59]. Among the carbides and nitrides, the nitrides of vanadium (VN) and molybdenum (γ-Mo_2N) have received the most attention due to their high capacitances [45-53]. As reported by Kumta et al, nanostructured VN exhibits a high capacitance of 1340 F g^{-1} (3530 μFcm^{-2}) in 1.0 mol dm^{-3} aqueous KOH electrolytes [45]. This value is higher than those reported for any other metal oxides, polymers, or carbon materials

(maximum reported capacitance is 1300 F g^{-1} for RuO_2) [34-42]. The authors attributed the origin of the high capacitance to a combination of electric double-layer formation and faradaic redox reactions occurring on the nitride or oxynitride (VN_xO_y) surface [45]. The following equilibrium reaction was proposed for VN in 1.0 mol dm^{-3} aqueous KOH electrolytes:

$$VN_xO_y + OH^- \leftrightarrow VN_xO_y||OH^- + VN_xO_y - OH \quad (5)$$

where $VN_xO_y||OH^-$ represents the electrostatic attraction between OH^- and the nitride or oxynitride surface. According to the authors, the VN_xO_y-OH represents successive oxidation by the hydroxyl species on the VN_xO_y surface due to electron transfer across the double layer [45]. Details regarding the origin of this enhancement in capacitance were further elucidated via results from cyclic voltammetry (CV), and *ex-situ* Fourier transform infrared (FTIR) and X-ray photoelectron spectroscopy (XPS) measurements. The voltammogram for VN in alkaline KOH (0.1 mol dm^{-3} solution) is shown in Figure 1.5. The occurrence of reversible redox peaks on the voltammogram indicates the presence of faradaic redox reactions or pseudocapacitive charge storage [45].

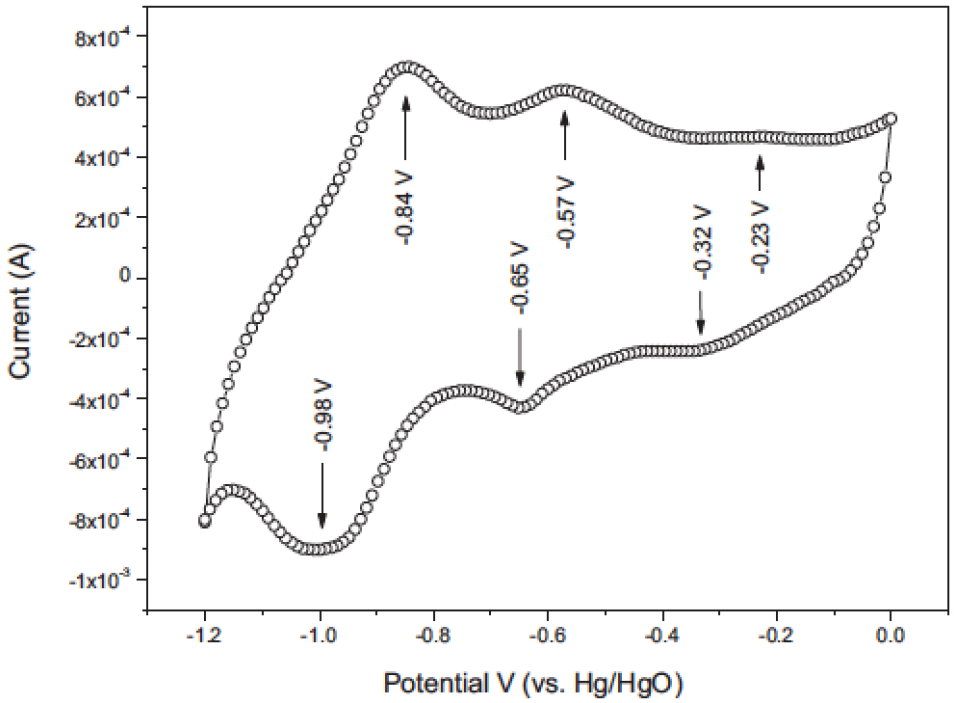

Figure 1.5: Cyclic voltammogram of VN nanocrystal synthesized at 600 °C, scanned at 2 mVs^{-1} in 0.1mol dm^{-3} KOH electrolyte, taken from reference 45.

The FTIR results shown in Figure 1.6a revealed the presence of an amorphous vanadium oxide layer producing absorption bands at 970 and 792 cm^{-1}. These were assigned to V=O and V-O vibrations, respectively. After cycling, various OH stretching peaks were observed in the FTIR spectra, suggesting adsorption of OH^- ions on the surface of the nitride. Figures 1.6 (b and c) show XPS spectra for VN before and after electrochemical cycling [45]. The XPS spectra indicated a shift in the V 2p peak to higher binding energy suggesting the presence of an oxide structure that is closest in stoichiometry to V_2O_5. During electrochemical cycling, the V $2p^3$ peak shifts to 515.9 eV with a decrease in intensity that suggests a reduction of the V_2O_5-type structure observed in the monolayer to either VO_2 or V_2O_3-type oxides via faradaic electron transfer [45]. From the XPS results, it was concluded that the oxide present on the surface changes its

oxidation state after electrochemical cycling, which coincides with the stable oxidation states of V seen in the pH versus standard hydrogen electrode (SHE) potential diagram provided by Pourbaix and Kelsall et al. [64].

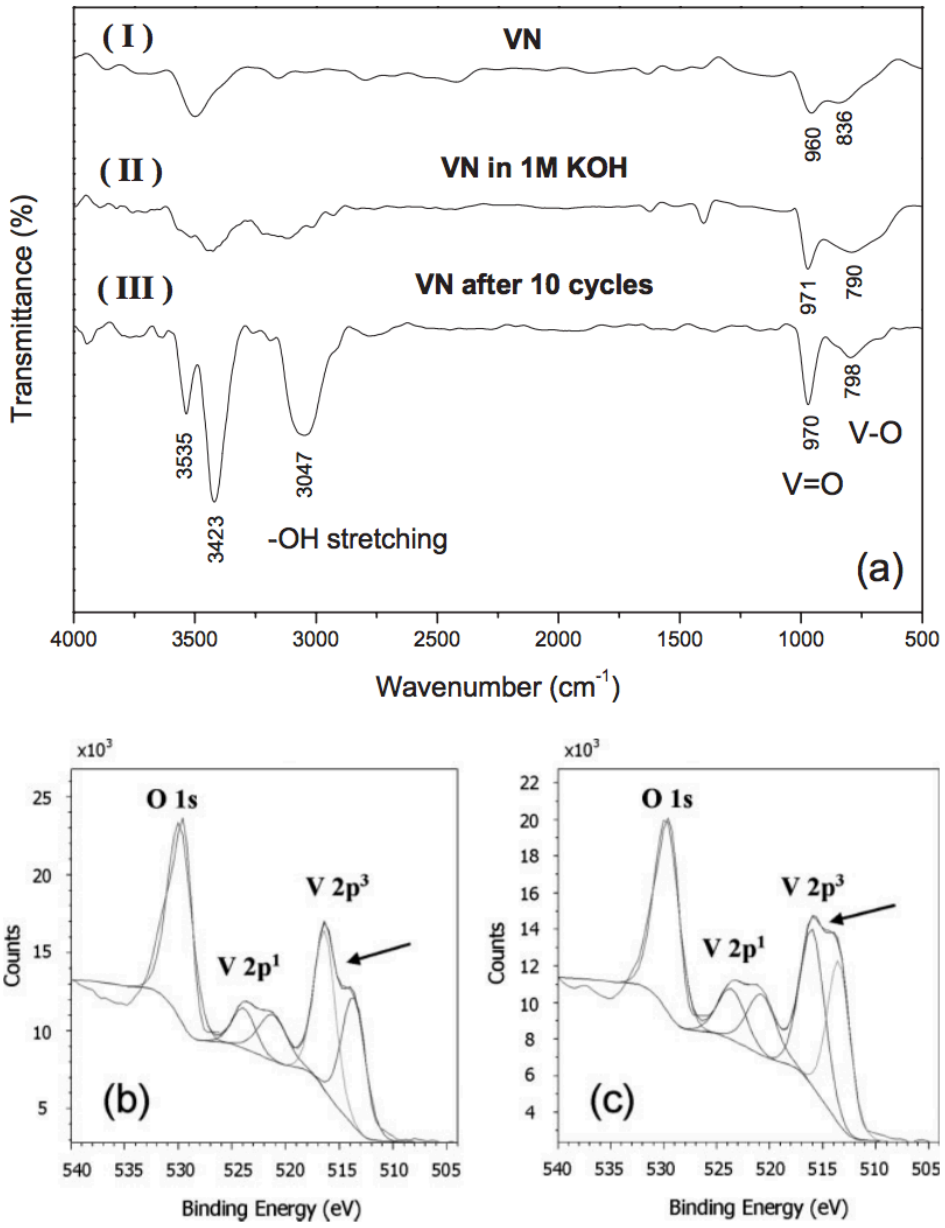

Figure 1.6: (a) FTIR spectra of (I) VN nanocrystals obtained at 400 C, (II) immersed in 1.0 mol dm^{-3} KOH solution for 24 hours, and (III) after ten cycles; and XPS spectra of VN nanocrystals (b) before and (c) after electrochemical cycling up to 200 cycles, taken from reference 45.

Despite such great efforts, the reaction mechanism that they proposed for VN is incomplete. Details regarding the change in the local structure, the extent of pseudocapacitance, and the quantity of adsorbed species are unknown. Given that the electrochemical charge storage process in these materials is very dynamic, a detailed examination of the material under operating conditions (*in situ*) would significantly advance our understanding of the charge-storage mechanism and enable full exploitation of the properties of high-surface-area carbides and nitrides in supercapacitor applications.

Recently, the Thompson group demonstrated, using ion isolation experiments in aqueous electrolytes, that H^+ and OH^- were the active ions that gave rise to the pseudocapacitance in Mo_2N and VN [46]. Using *in-situ* X-ray absorption spectroscopy (XAS) to track changes in the metal oxidation state in Mo_2N, a pseudocapacitive charge storage mechanism in aqueous acidic electrolytes was defined [53]:

$$Mo_2^{\delta}N + 2H^+ + 4e^- \leftrightarrow Mo_2^{\delta-1}N(H_{ads})_2 \qquad (6)$$

Figure 1.7a shows *in-situ* XAS near edge structure spectrum (XANES) of Mo_2N material at selected voltages within the stable voltage window. The changes in oxidation state were recorded as the material was cycled from -0.19 V to -0.73 V. The material did not show significant changes from the forward and reverse scans suggesting good electrochemical stability. A plot of oxidation state versus energy was derived from the XANES spectrum, and is shown in Figure 1.7b. Results from the XANES analysis suggested that as the voltage was decreased there was approximately one electron ($1e^-$) removed per Mo, as shown in Eq. 6.

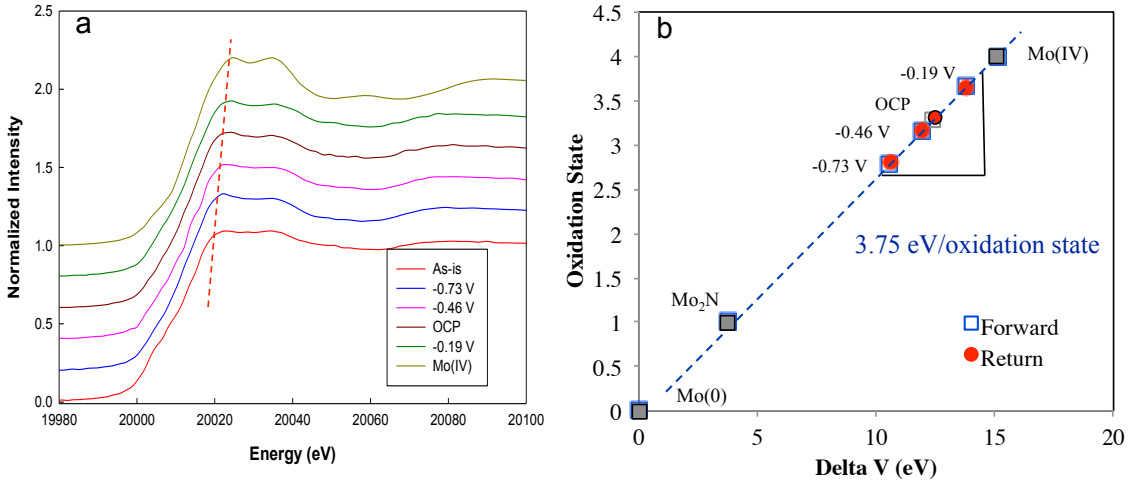

Figure 1.7: (a) Normalized XANES spectra for Mo_2N "as-is" and at selected voltages, (b) Change in oxidation states as function of energy for Mo_2N in aqueous 0.1 mol dm^{-3} H_2SO_4 solution, additionally, data for MoO_2 are also plotted for completeness, taken from reference 53.

The change in the local environment around the metal was also evaluated using extended X-ray absorption fine structure (EXAFS). Figure 1.8 shows the Fourier transforms of the EXAFS spectra for the forward and reverse direction. The peaks at 2 Å and 2.8 Å are attributed to Mo-N nearest neighbors and Mo-Mo next-nearest neighbors. The peaks at 3.8 Å are attributed to Mo-H-Mo multiple scattering. At this position, a significant and reproducible increase in the peak intensity at extreme potentials was observed, suggesting insertion of H^+ in the octahedral and tetrahedral interstitial sites during electrochemical charge storage. The insertion of hydrogen into interstitial sites in the Mo_2N lattice is not unexpected. For Mo in an *fcc* lattice, there are octahedral and tetrahedral interstitial sites. Nitrogen in Mo_2N occupies half of the octahedral interstitial sites leaving half of these sites and all of the tetrahedral sites for other small atoms like hydrogen. In terms of availability, up to two H^+ could be incorporated per Mo in tetrahedral interstices, with a third H^+ potentially occupying empty octahedral sites [53].

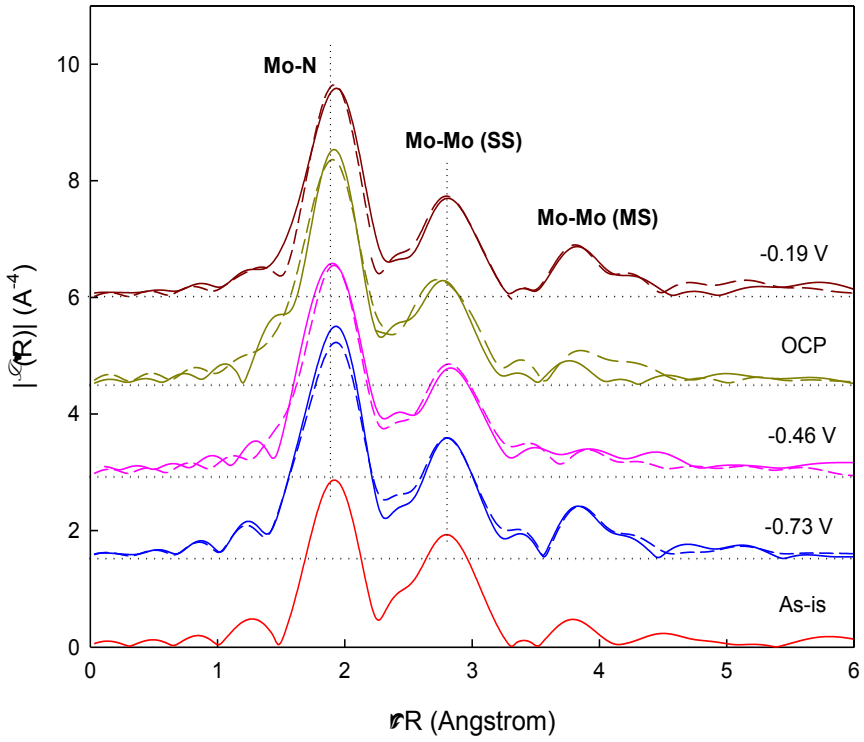

Figure 1.8: Fourier transforms of the K^3-weighted EXAFS data for Mo_2N "as-is" and at selected applied voltages in aqueous 0.1 mol dm^{-3} H_2SO_4 solution. The solid line represents measured data while increasing voltage. The dashed line represents measured data while decreasing voltage. Successive spectra are offset vertically by 1.5 for presentation, taken from reference 53.

Despite the effectiveness of the *in-situ* XAS experiment, there are some limitations to the capability of the experiment. For instance, the distribution of H^+ with applied voltage (location and depth of storage) remains poorly understood. Also, the XAS experiment was performed on only Mo_2N material; details regarding the change in oxidation states and local structure during electrochemical charge storage is warranted for other promising carbides and nitrides.

In addition to the redox chemistry, the specific capacitance of a material can be a function of the pore structure [65-76]. For high surface area activated carbons, the maximum capacitance is obtained when the size of the pore and adsorbed ion are

comparable [65-73]. Under these conditions, potentials of the opposing walls overlap, creating a potential well that is deeper than that available on larger pores walls [65-73]. This potential well enhances the adsorption of ions [66,68,70]. For larger pores there is no such enhancement and for smaller pores (i.e. ultramicropores), the space is not sufficient [65-73]. These findings have helped in the design of high performance, carbon-based supercapacitors. Thus, the development of early transition metal carbides and nitrides for use in supercapacitors would benefit from a detailed understanding of the relationship between the specific capacitance and the pore size.

1.3. Research Goal and Overall Approach

Early transition-metal carbides and nitrides are promising candidates for use in supercapacitors, due to their high electronic conductivities, high surface areas, high capacitances and good electrochemical stabilities. Further development of these electrode materials will benefit from a better understanding of how changes occur in the electrode material during the charge storage process. Despite efforts to date, the nature of the charge storage mechanism and pseudocapacitive properties of early transition-metal carbides and nitrides remains incomplete. The key aspect to the full exploitation of these materials in supercapacitors is an understanding of their pseudocapacitive charge-storage mechanism. The goal of the research described in this dissertation is to enhance our understanding of the charge-storage mechanisms for high-surface-area early transition-metal carbides and nitrides by developing detailed relationships between their capacitive, bulk, and surface properties using various physical and electrochemical characterization techniques in combination with *in-situ* surface and bulk characterization tools. The

dissertation comprises of seven chapters including the introduction. The following section provides a brief description of the remaining chapters.

1.4. Brief Description of Chapters

Chapter 2: Synthesis and Physical Characterization

This chapter discusses the synthesis and physical properties of the carbides and nitrides of Ti, V, Nb, Mo, and W metals. These materials were synthesized using a solid-state temperature-programmed reaction method. Physical properties including crystal structure, crystallite size, and phase purity were determined using X-ray diffraction. N_2 physisorption analysis was used to determine the surface area, average particle and pore sizes, and pore size distributions. The surface morphology and composition of synthesized materials were examined using scanning electron microscopy and Auger electron spectroscopy, respectively. Additionally, the effects of synthesis temperature on the surface area, correlation between crystalline size and pore size, and relation between the crystal structure and the pore size distribution were also established.

Chapter 3: Electrochemical Characterization

This chapter discusses the electrochemical properties of phase-pure, high-surface-area carbides and nitrides of Ti, V, Nb, Mo, and W metals. Cyclic voltammetry analysis was used to determine the operating voltage window, capacitance, and faradaic redox activities in aqueous electrolytes. Long term stability assessment and kinetics were carried out using chronopotentiometry and chronoamperometry, respectively. Electrochemical impedance spectroscopy coupled with square wave voltammetry was used to deconvolute the total capacitance into pseudocapacitance and double-layer capacitance. Additionally, the effects of crystal structure and composition on charge

storage, and the percent contribution of pseudocapacitance to the charge storage are also discussed.

Chapter 4: Charge Storage Mechanism

The focus of this chapter is to define the faradaic redox reactions involved in the pseudocapacitive charge storage mechanisms for carbides and nitrides in aqueous electrolytes, in particular, for γ-Mo_2N and VN, using X-ray absorption spectroscopy and small angle neutron scattering. X-ray absorption spectroscopy was used to determine the metal electronic structure and local structural changes during electrochemical charge storage. Neutron scattering techniques were used to quantify the adsorbed species as function of applied voltages. Additionally, the location of adsorbed species in pores was identified. Proposed pseudocapacitive charge storage mechanisms, consistent with physical, electrochemical, and bulk properties, yielded capacitances in excess of 1040 and 3550 μFcm^{-2} for the γ-Mo_2N and VN materials, respectively, in 1.2 V operating voltage windows.

Chapter 5: Surface Characterization

The surface properties are discussed in this chapter. Relationships between the pore size and the pseudocapacitance were established. The effects of an oxygen passivation layer on the physical and electrochemical properties including surface area, electrochemical stability, and capacitance were investigated. A correlation between passivated (with thin oxide layer on the surface) and non-passivated (native material) carbides and nitrides in terms of physical and electrochemical properties was also established.

Chapter 6: Effect of Electrolyte

In this chapter the possibility of using non-aqueous electrolytes such as protic ionic liquids containing abundant pseudocapacitive active ions (H^+) is explored with the aim of achieving higher pseudocapacitance and wider voltage windows as compared to aqueous electrolytes. Comparison between aqueous and non-aqueous electrolytes in terms of capacitance, operating voltage window, and faradaic redox activities were made. Additionally, the effects of ionic conductivity, viscosity, and ion transport on the charge storage are discussed. Given that the energy density of supercapacitors increases as a square of the voltage, high pseudocapacitance accompanied by a wide operating voltage window could greatly enhance the overall energy density of supercapacitors based on high-surface-area early transition-metal carbides and nitrides.

Chapter 7: Summary and Future Work

This chapter provides a summary and limitations of the research described in this dissertation work. Relevant future research and directions to mitigate the limitations of the current work have been proposed. Additionally, key aspects of the fabrication and development of supercapacitor devices based on high-surface-area early transition-metal carbides and nitrides are also discussed.

1.5. References

1. World Population Clock, March 15, 2016.
2. Statistical Review of World Energy, London, (2013).
3. http://www.iea.org/publications/freepublications/. IEA, pp. 6, May 5, (2014).
4. http://www.iea.org/publications/freepublications/. IEA, pp. 8, March, (2015).
5. http://future360.tv/video/why-energy-important.
6. Grid Energy Storage-U.S. Department of Energy, December 12, (2013).
7. D. Pendicka, Storing energy from the wind in compressed-air reservoirs, The New Scientist, 195 (29) (2007) 44-47.
8. Z. Yang, J. Zhang, M. C. W. Kintner-Meyer, X. Lu, D. Choi, P. Lemmon, and J. Liu, Chem. Rev., 111 (2011) 3577-3613.
9. International Energy Agency, Electricity Access Database-World Energy Outlook (2015).
10. U.S. Energy Information Administration, Electricity in the U.S., March 29, (2016).
11. Handbook of Energy Storage for Transmission and Distribution Applications; Electrical Power Research Institute, Palo Alto, CA, and Department of Energy: Washington, DC, (2003).
12. Environmental Assessment of Plug-In Hybrid Electric Vehicles; Electric Power Research Institute and Natural Resources Defense Council: Palo Alto, California, Nationwide Greenhouse Gas Emission, 1 (2007).
13. B. Dunn, H. Kamath, and J. M. Tarascon, Science, 334 (2011).

14. M. M. Thackeray, C. Wolverton, and E. D. Isaacs, Energy Environ. Sci., 5 (2012) 7854-7863.
15. M. Tarascon and M. Armand, Nature, 414 (2001) 359-367.
16. M. Armand and M. Tarascon, Nature, 451 (2008) 652-657.
17. K. Amine, Nature Energy, 1 (2016) 15018.
18. A. Yu, V. Chabot, and J. Zhang, Electrochemical Supercapacitors for Energy Storage and Delivery, CRC Press, (2013).
19. G. Wang, L. Zhang, J. Zhang, Chem. Soc. Rev., 41 (2012) 797-828.
20. P. Simon, Y. Gogotsi, Nature Materials, 7 (2008) 845.
21. B. E. Conway, Electrochemical Supercapacitors, Kluwer Academic/ Plenum Publishers, (1999).
22. D. Pech, M. Brunet, H. Durou, P. Huang, V. Mochalin, Y. Gogotsi, P. L. Taberna, P. Simon, Nature Nanotechnology, 5 (2010) 651-654.
23. L. Zhang et al., International Journal of Hydrogen Energy, 34 (2009) 4889-5899.
24. M. Egashira, K. Ueda, N. Yoshimoto, M. Morita, J. Electrochem. Soc., 214 (2008).
25. World Ultracapacitor Markets, N661-27, Frost and Sullivan, (2009).
26. Batteries and Ultra-capacitors for the Smart Power Grid, NanoMarkets, (2009).
27. http://cleantechnica.com/2011/05/11/cheaper-ultracapacitors-for-electric-vehicles.
28. http://analysis.energystorageupdate.com/lithium-ion-costs-fall-50-within-five-years.
29. http://www.greentechmedia.com/articles/read/aes-energy-storage-targets-30-billion-peak-power-substitution-market.

30. http://singularityhub.com/2015/06/11/robocars-ultracapacitors-energy-sources.
31. http://www.sunvaultenergy.com/sunvault-energy-and-edison-power-company-create-massive-10000-farad-graphene-supercapacitor.
32. P. Simon, A. Burke, Electrochemical Society: Interface Spring, p. 38 (2008).
33. A. Burke, Int. J. Energy Res., 34 (2010) 133.
34. M. Mastragostino, C. Arbizzani, F. Soavi, Solid State Ionics, 148 (2002) 493.
35. A. Rudge, J. Davey, I. Raistrick, S. Gottesfeld, J. Power Sources, 47 (1994) 89.
36. C. C. Hu, K. H. Chang, M. C. Lin, Y. T. Wu, Nano Lett., 6 (12) (2006) 2690.
37. C. C. Hu, T. W. Tsou, Electrochem. Commun., 4 (2002) 105.
38. T. Brousse, M. Toupin, R. Dugas, L. Athouel, O. Crosnier, D. Belanger, J. Electrochem. Soc., 153 (12) (2006) A2171.
39. C. Xu, F. Kang, B. Li, H. Du, J. Mater. Res., 25 (8) (2010) 1421.
40. M. Toupin, T. Brousse, D. Bélanger, Chem. Mater., 16 (16) (2004) 3184.
41. J. P. Xheng and T. R. Jow, J. Electrochem. Soc., 1 (1995) 142.
42. W. Sugimoto, K. Yokoshima, Y. Murakami, Y. Takasu, Electrochimica Acta, 52 (2006) 1742-1748.
43. M. Azuma, Y. Nakato, H. Tsubomura, J. Electrochem. Soc., 255 (1988) 179.
44. A. M. Glushenkov, D. Hulicova, D. Llewellyn, G. Q. Liu, Y. Chen, Chem. Mater., 22 (2010) 914.
45. D. W. Choi, G. E. Blomgren, P. N. Kumta, Adv. Mater., 18 (2006) 1178.
46. P. Pande, P. Rasmussen, L. Thompson, J. Power Sources, 207 (2012) 212-215.
47. D. Choi, P.N. Kumta, J. Am. Ceram. Soc., 94, 8 (2011) 2371.
48. T. C. Liu, W. G. Pell, B. E. Conway, J. Electrochem.Soc., 145 (6) (1998) 1882.

49. M. R. Wixom, D. J. Tarnowski, J. M. Parker, J. Q. Lee, P. L. Chen, I. Song, L. T. Thompson, Mat. Res. Soc. Symp. Proc., 496 (1998) 643.

50. X. Zhou, C. Shang, S. Doug, X. Chen, P. Han, L. Li, J. Yao, Z. Liu, H. Xu, Y. Zhu, G. Cui, Appl. Mater. Interfaces, 3 (2011) 3058.

51. S. L. Roberson, D. Finello, R. F. Davis, J. Appl. Electrochem., 29 (1999) 75.

52. R. L. Porto, R. Frappier, J. B. Ducros, C. Aucher, H. Mosqueda, S. Chenu, B. Chavillon, F. Tessier, F. Cheviré, T. Brousse, Electrochimica Acta 82 (2012) 257-262.

53. P. Pande, A. Deb, A. S. Sleightholme, A. Djire, P. Rasmussen, J. Penner-Hahn, L. T. Thompson, J. Power Sources, 289 (2015) 154-159.

54. G. Hasegawa, A. Kitada, S. Kawasaki, K. Kanamori, K. Nakanishi, Y. Kobayashi, H. Kageyama, T. Abe, J. of Electrochemical Soc., 162 (1) (2015) A77-A85.

55. O. Kartachova, A. M. Glushenkov, Y. Chen, H. Zhang, X. J. Dai, Y. Chen, J. Power Sources, 220 (2012) 298-305.

56. A. Djire, O. Ajenifujah, A. Sleightholme, P. Rasmussen, L. T. Thompson, J. Power Sources, 207 (2015) 212-215.

57. D. Choi, P.N. Kumta, J. Am. Ceram. Soc. 90 (2007) 3113-3120.

58. A. R. Ko, S.B. Han, Y.W. Lee, K.W. Park, Phys. Chem. Chem. Phys. 13 (2011) 12705-12707.

59. B. E. Conway, J. Electrochem. Soc., 6 (1991) 138.

60. R. B. Levy, M. Boudart, Science, 181 (1973) 547.

61. S. T. Oyama, The Chemistry of Transition-Metal Carbides and Nitrides, Chapman and Hall Publisher, 1996.

62. S. T. Oyama, Catal. Today 15 (1992) 179.

63. J. B. Claridge, A. P. E. York, A.J. Brungs, M. L. H. Green, Chem. Mater 12 (1) (2000) 132.

64. G. H. Kelsall, I. Thompson, P. A. Francis, J. Appl. Electrochem. 23 (1993) 417.

65. C. Largeot, C. Portet, J. Chmiola, P. L. Taberna, Y. Gogotsi, and P. Simon, J. Am. Chem. Soc., 130 (2008) 2730-2731.

66. S. Boukhalfa, L. He, Y. B. Melnichenko, and G. Yushin, Angew. Chem., 125 (2013) 4716-4720.

67. V. López-Flores, M. A. Roldán, C. Real, A. Muñoz Páez, G. R. Castro, J. Appl. Phys., 104 (2008) 023519.

68. L. He, Y. B. Melnichenko, N. C. Gallego, C. I. Contescu, J. Guo, and J. Bahadur, Carbon, 80 (2014) 82-90.

69. J. Huang, B. G. Sumpter, V. Meunier, Chem. Eur. J., 14 (2008) 6614-6626.

70. W. C. Conner, J. P. Fraissard, Fluid Transport in Nanoporous Materials: Proceedings of the NATO Advanced, Springer (2006).

71. P. Simon, A. Burke, J. Electrochem. Soc. Interface, Spring (2008).

72. B. P. Bakhmatyuk, B. Y. Venhryn, I. I. Grygorchak, M. M. Micov, S. I. Mudry, Advanced Study Center Co. Ltd, (2007).

73. J. Chmiola, G. Yushin, Y. Gogotsi, C. Portet, P. Simon, P. L. Taberna, Science, 313 (2006) 1760-1763.

74. D. Jiang, Z. Jin, D. Henderson, and J. Wu, J. Phys. Chem. Lett., 3 (2012) 1727-1731.

75. S. Boukhalfa, D. Gordon, L. He, Y. B. Melnichenko, N. Nitta, A. Magasinski, and G. Yushin, ACS Nano, 8 (3) (2014) 2495-2503.

76. S. Boukhalfa, L. He, Y. B. Melnichenko, and G. Yushin, Angew. Chem., 125 (2013) 4716-4720.

Chapter 2

Physical and Surface Properties

2.1. Early Transition-Metal Carbides and Nitrides

Small atoms, such as carbon or nitrogen, incorporated interstitially in the lattices of early transition metals (Ti, V, Nb, Ta, Mo, W) produce a class of compounds with unique physical and chemical properties [1]. These carbides and nitrides are called interstitial compounds. The incorporation of the carbon or nitrogen into the metal structure causes an expansion of the metal crystal lattice [1]. These interstitial compounds adopt different crystal structures based on geometric and electronic factors. The geometric factor is explained by the so-called Hägg rule, which states that simple structures such as face-centered cubic (fcc), hexagonal-closed packed (hcp), and simple hexagonal (hex) (shown in Figure 2.1) are formed when the ratio of the radii of non-metal to metal is less than 0.59 [2]. The electronic factor that explains the difference between the crystal structures of the interstitial compounds and the parent metals (which typically have a body-centered cubic structure (bcc)) is based on the Engel-Brewer theory. This theory states that the structure adopted by these interstitial compounds depends on the number of s-p valence electrons per atom (e/a) [1]. As such, the mixing of the s-p orbitals of the non-metal with the s-p-d band of the metal will dictate the crystal structure of the carbide or nitride material. For example, when e/a is between 1 and 1.5, bcc structures are

formed, between 1.7 and 2.1, hcp structures are formed, and fcc structure are preferred when e/a is between 2.5 and 3.

IV	V	VI
Ti	V	Cr
Zr	Nb	Mo
Hf	Ta	W
MC/MN	MC/MN	M_xC_y/M_xN_y

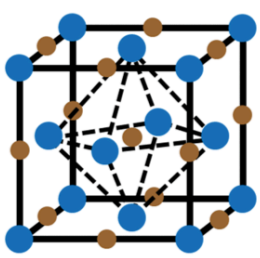

Face-Centered Cubic

TiC, VC, NbC
TiN, VN, NbN

α-MoC_{1-x}, β-WC_{1-x}
γ-Mo_2N, β-W_2N

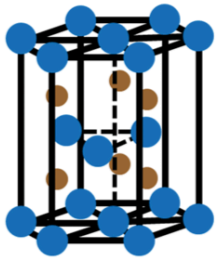

Hexagonal closed packed

β-Mo_2C, W_2C

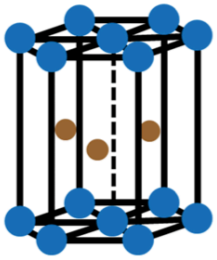

Simple hexagonal

MoC, WC
δ-WN

Figure 2.1: Crystal structures for Groups 4-6 transition metal carbides and nitrides.

In addition to the changes in the crystal structure, the addition of carbon or nitrogen into the parent metal lattice results in the formation of carbide and nitride materials with physical and chemical properties that are different from the parent metal [1]. These interstitial transition-metal carbides and nitrides possess high melting points, extreme hardness and strength, high electrical and thermal conductivities [1]. Table 2.1

lists the electrical conductivities and unoccupied interstitial (octahedral and tetrahedral) sites for various carbides and nitrides.

Table 2.1: Electrical conductivities and density of unoccupied interstices for early transition-metal carbides and nitrides [8].

Material	Electrical Conductivity (Sm^{-1}) $x10^7$	Available Tetrahedral Interstices/ Mole of Material ($x10^{21}$)	Available Octahedral Interstices/ Mole of Material ($x10^{20}$)
TiN[a]	0.40	1.20	None
VN[a]	0.12	1.21	None
VC[a]	0.16	1.20	None
NbN[a]	0.17	1.20	None
NbC[a]	0.29	1.20	None
β-W_2N[b]	1.11	2.41	6.03
β-WC_{1-x}[b]	0.45	2.33	5.84
γ-Mo_2N[b]	0.51	2.41	6.03
α-Mo_2C[b]	-	2.41	6.02
β-Mo_2C[c]	0.14	0.29	0.72
(α+β)-Mo_2C[d]	-	-	-

[a] Face-centered-cubic structured materials with 1:1 metal to non-metal stoichiometry
[b] Face-centered-cubic structured materials with 2:1 metal to non-metal stoichiometry
[c] Hexagonal-closed-packed structured material with 2:1 metal to non-metal stoichiometry
[d] (50% fcc + 50% hcp) structured material with 2:1 metal to non-metal stoichiometry

The carbides and nitrides have attracted attention because they are excellent catalysts for a number of reactions usually carried out by the more expensive noble metals [4-6]. The similarity in catalytic and electronic properties between the carbides and the noble metals was first reported by Levy and Boudart in 1973 [7]. They noted that WC behaved catalytically like Pt, and suggested that this was due to the addition of carbon valence electrons to those of tungsten. A few years later, these findings were extended to early transition-metal nitrides [8]. Since then, these interstitial compounds

have been tested for several thermocatalytic and electrocatalytic reactions ranging from ammonia synthesis to hydrocarbon reforming, both as catalysts and as active-catalyst supports [9-16].

In the last decade, there have been several investigations of the use of early transition-metal carbides and nitrides as electrode materials for energy storage applications including supercapacitors due to their high surface areas, high electronic conductivities, high capacitances and wide operating voltage windows [16-32]. Based on the above aforementioned properties, these high surface area materials hold promise to revolutionize the electrochemical energy storage landscape via low materials cost and high energy and power densities.

Some of the methods developed for synthesizing high surface area carbides and nitrides include gas-phase reactions of metal compounds [34-36], reaction of gaseous reagents with solid-state metal compounds [37], pyrolysis of metal precursors, and solution reactions [38]. Among these, one of the most attractive and widely used is the temperature-programmed reaction (TPR) method developed by Boudart and co-workers [7, 11-13] for the nitrides and carbides of molybdenum and tungsten metals, which was later expanded to other carbides and nitrides by Claridge and co-workers [9]. The TPR method is attractive because it is easy, consistent, and results in high surface area materials [7-9].

2.2. Experimental Methods

2.2.1. Carbides and Nitrides Synthesis

High-surface-area carbides and nitrides of Ti, V, Nb, Mo, and W were prepared from TiO_2 (99.9%, Alfa Aesar), V_2O_5 (Alfa Aesar), Nb_2O_5 (99.9985%, Alfa Aesar),

$(NH_4)_6Mo_7O_24 4(H_2O)$ (81-83% as MoO_3, Alfa Aesar) and WO_3 (Alfa Aesar) using the TPR method [17-22]. Figure 2.2 shows a schematic of the TPR temperature profile. A mixture of 15% CH_4 in H_2 (Cryogenic Gases) was used as the reaction gas for the synthesis of the carbides. Anhydrous NH_3 (Cryogenic Gases) was used as the reaction gas for the nitrides. The precursors were first crushed and sieved to retain particles with sizes between 125 and 250 μm. The particles were then supported on a quartz-wool plug in a quartz-tube reactor. The reaction conditions used to synthesize the carbides and nitrides of Ti, V, Nb, Mo, and W metals are listed in Table 2.2. The synthesis of α-Mo_2C and WC_{1-x} involved the nitridation of the corresponding oxide precursor using NH_3 to form γ-Mo_2N and β-W_2N, respectively, which was then allowed to cool to room temperature before carburization with 15% CH_4 in H_2 to form the final products. After synthesis, the materials were quenched to room temperature. Because of their pyrophoric nature, the materials were then passivated using a flowing mixture of 1% O_2/He (Cryogenic Gases) for 5 hours to form an oxygen-rich protective layer that prevents bulk oxidation of the material when exposed to air.

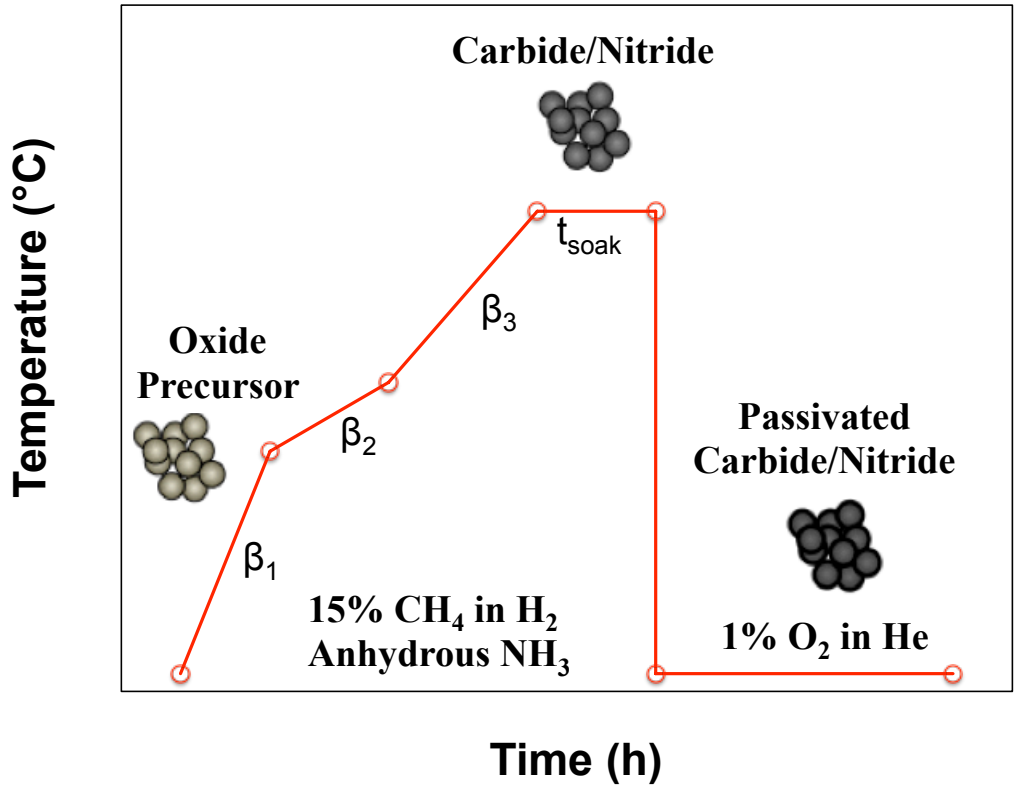

Figure 2.2: Schematic of the temperature program used to synthesize the carbides and nitrides of Ti, V, Nb, Mo, and W metals. β_1, β_2, β_3 represent the heating rates, and t_{soak} is the soak time.

2.2.2. Material Characterization

2.2.2.1. X-ray Diffraction Analysis (XRD)

XRD is a bulk characterization technique that is used for identifying the atomic and molecular structure of a crystal, in which the crystalline atoms cause a beam of incident X-rays to diffract into many specific directions. Distinctive peak patterns unique to the material are obtained by measuring the angles and intensities of these diffracted beams. XRD patterns show relative intensities of diffracted x-rays versus diffraction angle.

Table 2.2: Synthesis conditions for early transition-metal carbides and nitrides [7-13].

Material	Precursor Weight (g)	Reactant Gas	Flow rate mL/min	T_1 °C	β_1 °C/min	T_2 °C	β_2 °C/min	T_3 °C	β_3 °C/min	t_{soak} min
TiN	1.0	NH_3	450	300	9.18	1000	0.933	-	-	60
VN	0.4	NH_3	1200	750	5.00	-	-	-	-	60
VC	0.4	15%CH_4/H_2	800	157	8.00	900	2.00	-	-	120
NbN	1.0	NH_3	600	800	1.00	-	-	-	-	180
NbC	0.4	15%CH_4/H_2	800	900	9.94	-	-	-	-	120
β-W_2N	1.0	NH_3	400	350	10.84	460	0.611	750	2.9	60
β-WC_{1-X}	1.0	15%CH_4/H_2	250	200	10.29	750	1	-	-	60
γ-Mo_2N	1.5	NH_3	400	350	10.00	450	0.66	700	1.66	120
α-Mo2C	1.3	NH_3	400	350	10.00	450	0.66	700	1.66	120
	1.3	15%CH_4/H_2	250	200	10.3	590	1.00			120
β-Mo_2C	1.3	15%CH_4/H_2	250	200	10.3	590	1.00			120
(α+β)-Mo_2C	1.3	H_2	400	350	4.64	-	-	-	-	720
		15%CH_4/H_2	400	590	2.67	-	-	-	-	120

Based on the crystal structure of the material, the XRD pattern of the material exhibits peaks over a range of diffraction angles. These peaks correspond to diffraction from the various crystal planes in the material, and thus can be used to determine useful physical properties including crystal structures and the crystallite size [39].

In this dissertation, XRD analysis was performed using a Rigaku Miniflex Diffractometer with a Cu Kα (λ= 0.15404 nm) source. The powder samples were loaded on a glass sample holder. XRD was carried out at a scan rate of 5.0° min^{-1} with a step size of 0.1° over a 2θ range of 10 to 90°. The JADE 10.0 software, which has the International

Centre for Diffraction Database built-in for phase identification, was used to identify the phase purity of synthesized carbide and nitride materials by matching the measured spectra to the database to obtain the chemical composition of the material.

2.2.2.2. N_2 Physisorption Analysis

Properties such as specific surface area and the pore size distribution are fundamental parameters that can be directly correlated to the porous structure of a solid material. These properties can be determined by the physisorption technique, which can be carried out by a Micromeritic ASAP 2020 surface area and porosity analyzer.

The adsorption of gas molecules on solid surfaces is modeled by the Brunauer-Emmett-Teller theory (BET). This physical adsorption of a gas over the entire exposed surface of a material and the filling of pores is called physisorption and is used to measure total surface area and the average pore size of solid powder materials.

The specific surface area of a powder is estimated from the amount of nitrogen adsorbed in relationship with its pressure, at the boiling temperature of liquid nitrogen under normal atmospheric pressure. The measurement process of physisorption involves chilling the measured powder, using nitrogen to adhere to the surface, then lowering the pressure, leading to desorption. A typical adsorption and desorption isotherm for carbide or nitride materials is shown in Figure 2.3.

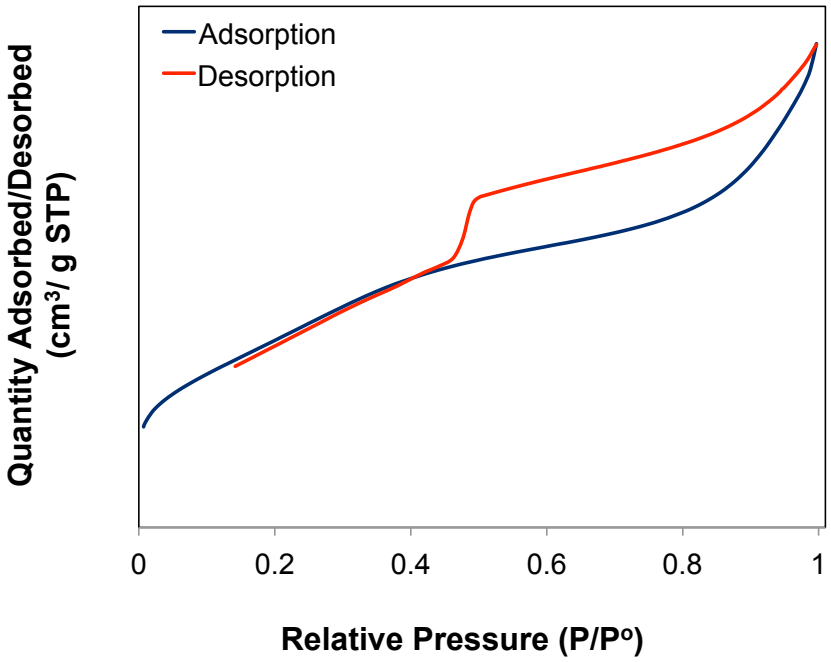

Figure 2.3: A typical N_2 physisorption isotherm for high-surface area carbides and nitrides, showing adsorption and desorption curves for Mo_2N material.

While the BET method is used to determine the surface area, the pore size distribution is determined using the Barrett-Joyner-Helenda (BJH) and Horvath-Kawazoe (HK) methods. The BJH method is employed to determine the pore size distributions from experimental isotherms using the Kelvin model of pore filling [40]. It applies to mesopore (2-50 nm) and macropore (> 50 nm) size ranges. The HK method applies to the micropore size range (< 2 nm), and is based on slit-shaped pores, cylindrical pores, and spherical pores.

As mentioned previously, in this study, BET surface area and pore size distribution analysis of the synthesized materials was carried out using a Micromeritics ASAP 2010 analyzer. Approximately 100 mg of material was analyzed at a time. Prior to the analysis, the materials were degassed at 350°C under vacuum for 8 h. After

degassing, the sample was moved to the analysis chamber. The analysis chamber was cooled to 77K with liquid N_2.

2.2.2.3. Scanning Electron Microscopy (SEM)

The surface morphologies of synthesized carbides nitrides were examined using SEM. SEM is an electron microscopic technique that produces images of a sample by scanning it with a focused beam of electrons. The electrons interact with atoms in the sample, producing various signals that contain information about the sample's surface morphology and composition. The microscopy was carried out using a FEI Nova 200 Nanolab field emission electron microscope operating at an accelerating voltage of 10.0 kV.

2.2.2.4. Auger Electron Spectroscopy (AES)

AES is a surface analysis tool that can provide combined information as one can obtain from both x-ray photoelectron spectroscopy (XPS) and scanning electron microscopy (SEM). These include the chemical composition of the material surface, the elemental mapping, and the depth profile (with ion sputtering assistance). The advantages of AES over other surface analysis methods are excellent spatial resolution (~ 10 nm), surface sensitivity (~ 2 nm in depth), and efficient detection of light elements. AES was performed with a Physical Electronics Auger Nanoprobe 680 instrument using a beam voltage of 3 kV and a beam current of 10 nA. The electrodes were placed in a transfer chamber and drawn to 1.0 µTorr vacuum; then transferred to the analysis chamber (~ 1.5 nTorr). Auger spectra were collected in the range of 0 to 2 keV. Additionally, the electrodes were sputtered with Ar at a rate of 2.5 ml min^{-1} to clean the surfaces and Auger

spectra were collected after removal of surface contaminants such as carbon to see if the elemental composition varied as a function of depth.

2.3. Results and Discussion

2.3.1. Physical Properties

The XRD patterns for the Ti, V, Nb, Mo, and W carbide and nitride materials are shown in Figures 2.4 and 2.5, respectively. The peaks matched those for the standard compounds, confirming that the bulk materials were phase-pure fcc and hcp carbides and nitrides. Table 2.3 lists key physical properties for the materials including their crystallite sizes and surface areas. The Mo and W-based materials contained the smallest crystallites and possessed the highest surface areas while the Ti, V, and Nb-based materials contained the largest crystallites and lowest surface areas. The larger crystallite sizes and lower surface areas for the Ti, V, and Nb-based materials, in particular TiN, VC, and NbC materials, were likely due to the high synthesis temperatures (over 900 °C). Except for W-based materials, all the nitrides have higher surface areas and higher micropore volumes than their carbide counterparts. Overall, the smaller the crystalline size, the higher the surface area.

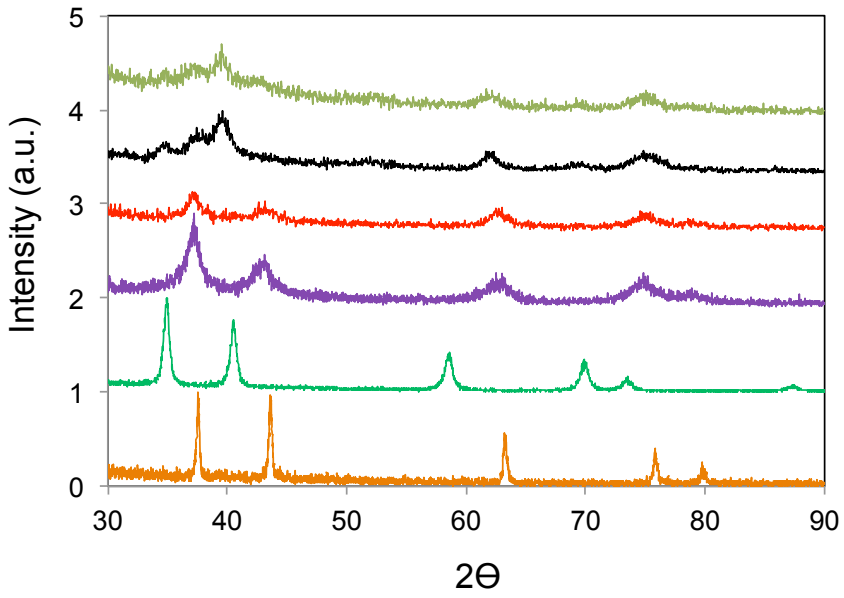

Figure 2.4: X-ray diffraction patterns for VC, NbC, WC_{1-x}, and α-Mo_2C, β-Mo_2C, (α+β)-Mo_2C (from the bottom to the top), diffraction patterns matched those for the standard compounds indicating phase purity of all the materials.

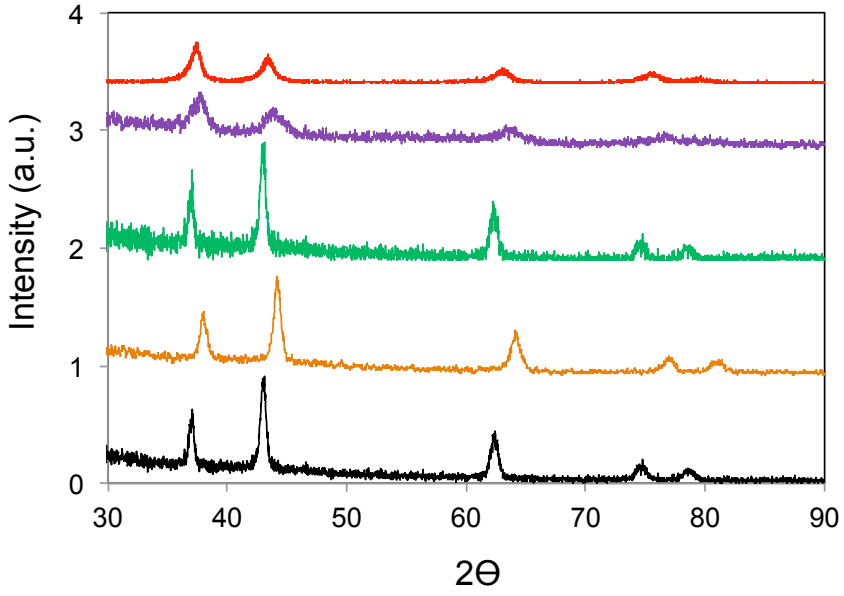

Figure 2.5: X-ray diffraction patterns for TiN, VN, NbN, W_2N, and γ-Mo_2N (from the bottom to the top), diffraction patterns matched those for the standard compounds indicating phase purity of all the materials.

Table 2.3: Physical properties of early transition-metal carbides and nitrides.

Material	Crystallite Size (nm)	Surface Area (m^2g^{-1})	Pore Volume (cm^3g^{-1})	Micropore Volume (cm^3g^{-1})
TiN[a]	15	18 ± 0.2	0.20	0.008
VN[a]	21	32 ± 0.1	0.18	0.02
VC[a]	14	6 ± 0.1	0.03	0.0004
NbN[a]	13	34 ± 0.3	0.06	0.021
NbC[a]	15	16 ± 0.1	0.05	0.01
β-W_2N[b]	6	42 ± 0.2	0.03	0.02
β-WC_{1-x}[b]	6	65 ± 0.3	0.07	0.053
γ-Mo_2N[b]	6	144 ± 0.2	0.12	0.08
α-Mo_2C[b]	6	92 ± 0.2	0.16	0.003
β-Mo_2C[c]	6	82 ± 0.2	0.13	0.007
(α+β)-Mo_2C[d]	-	88 ± 0.2	0.14	0.009

[a] Face-centered-cubic structured materials with 1:1 metal to non-metal stoichiometry

[b] Face-centered-cubic structured materials with 2:1 metal to non-metal stoichiometry

[c] Hexagonal-closed-packed structured material with 2:1 metal to non-metal stoichiometry

[d] (50% fcc + 50% hcp) structured material with 2:1 metal to non-metal stoichiometry

2.3.2. Pore Size Distributions

Figures 2.6 to 2.10 show pore size distributions for the carbides and nitrides. Consistent with the trend in the surface area, with the exception of the WC_{1-x}, the nitrides exhibit larger pore volume than their carbide counterparts. The relatively high surface area observed for WC_{1-x} as compared to W_2N is likely due to the lower synthesis temperature and nitridation steps as discussed in the synthesis section. The pore size distributions for all the materials are dominated by micro- and meso-pores (Figures 2d and 2e). The Mo and W-based materials (Figures 2.6 and 2.7) had significant micro-pore volumes. Average pore sizes for materials with 1:1 metal to non-metal stoichiometries were larger (3-100 nm) than those with 2:1 stoichiometries (1-10 nm); most likely due to the high synthesis temperatures, leading to particle growth. The α-Mo_2C and β-Mo_2C

materials showed two maxima in the pore-size distributions, while (α+β)-Mo_2C was predominated by one peak (Figure 2.6). Additionally, the pore size distribution for α-Mo_2C was predominated by large pores. Similarities in trends between the surface areas and pore size distributions of the interstitial compound carbides and nitrides could assist in correlating the crystal structure and composition of carbides and nitrides with their electrochemical properties. This is further discussed in Chapter three. Overall, the higher the surface area, the smaller the pore sizes.

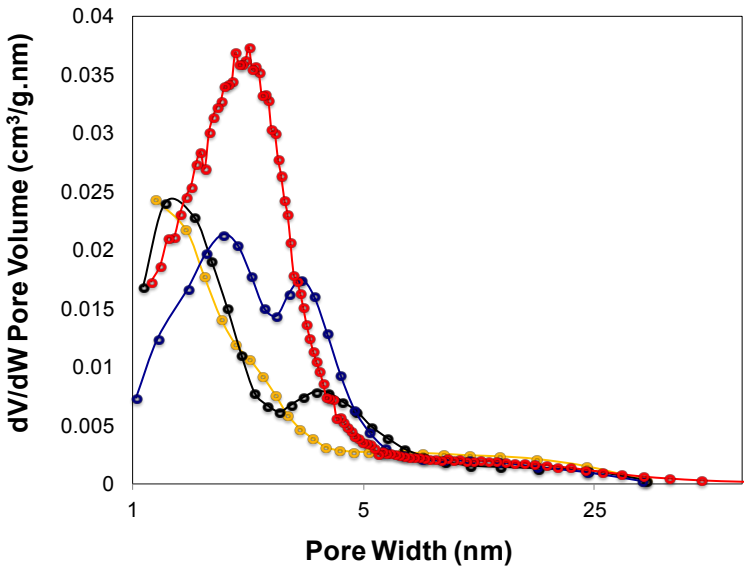

Figure 2.6: Pore size distributions for γ-Mo_2N (red), α-Mo_2C (blue), and β-Mo_2C (yellow), (α+β)-Mo_2C (black), showing micropore and mesopore ranges.

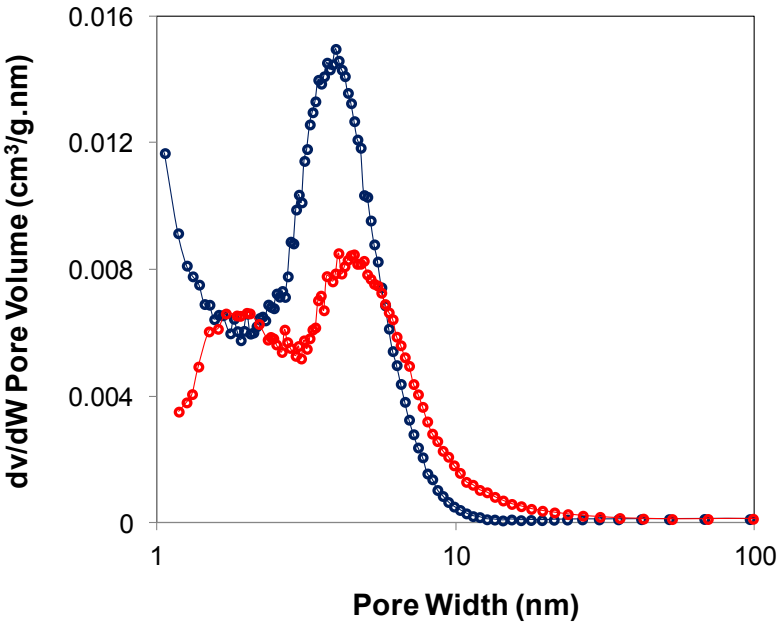

Figure 2.7: Pore size distributions for W_2N (red) and WC_{1-x} (blue), showing micropore and mesopore ranges.

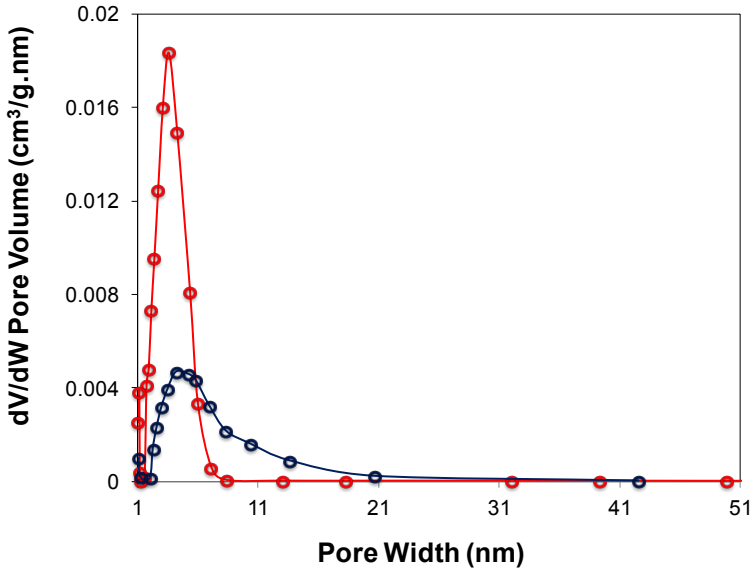

Figure 2.8: Pore size distributions for NbN (red) and NbC (blue), showing micropore and mesopore ranges.

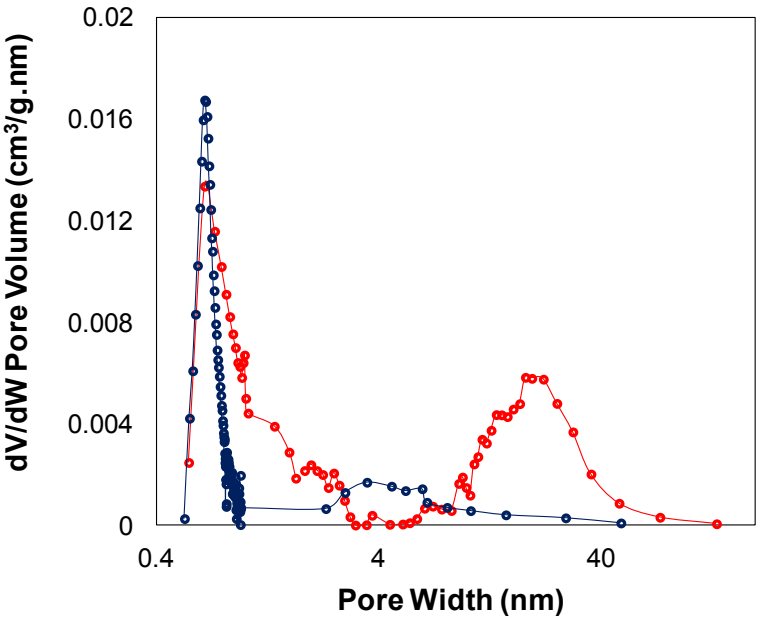

Figure 2.9: Pore size distributions for VN (red) and VC (blue), showing micropore and mesopore ranges.

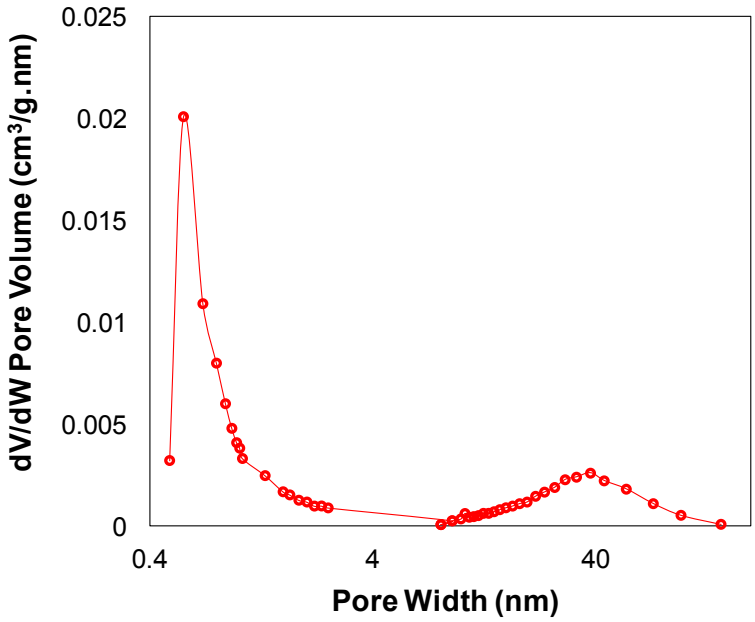

Figure 2.10: Pore size distributions for TiN, showing micropore and mesopore ranges.

2.3.3. Surface Morphologies

The SEM images for γ-Mo_2N and VN are shown in Figures 2.11 and 2.12, respectively. For completeness, morphological analysis was performed for both the powder and the electrode. The micrographs indicated that the materials are highly porous, consistent with the surface area and pore size distribution measurements. However, the resolution did not allow detailed analysis of individual pore sizes. Surface porosity is observed for both the powder materials and coated electrodes. There are subtle morphological differences between coated electrodes and powder materials. This may be a consequence of slurry coating in which the powder is mixed with a small amount of carbon and polyvinylidene fluoride, then crushed into smaller particles to facilitate the formation of a uniform mixture.

2.3.4. Surface Compositions

AES was used to determine the surface compositions of VN, VC, W_2N and WC_{1-x} electrodes. The electrodes were prepared by mixing the synthesized material (92 wt. %) with carbon black (5 wt. %, Super PLi (TIMCAL) and polyvinylidene fluoride (3 wt. %, Kynar) in N-methylpyrrolidione solvent (Alfa Aesar). The resulting slurry was spread onto a Ti foil, and then dried in vacuum at 80° C for 8 hours. The spectra for VN and VC are shown in Figure 2.13, and those for W_2N and WC_{1-x} are represented in Figure 2.15. The spectra were collected while taking SEM images as shown in Figures 2.13 and 2.15. The surface compositions (in mole percent) for VN and VC are shown in Figure 2.14, and those for W_2N and WC_{1-x} are represented in Figure 2.16. For VN, the ratio of non-metal to metal was ~1 (N/V = ~1), whereas for VC, this ratio was approximately 5 (C/V = ~5) indicating the presence of excess carbon on the VC electrode as a consequence of the synthesis procedure. Consistent with the surface area measurements, the

concentration of elements on the surfaces of W_2N and WC_{1-x} were essentially the same. The ratios of non-metal to metal were similar (see Figure 2.16). This is not unexpected given the similarities in their synthesis procedures. Similarities in trends between the surface areas and surface compositions could influence the performance and electrochemical properties of carbides and nitrides.

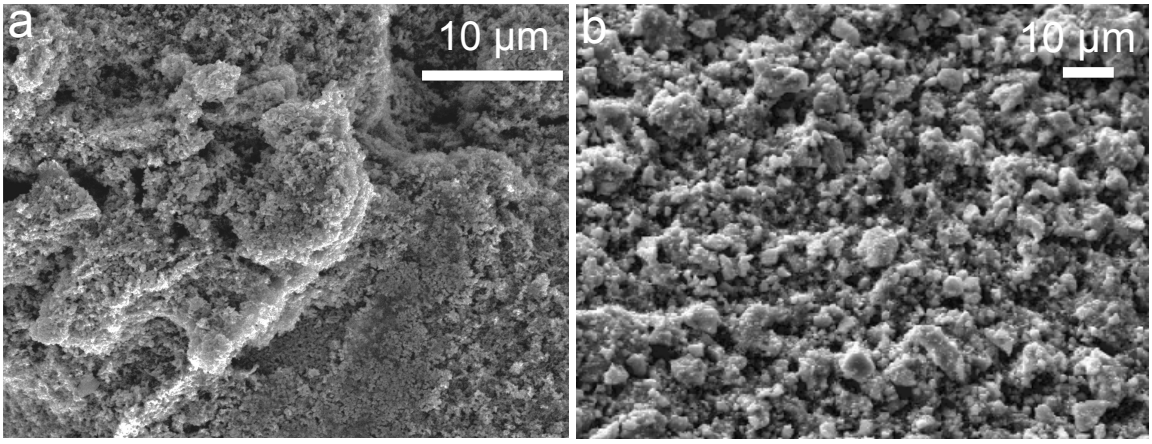

Figure 2.11: Scanning electron micrographs for γ-Mo_2N powder (a) and electrode (b), revealing the porous nature of the material.

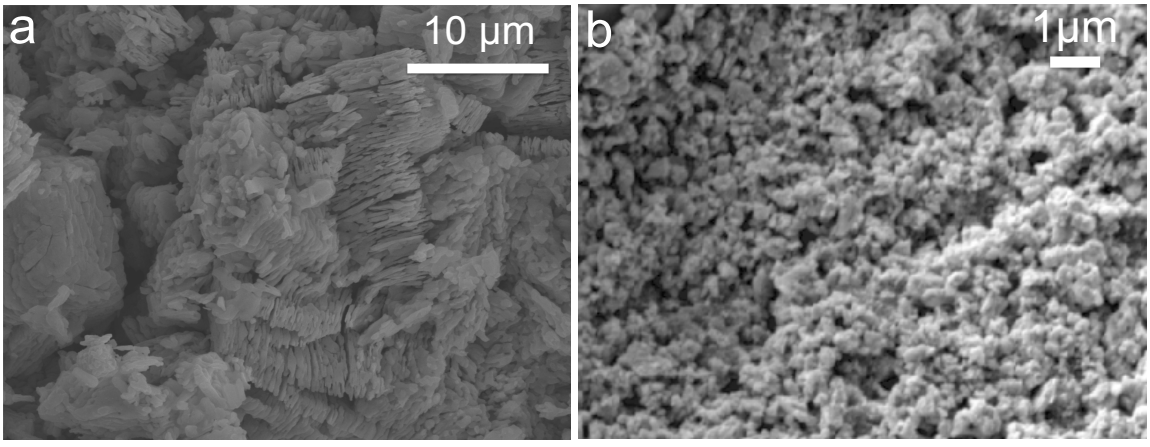

Figure 2.12: Scanning electron micrographs for VN powder (a) and electrode (b), revealing the porous nature of the material.

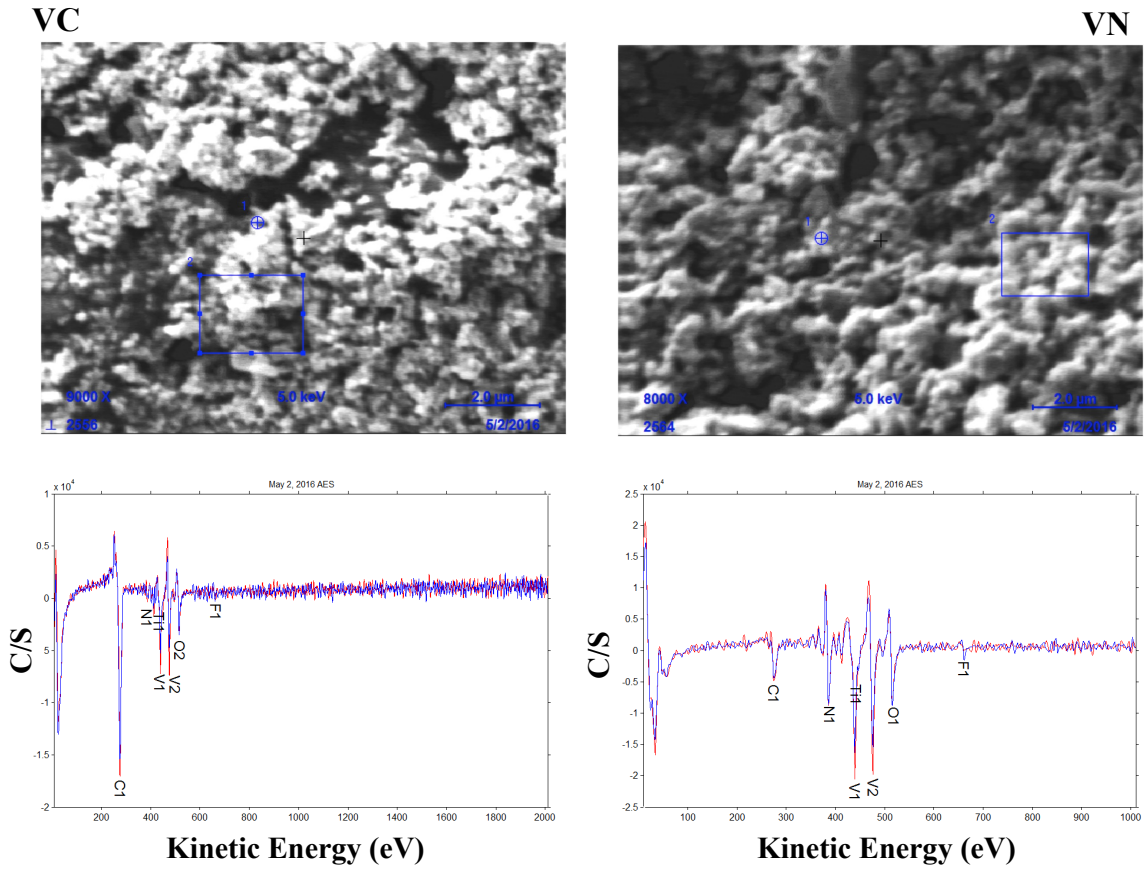

Figure 2.13: (Top) Scanning electron micrographs, (bottom) Auger electron spectroscopy data for VC and VN electrodes, The blue squares on the micrographs indicate where the Auger spectra were taken.

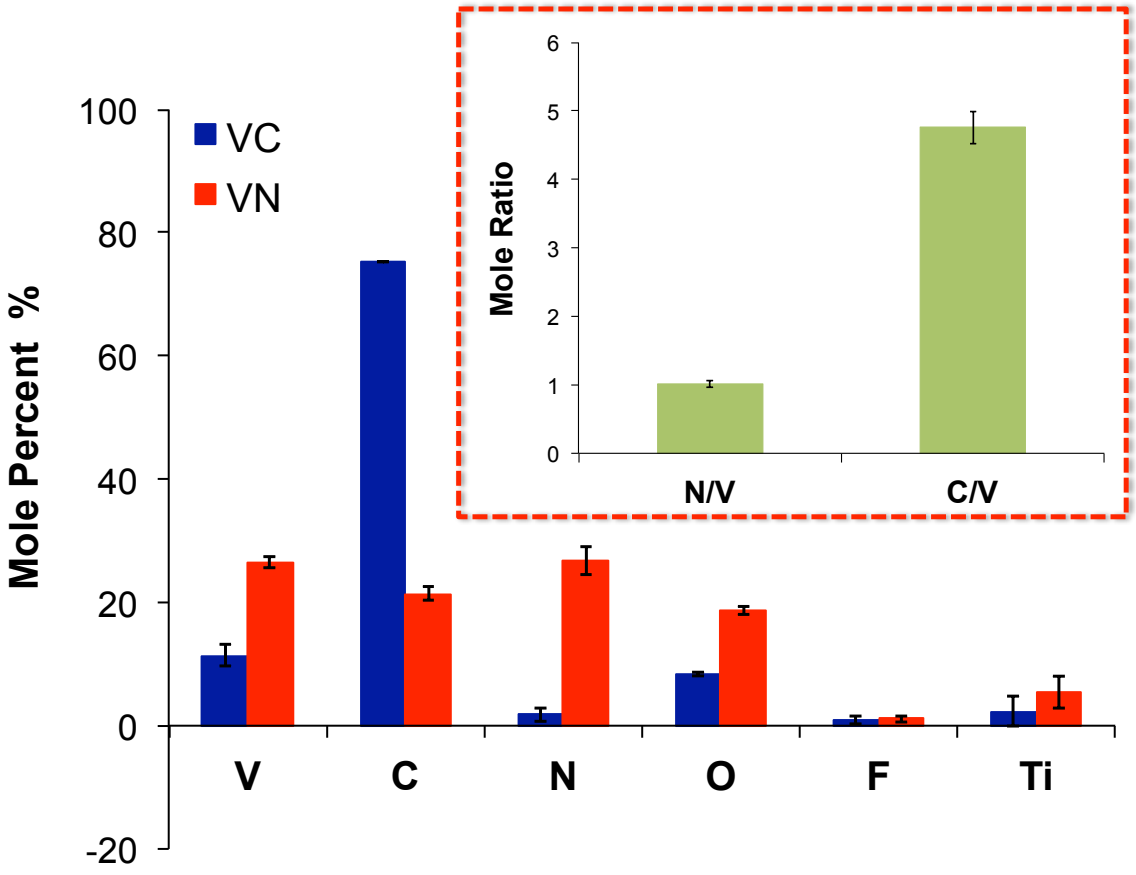

Figure 2.14: Surface compositions (in mole percent) for VC and VN electrodes, the ratio of non-metal to metal is shown in the inset.

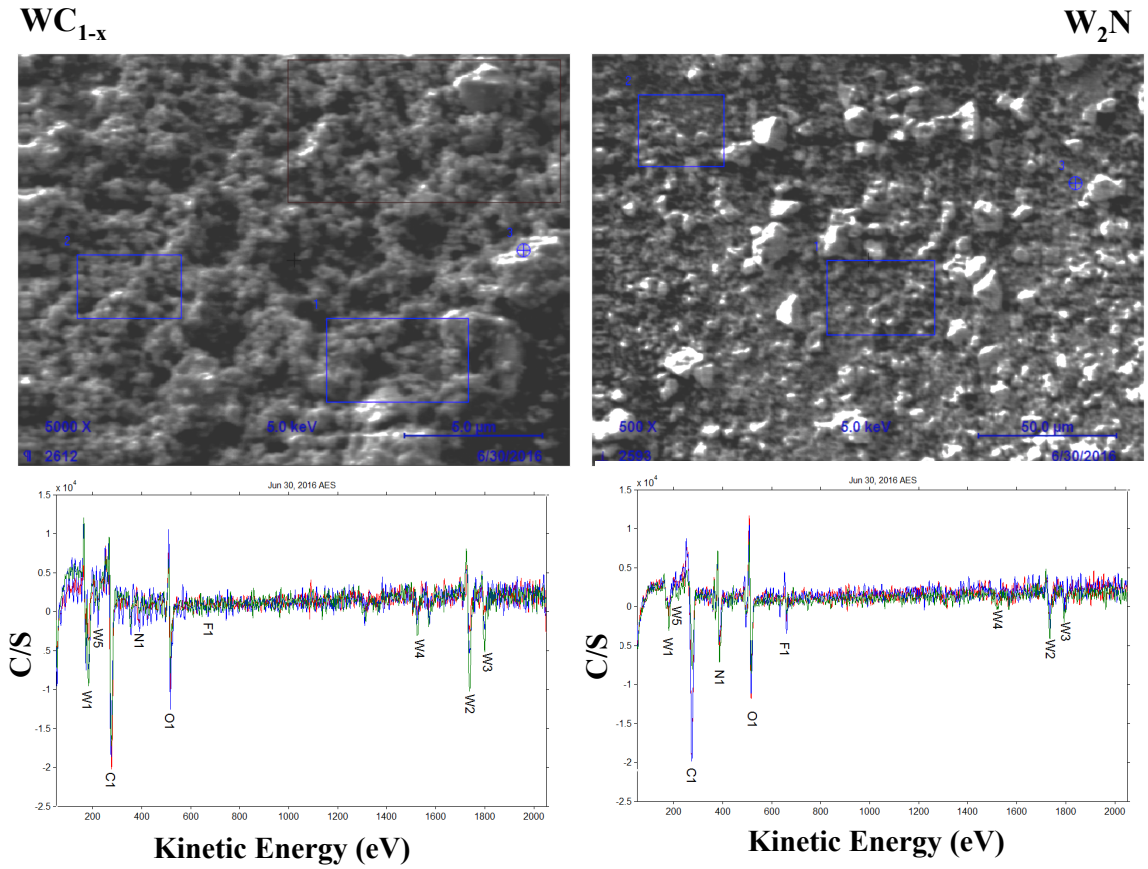

Figure 2.15: (Top) Scanning electron micrographs, (bottom) Auger electron spectroscopy data for WC_{1-x} and W_2N electrodes, The blue squares on the micrographs indicate where the Auger spectra were taken.

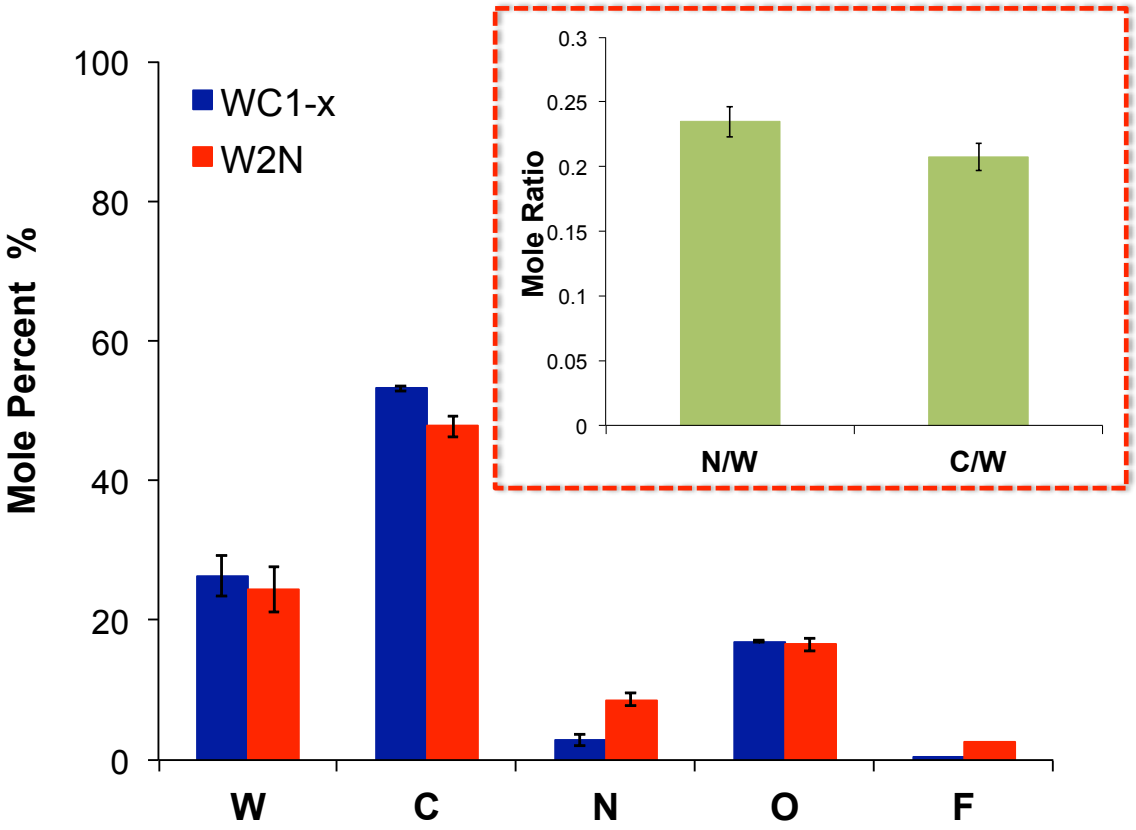

Figure 2.16: Surface compositions (in mole percent) for WC_{1-x} and W_2N electrodes, the ratio of non-metal to metal is shown in the inset.

2.4. Conclusion

Interstitial compounds, specifically early transition-metal carbides and nitrides of Ti, V, Nb, Mo, and W metals, were synthesized using a temperature-programmed reaction method**.** The materials were phase pure as confirmed by the XRD analysis. They were highly porous and possessed high surface areas and different pore size ranges (micro and meso). The pore size distributions of materials with high surface area were shifted to smaller pore sizes, consistent with the surface area measurements. The nitrides exhibited higher surface area and larger micropore pore volume as compared to the carbides. The higher surface areas observed for the nitrides were likely a consequence of

their lower crystallite size and smaller average pore size. Surface analysis revealed the presence of undesirable excess carbon on the carbides, particularly, on VC. Further improvement in the physical and surface properties of carbides will benefit from ameliorating their synthesis procedures.

2.5. References

1. S. T. Oyama, Catal. Today, 15 (1992) 179-200.
2. G. Hagg, J. Phys. Chem. 12 (1931) 33-56.
3. C. A. Bennett, Ph. D. Thesis, University of Michigan, (2002).
4. J. F. Shackelford, "Introduction to Materials Science for Engineers", 2nd ed., Macmillan, New York, (1988).
5. S. T. Oyama and G. L Haller, "Catalysis, Specialist Periodical Reports", G.C. Bond and G. Webb, Eds., Vol 5, p. 333, The Chemical Society, London, (1981).
6. L. Leclercq, "Surface Properties and Catalysis by Nonmetals", J. P. Bonnelle, B. Dehnon and E. Derouane, Eds., p. 433, Reidel, Dordrecht, (1983).
7. R. B. Levy, M. Boudart, Science, 181 (1973) 547.
8. S. T. Oyama, The Chemistry of Transition-metal Carbides and Nitrides, Chapman and Hall Publisher, (1996).
9. J. B. Claridge, A. P. E. York, A. J. Brungs, M. L. H. Green, Chem. Mater 12 (1) (2000) 132.
10. R. Kapoor, S.T. Oyama, J. Solid State Chem. 99 (1992) 303.
11. J. A. Schaidle, A. C. Lausche, L. T. Thompson, J. Catal. 272 (2010) 235.
12. L. Volpe, M. Boudart, J. Solid State Chem., 59 (1985) 332.
13. J. G. Chen, Chem. Rev. 96, 4 (1996) 1477.
14. S. Ramanathan, S. T. Oyama, J. Phys. Chem. 99, 44 (1995) 16355.
15. H. Zhong, H. Zjang, G. Liu, Y. Liang, J. Hu, B. Yi, Electrochem. Comm., 8, 5 (2006) 707.
16. M. Azuma, Y. Nakato, H. Tsubomura, J. Electrochem. Soc., 255 (1988) 179.

17. M. Glushenkov, D. Hulicova, D. Llewellyn, G. Q. Liu, Y. Chen, Chem. Mater., 22 (2010) 914.

18. D. W. Choi, G. E. Blomgren, P. N. Kumta, Adv. Mater., 18 (2006) 1178.

19. P. Pande, P. Rasmussen, L. Thompson, J. Power Sources, 207 (2012) 212-215.

20. D. Choi, P.N. Kumta, J. Am. Ceram. Soc., 94, 8 (2011) 2371.

21. T. C. Liu, W. G. Pell, B. E. Conway, J. Electrochem.Soc., 145 (6) (1998) 1882.

22. M. R. Wixom, D. J. Tarnowski, J. M. Parker, J. Q. Lee, P. L. Chen, I. Song, L. T. Thompson, Mat. Res. Soc. Symp. Proc., 496 (1998) 643.

23. X. Zhou, C. Shang, S. Doug, X. Chen, P. Han, L. Li, J. Yao, Z. Liu, H. Xu, Y. Zhu, G. Cui, Appl. Mater. Interfaces, 3 (2011) 3058

24. S. L. Roberson, D. Finello, R. F. Davis, J. Appl. Electrochem., 29 (1999) 75.

25. R. L. Porto, R. Frappier, J.B. Ducros, C. Aucher, H. Mosqueda, S. Chenu, B. Chavillon, F. Tessier, F. Cheviré, T. Brousse, Electrochimica Acta 82 (2012) 257-262.

26. P. Pande, A. Deb, A. S. Sleightholme, A. Djire, P. Rasmussen, J. Penner-Hahn, L. T. Thompson, J. Power Sources, 289 (2015) 154-159.

27. G. Hasegawa, A. Kitada, S. Kawasaki, K. Kanamori, K. Nakanishi, Y. Kobayashi, H. Kageyama, T. Abe, J. of Electrochemical Soc., 162 (1) (2015) A77-A85.

28. O. Kartachova, A. M. Glushenkov, Y. Chen, H. Zhang, X. J. Dai, Y. Chen, J. Power Sources, 220 (2012) 298-305.

29. A. Djire, O. Ajenifujah, A. Sleightholme, P. Rasmussen, L. T. Thompson, J. Power Sources, 207 (2015) 212-215.

30. D. Choi, P.N. Kumta, J. Am. Ceram. Soc. 90 (2007) 3113-3120.

31. A. R. Ko, S.B. Han, Y.W. Lee, K.W. Park, Phys. Chem. Chem. Phys. 13 (2011) 12705-12707.

32. B. E. Conway, J. Electrochem. Soc., 6 (1991) 138.

33. R, J. O'Brien, L. Xu, X. X. Bi, P. C. Eklund, B. H. Davis, The Chemistry of Transition Metal Carbides and Nitrides; Oyama, S.T., Ed.; Blackie Academic & Professional: Glasgow, Scotland, (1996) 362-372.

34. M. J. Ledoux, C. Pham-Huu, Catal. Today 15 (1992) 263.

35. M. J. Ledoux, S. Hantzer, C. Pham-Huu, J. Guille, M. P. J. Desaneaux, J. Catal. 114 (1988) 176.

36. R. W. Chorley, P. W. Lednor, Adv. Mater., 3 (1991) 474.

37. J. M. Giraudon, L. Leclercq, G. Leclercq, A. Lofberg, A. Frennet, J. Mater. Sci., 28 (1993) 2449.

38. D. Zeng, M. Hampden-Smith, J. Chem. Mater., 4 (1992) 968.

39. B. D. Cullity, S. R. Stock, Elements of X-ray Diffraction, Vol 2, Addison Wesley Reading, MA, (1978).

40. http://www.micromeritics.com/Repository/Files/Gas_Sorption.pdf

Chapter 3

Electrochemical Properties

3.1. Introduction

Early transition-metal carbides and nitrides have shown promise for use in high energy density supercapacitors. Their further development would benefit from an understanding of the effects of crystal structure and composition on performance. This chapter describes results for phase-pure, nanostructured, face-centered cubic (fcc) and hexagonal-closed-packed (hcp) early transition metal (Ti, V, Nb, Mo, and W) carbides and nitrides that were synthesized using a temperature-programmed reaction method as described in chapter two. The materials were characterized electrochemically in aqueous H_2SO_4 and KOH electrolytes. In voltage windows where the materials were electrochemically stable, the results are most consistent with charge storage via a pseudocapacitive mechanism in both electrolytes. The fcc- and hcp-based structures Mo_2C materials showed different electrochemical properties. Because of their larger pore sizes, fcc-Mo_2C had improved ion transport and higher capacitance in KOH electrolyte. The nitrides had higher areal specific capacitances than the carbides. In terms of metal, V exhibited the highest areal specific capacitance in its nitride form, while in their carbide form, Mo and W metals showed improved charge storage capacity. The lower performance observed for carbides is attributed to excess amorphous carbon deposited on the materials during synthesis, as corroborated by results from Auger electron

spectroscopy (see chapter two). Electrolytes active ions interact more frequently with the carbon than the carbide. Such an interaction leads to electrostatic double-layer storage.

The extent of pseudocapacitance exhibited by the carbides and nitrides in aqueous electrolytes was investigated using cyclic voltammetry and electrochemical impedance spectroscopy. The contribution of pseudocapacitance to charge storage in all carbides and nitrides was much higher than double-layer capacitance and ranged from 63% for TiN to 87% for VN in acidic electrolyte. These findings serve as useful correlation and prediction tools for the design of higher-energy density electrochemical supercapacitors based on early transition-metal carbides and nitrides.

3.2. Experimental Methods

3.2.1. Procedure

The electrochemical characterization was carried out using cyclic voltammetry (CV) and electrochemical impedance spectroscopy (EIS) in a three-electrode electrochemical cell (ECC-Aqu, EL-Cell FmbH, Germany) with 0.1 mol dm^{-3} H_2SO_4 and 0.1 mol dm^{-3} KOH electrolytes. The cell was assembled with an 18 mm diameter glass fiber separator of thickness 1.55 mm. An 18 mm diameter activated carbon fabric counter electrode (CE) (Kynol ACC-507-15, sp. S. A. 1500 m^2g^{-1}, thickness 0.54 mm) was used. A schematic of the cell is shown in Figure 3.1. The working electrode (WE) was prepared by mixing the synthesized material (92 wt. %), carbon black (5 wt. %, Super PLi (TIMCAL) and polyvinylidene fluoride (3 wt. %, Kynar) in N-methylpyrrolidione solvent (Alfa Aesar). The resulting slurry was spread onto a Ti foil, the current collector (CC), and then dried in vacuum at 80°C for 8 hours. The mass of the active material was

determined by subtracting the mass of the Ti substrate from the mass of the coated electrode (Ti + active material). Approximately 3 mg of active material was coated on the substrate. The working electrode diameter was 16 mm, to ensure an even current distribution between counter and working electrodes. A Pt wire (1 mm diameter) was used as the reference electrode (RE). Pt wire electrodes have been shown to be electrochemically stable in aqueous electrolytes, and can be used as a reference electrode under appropriate conditions [1]. The CE and separator were soaked in electrolyte overnight to ensure better wettability, and de-aerated with nitrogen for at least 30 min before assembling the cell. The measurements were performed using an Autolab PGSTAT302N potentiostat.

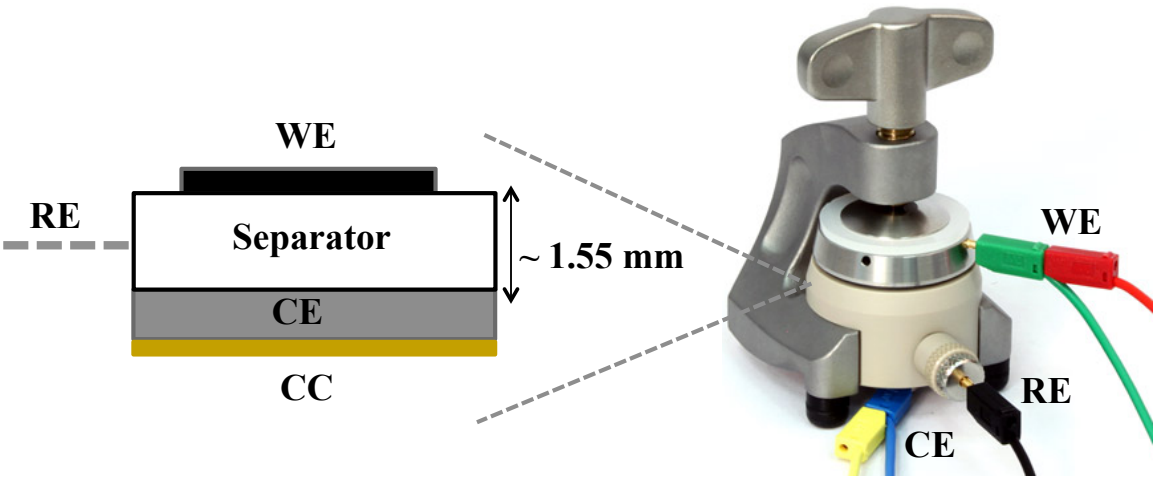

Figure 3.1: Schematic of the three-electrode electrochemical cell (ECC-Aqu, EL-Cell FmbH, Germany), showing separator and working, counter, and reference electrodes.

3.2.2. Analysis Techniques

3.2.2.1. Cyclic Voltammetry (CV)

CV analysis was used to determine the stable operating voltage window, capacitance, the dependence of capacitance on the scan rate, and faradaic redox activities

of the carbides and nitrides electrodes. CV is a potentiodynamic electrochemical measurement that measures the current response of a system under conditions where the potential is applied. In a CV experiment the WE potential is ramped linearly between two set potentials at a set rate. These cycles of ramps in potential may be repeated as many times as desired. The current at the WE is plotted versus the applied potential to give rise to the cyclic voltammogram trace. The potential and current response of the WE are measured with respect to the RE (with known standard stable potential) and CE (with high surface area), respectively.

The specific capacitances, C, were estimated by integrating the area under the cyclic voltammograms according to [2,3]:

$$C = \frac{\int_{V_{cathodic}}^{V_{anodic}} IdV}{mv(V_{anodic} - V_{cathodic})} \quad (1)$$

where I is the current, V_{anodic} is the anodic limit, $V_{cathodic}$ is the cathodic limit, m is the mass of active material, and v is the voltage scan rate. The areal specific capacitance for all the materials was obtained by normalizing the specific capacitance to the BET surface area (from chapter two).

3.2.2.2. Electrochemical Impedance Spectroscopy (EIS)

EIS analysis was used to measure the pseudocapacitance and double-layer capacitance. EIS has been recognized as one of the principal methods for examining the fundamental behavior of electrode materials. In EIS, the potential of the WE is modulated (typically with a low amplitude modulation of ≤ 10 mV) over a wide frequency range from 1 mHz to 1 MHz and the current response of the system is then recorded and

evaluated. This frequency response can be fit to an equivalent circuit model to simulate the behavior of the actual system.

In this study, EIS measurements were performed at selected potentials within the stable potential window. A low amplitude modulation of 10 mV and a wide frequency range from 1 mHz to 100 kHz was used. Using this approach, an experimental distinction was made between pseudocapacitance and double-layer capacitance as they display different orders of relaxation time constants [3].

3.3. Results and Discussion

3.3.1. Electrochemical Properties

The stable operating voltage windows were determined by cycling the materials in H_2SO_4 and KOH electrolytic solutions at 50 mV s^{-1}. The voltage window was expanded from the open circuit voltage (OCV) to more negative and positive voltages in increments of 100 mV until the material showed evidence of irreversible reactions (e.g. H_2 or O_2 evolution). Stability was verified by cycling the materials for at least 100 scans. For most materials, the cyclic voltammograms (10^{th}, $50^{th,}$ and 100^{th} cycles) overlapped indicating materials stability. Figures 3.2 to 3.6 show overlapped cyclic voltammograms collected at 50 mV s^{-1} for all the carbides and nitrides. Additionally, voltammograms collected at lower scan rate (2 mV s^{-1}) are also plotted in an effort to identify the faradaic redox processes occurring on the surface of the materials. The γ-Mo_2N material shows sign of instability in KOH electrolyte (see Figure 3.6b). The (α+β)-Mo_2C material shows slight variation in the first few cycles in H_2SO_4 electrolyte (see Figure 3.6c) due to lack of full wettability, though the voltammograms gradually overlapped with cycling suggesting material stability.

Table 3.1 lists the electrochemical stability windows, specific capacitances and areal specific capacitances recorded at 50 mV s^{-1} for all of the materials. With the exception of Mo carbides in both H_2SO_4 and KOH electrolytes and NbN in KOH, all of the materials were stable over > 0.8 V with large overpotentials for the H_2 evolution reaction. Other than NbC and VC in acidic electrolyte, all of the materials had specific capacitances higher than those expected for double-layer charging, which is typically on the order of 40 μF cm^{-2} for porous materials [4]. This result implicated a pseudocapacitive charge-storage mechanism. For most of the materials, voltammograms collected at low scan rate show faradaic redox peaks, consistent with a pseudocapacitive charge storage mechanism.

To better understand the pseudocapacitive mechanism, the dependence of the capacitances of the carbides and nitrides on the scan rate (between 2 and 2000 mV s^{-1}) was evaluated in H_2SO_4 and KOH aqueous electrolytes (see Figures 3.7 to 3.11). Most of the materials exhibited pseudocapacitive charge storage, as demonstrated by the logarithmic relation between capacitance and scan rate [4-7]. For materials exhibiting only double-layer charge storage, varying the scan rate does not significantly affect the measured capacitance, [4]. All the materials exhibited a negligible capacitance at the highest scan rate (~2000 mV s^{-1}). At high scan rate, diffusion limitations slow the accessibility of active ions to the inner surface of the material; consequently some pores, particularly micropores, remain inaccessible [4,8]. The highest total capacitance was achieved at the lowest scan rates (~2 mV s^{-1}). Changes in the capacitances for NbC in both electrolytes and VC in acidic electrolyte (see Figures 3.8 and 3.9b) with scan rate were negligible, suggesting solely double-layer charge storage.

Table 3.1: Electrochemical properties of early transition-metal carbides and nitrides in aqueous electrolytes, capacitance data collected at 50 mV s^{-1}, all data collected at room temperature.

Material	Voltage Window (V)	Specific Capacitance (F g^{-1}) [a]	Areal Specific Capacitance (μF cm^{-2}) [b]
TiN	0.9 (H_2SO_4)	24	134
	1.6 (KOH)	27	148
VN	1.3 (H_2SO_4)	83	243
	1.1 (KOH)	103	303
VC	0.8 (H_2SO_4)	0.24	2.72
	1.1 (KOH)	7.90	88
NbN	1.3 (H_2SO_4)	11	32
	0.6 (KOH)	45	131
NbC	0.8 (H_2SO_4)	1.92	12
	1.1 (KOH)	21.1	131
β-W_2N	0.9 (H_2SO_4)	76	122
	1.2 (KOH)	66	98
β-WC_{1-X}	1.15 (H_2SO_4)	43	67
	0.9 (KOH)	143	220
γ-Mo_2N	1.2 (H_2SO_4)	188	138
	1.2 (KOH)	116	85
α-Mo_2C	0.6 (H_2SO_4)	84	86
	0.7 (KOH)	46	47
β-Mo_2C	0.7 (H_2SO_4)	42	51
	0.7 (KOH)	39	47
(α+β)-Mo_2C	0.7 (H_2SO_4)	36	41
	0.6 (KOH)	44	50

[a] Specific capacitances estimated using equation 1 at 50 mVs^{-1}, scan 100

[b] Areal specific capacitance determined from specific capacitance and BET surface area

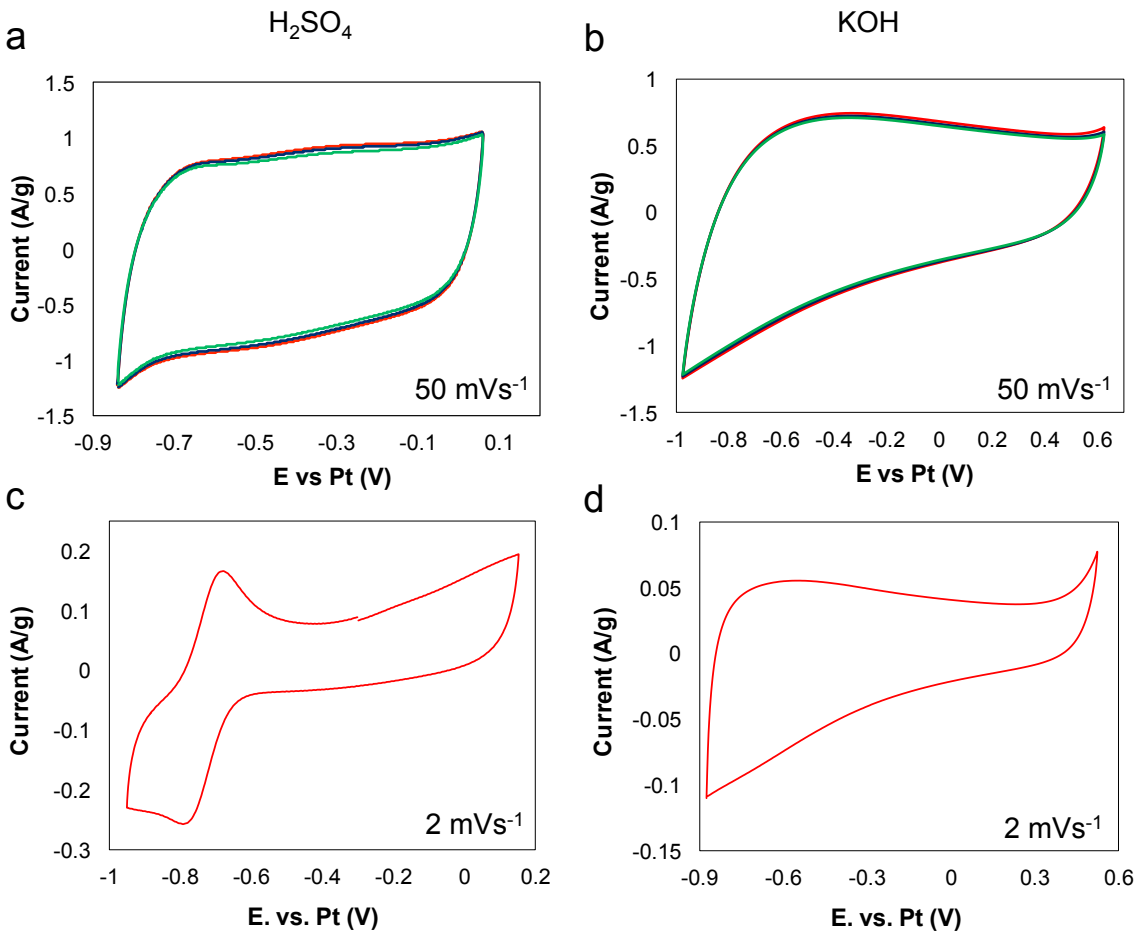

Figure 3.2: Cyclic voltammograms for TiN in 0.1 mol dm^{-3} (left) H_2SO_4 and (right) KOH; (a) and (b) were collected at 50 mVs^{-1} showing cycles 10^{th} (red), 50^{th} (blue) and 100^{th} (green); (c) and (d) were collected at 2 mVs^{-1} showing 2^{nd} cycle; all data recorded at room temperature.

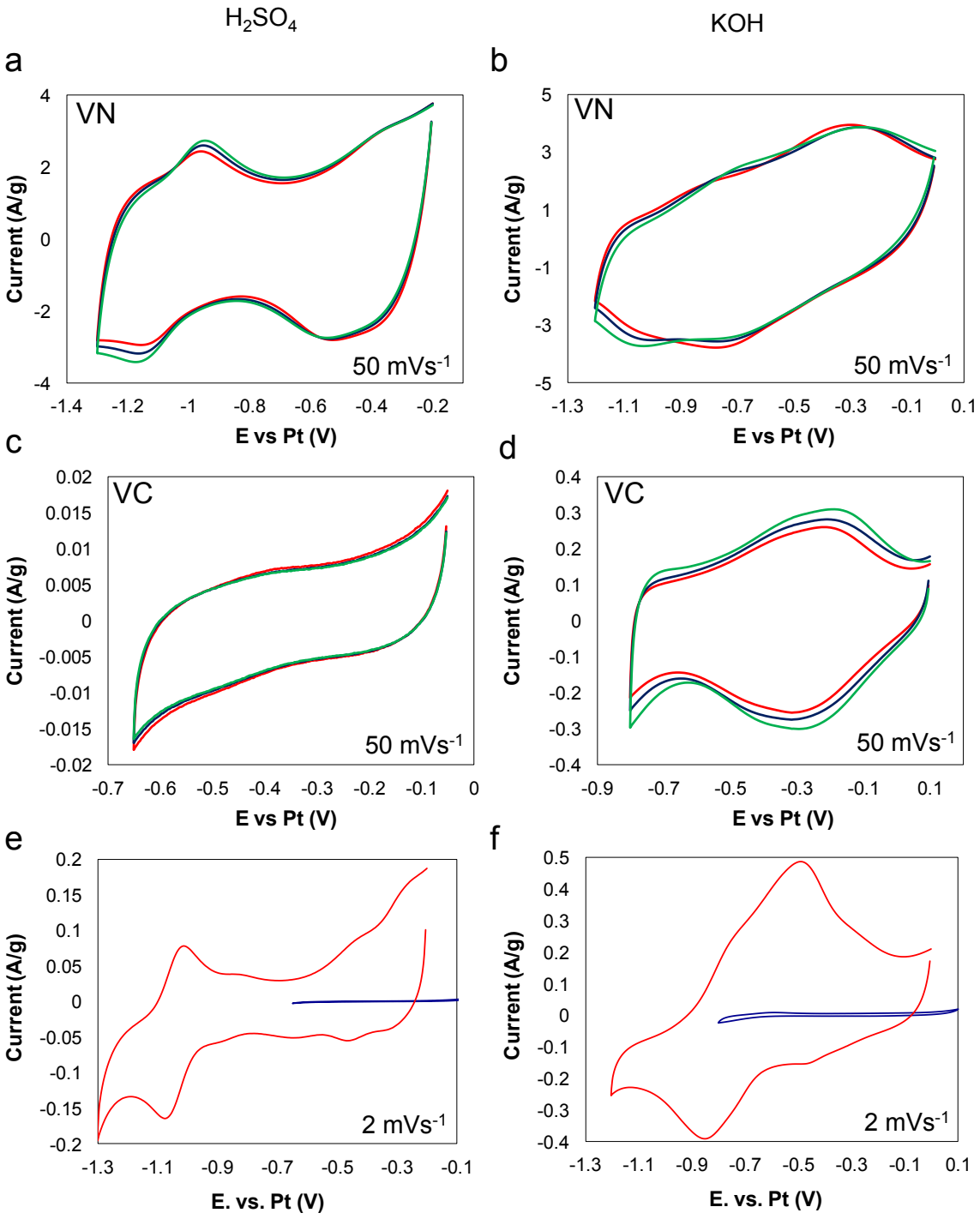

Figure 3.3: Cyclic voltammograms for VN (a) and (b) and VC (c) and (d) at 50 mVs^{-1} showing cycles 10^{th} (red), 50^{th} (blue) and 100^{th} (green); (e) and (f) for VN (red) and VC (blue) at 2 mVs^{-1} showing 2^{nd} cycle, all data recorded at room temperature in 0.1 mol dm^{-3} (left) H_2SO_4 and (right) KOH.

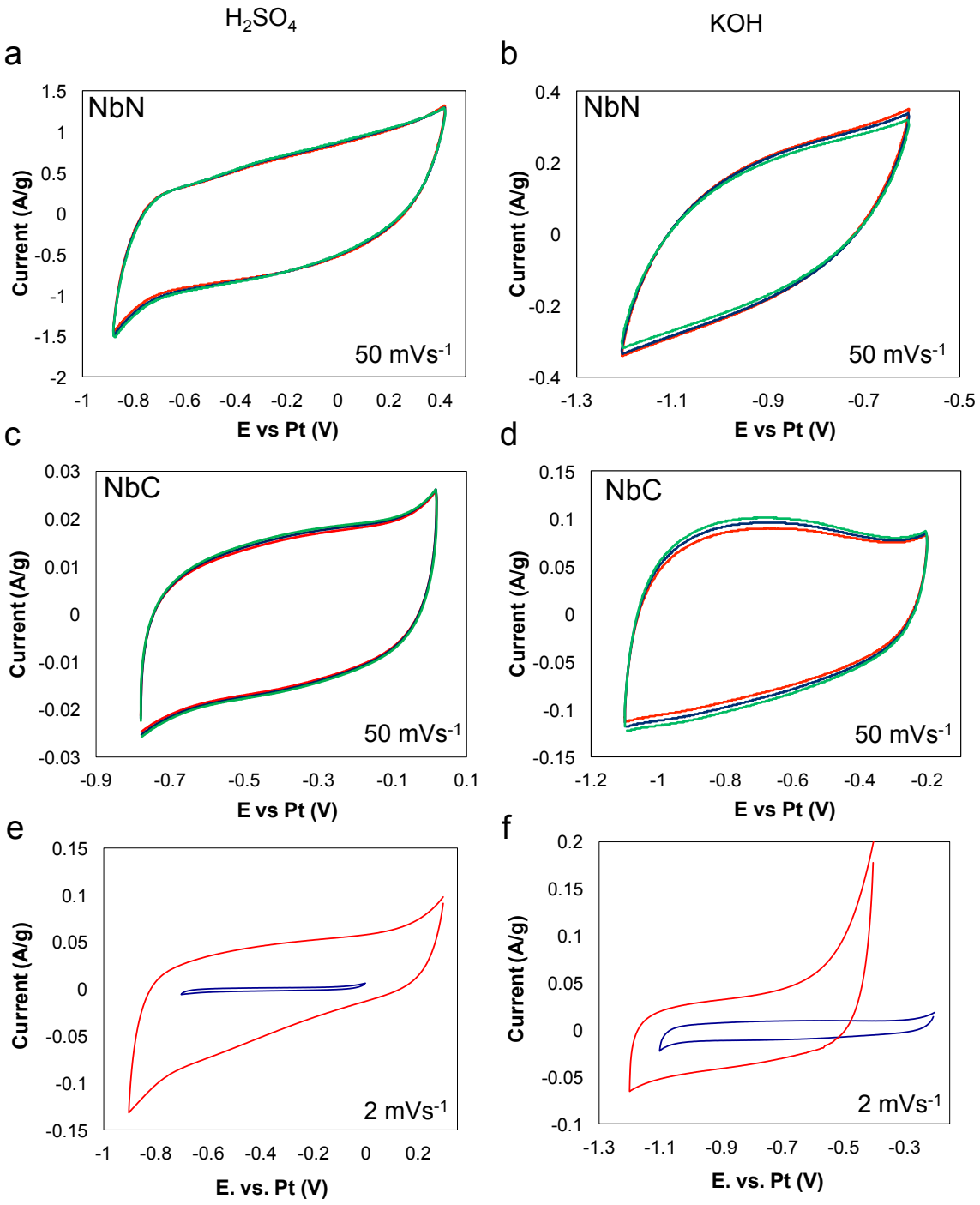

Figure 3.4: Cyclic voltammograms for NbN (a) and (b) and NbC (c) and (d) at 50 mVs^{-1} showing cycles 10^{th} (red), 50^{th} (blue) and 100^{th} (green); (e) and (f) for NbN (red) and NbC (blue) at 2 mVs^{-1} showing 2^{nd} cycle, all data recorded at room temperature in 0.1 mol dm^{-3} (left) H_2SO_4 and (right) KOH.

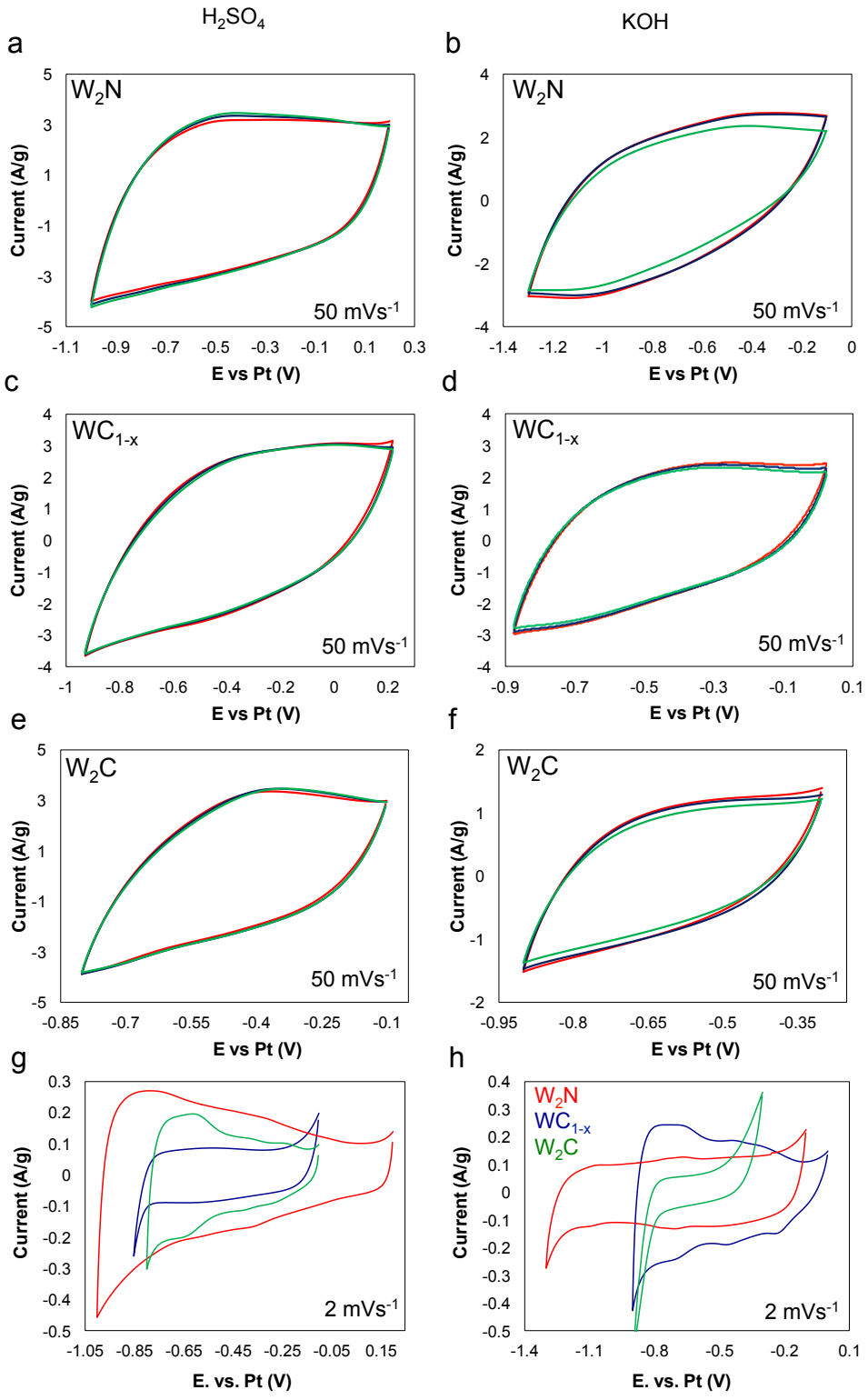

Figure 3.5: Cyclic voltammograms for W_2N (a) and (b), WC_{1-x} (c) and (d), and W_2C (e) and (f) at 50 mVs^{-1} showing cycles 10^{th} (red), 50^{th} (blue) and 100^{th} (green); (e) and (f) for W_2N (red), WC_{1-x} (blue), and W_2C (green) at 2 mVs^{-1} showing 2^{nd} cycle, all data recorded at room temperature in 0.1 mol dm^{-3} (left) H_2SO_4 and (right) KOH.

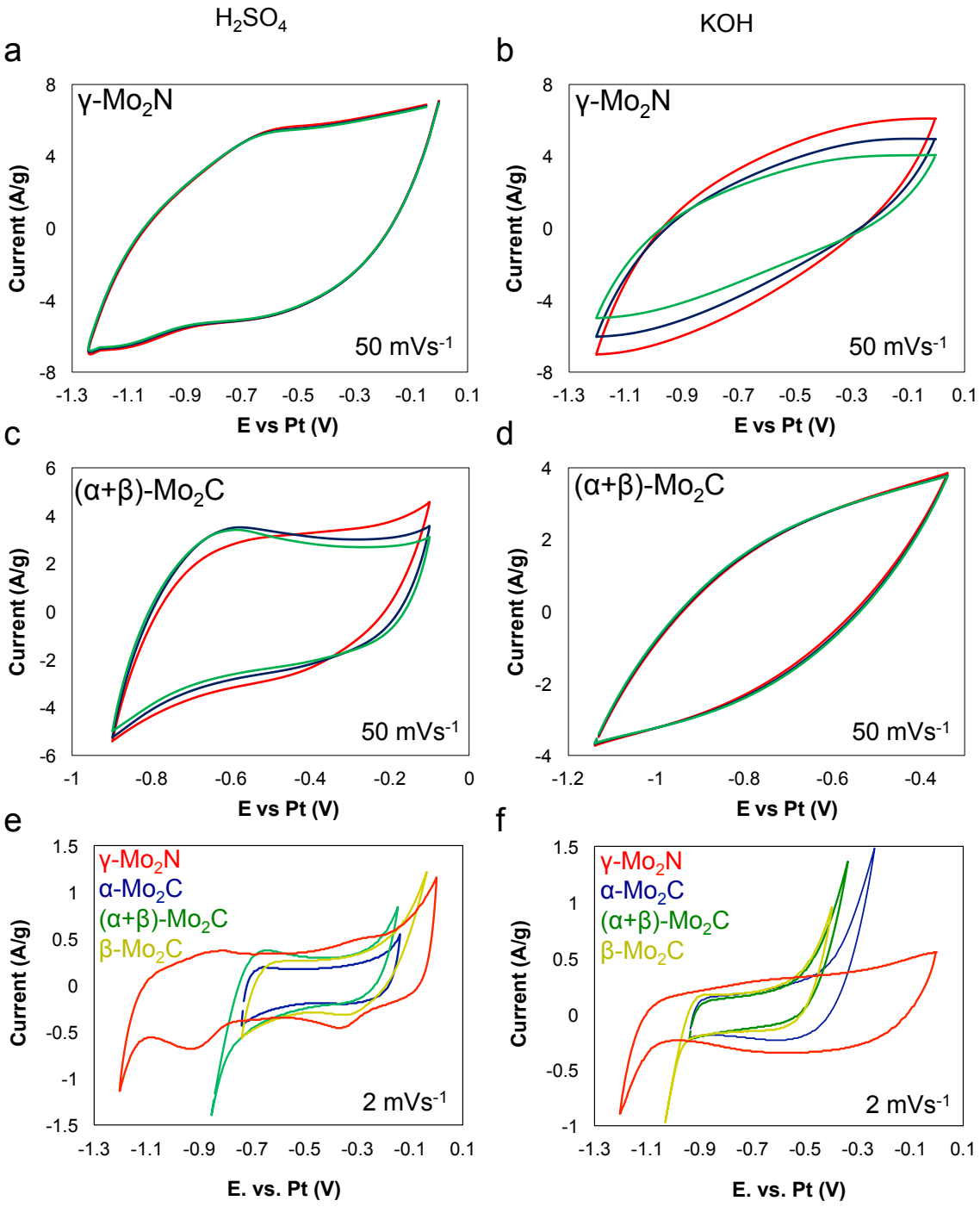

Figure 3.6: Cyclic voltammograms for γ-Mo_2N (a) and (b) and (α+β)-Mo_2C (c) and (d) at 50 mVs^{-1} showing cycles 10th (red), 50th (blue) and 100th (green); (e) and (f) for γ-Mo_2N (red), α-Mo_2C (blue), (α+β)-Mo_2C (green) and β-Mo_2C (yellow) at 2 mVs^{-1} showing 2nd cycle, all data recorded at room temperature in 0.1 mol dm^{-3} (left) H_2SO_4 and (right) KOH.

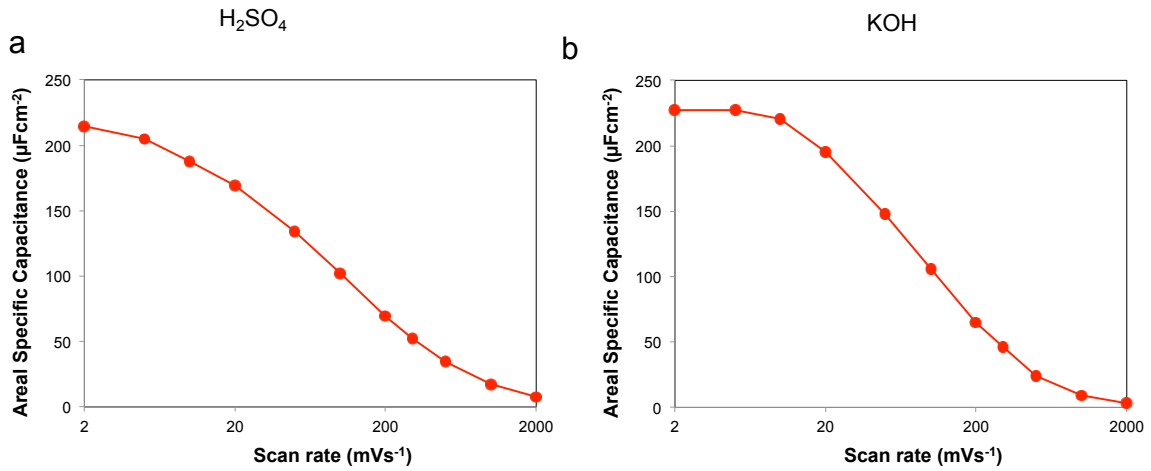

Figure 3.7: Areal specific capacitances as function of scan rate for TiN in 0.1 mol dm^{-3} (a) H_2SO_4 and (b) KOH, all data recorded at room temperature.

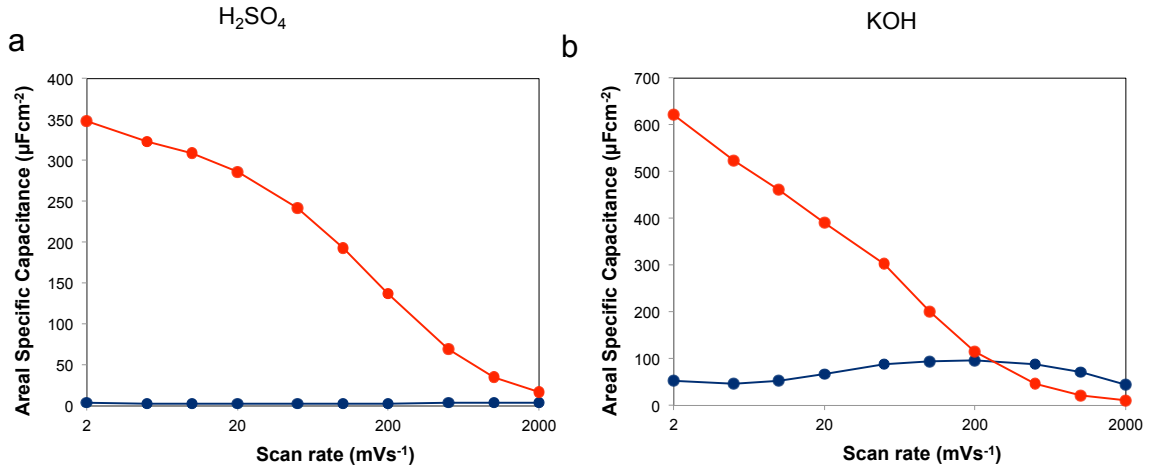

Figure 3.8: Areal specific capacitances as function of scan rate for VN (red) and VC (blue) in 0.1 mol dm^{-3} (a) H_2SO_4 and (b) KOH, all data recorded at room temperature.

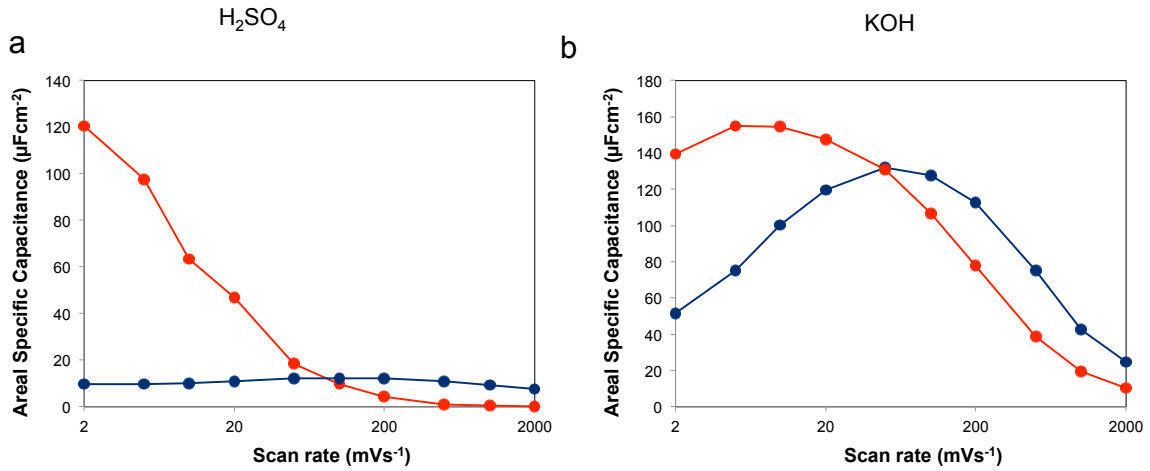

Figure 3.9: Areal specific capacitances as function of scan rate for NbN (red) and NbC (blue) in 0.1 mol dm^{-3} (a) H_2SO_4 and (b) KOH, all data recorded at room temperature.

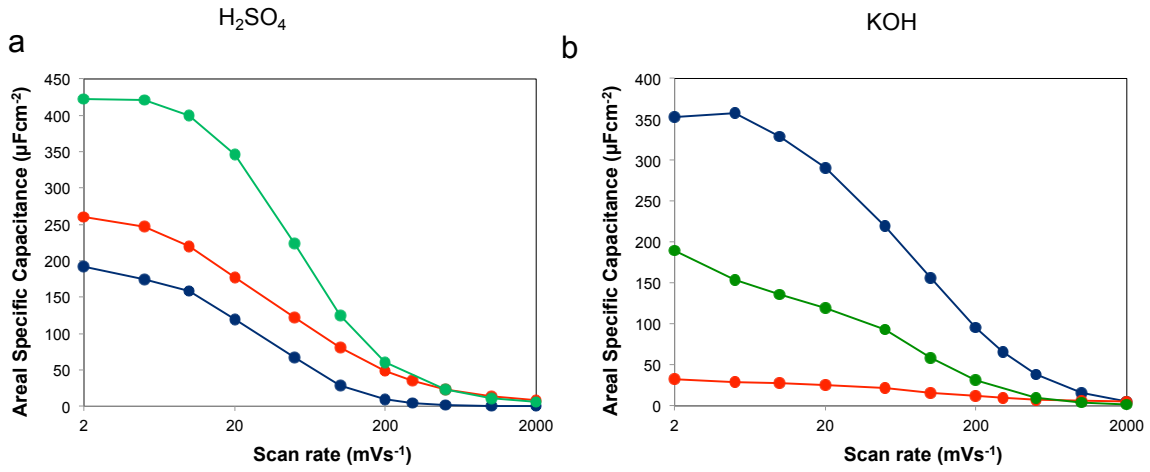

Figure 3.10: Areal specific capacitances as function of scan rate for W_2N (red), WC_{1-x} (blue) and W_2C (green) in 0.1 mol dm^{-3} (a) H_2SO_4 and (b) KOH, all data recorded at room temperature.

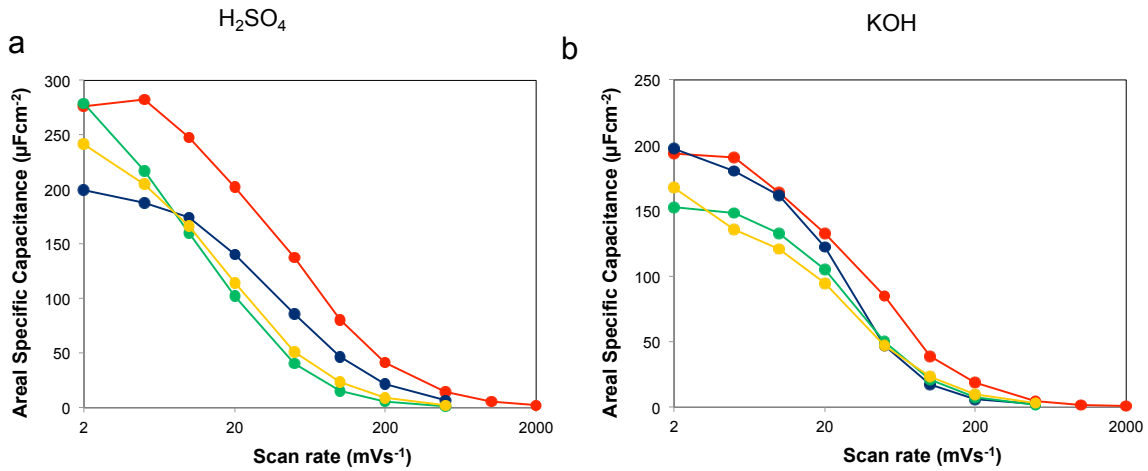

Figure 3.11: Areal specific capacitances as function of scan rate for γ-Mo_2N (red), α-Mo_2C (blue), (α+β)-Mo_2C (green) and β-Mo_2C (yellow) in 0.1 mol dm^{-3} (a) H_2SO_4 and (b) KOH, all data recorded at room temperature.

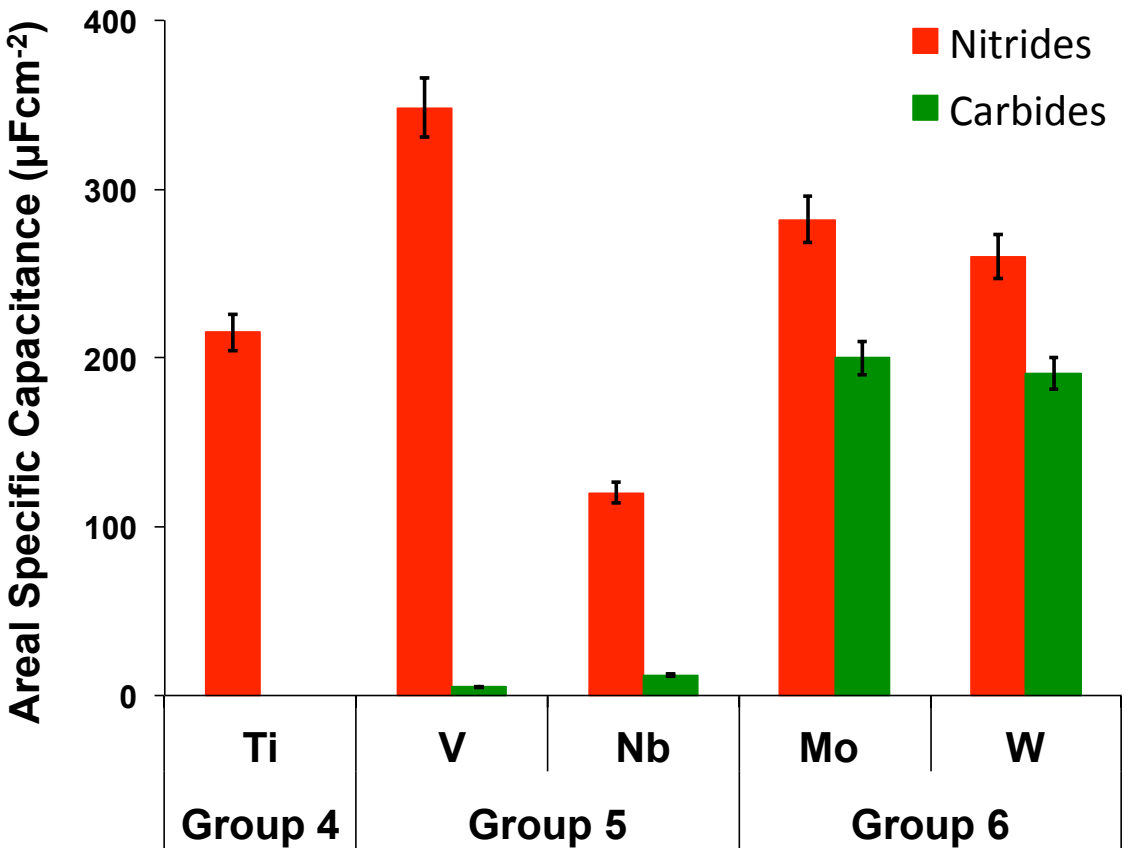

Figure 3.12: Clustered bar chart of total areal specific capacitance as a function of composition for fcc structures of early transition-metal nitrides (red) and carbides (blue), in 0.1 mol dm^{-3} H_2SO_4, all data recorded at room temperature.

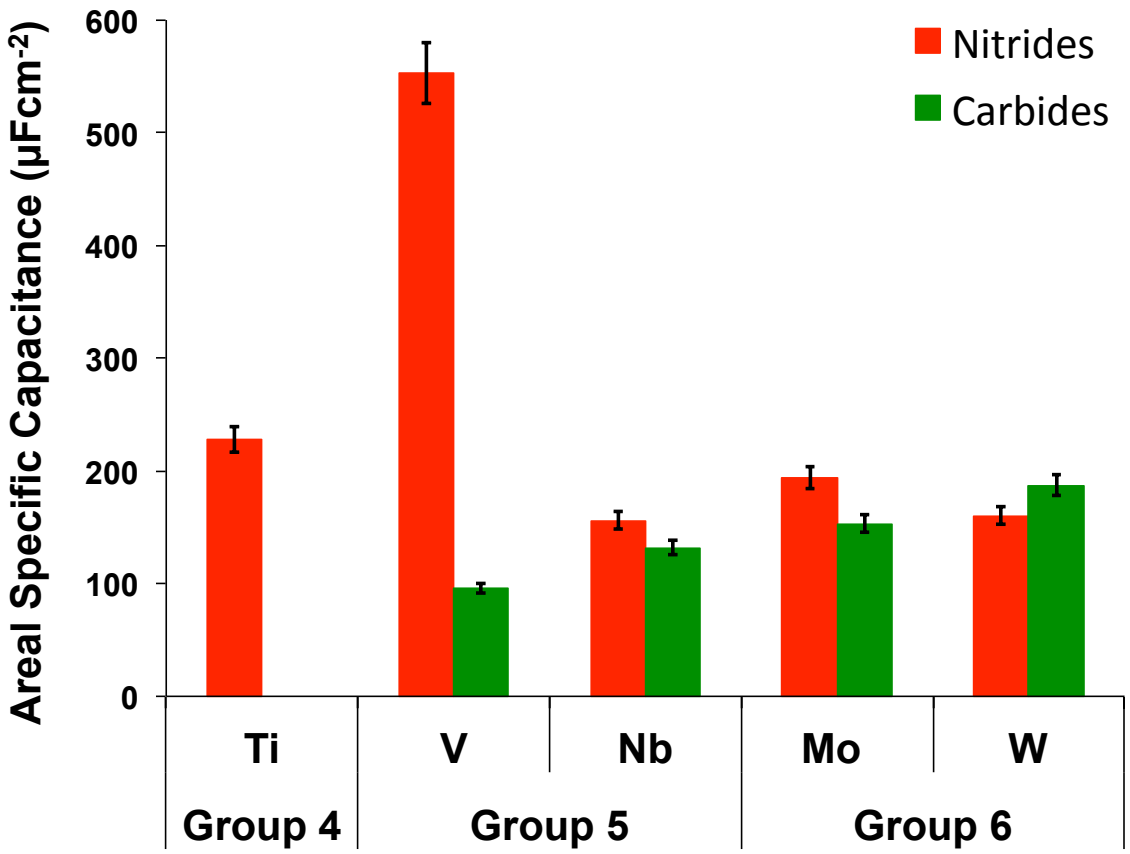

Figure 3.13: Clustered bar chart of total areal specific capacitance as a function of composition for fcc structures of early transition-metal nitrides (red) and carbides (blue), in 0.1 mol dm^{-3} KOH, all data recorded at room temperature.

3.3.2. Effects of Crystal Structure on Charge Storage

Because of their larger pore size, we hypothesized that fcc-Mo_2C materials would have better ion transport than hcp-Mo_2C materials. To test this hypothesis, we compared properties of α-Mo_2C (fcc), β-Mo_2C (hcp) and (α+β)-Mo_2C (a mixture of 50% α-Mo_2C and 50% β-Mo_2C). In KOH electrolyte, the α-Mo_2C material possessed higher areal specific capacitance than the β-Mo_2C and (α+β)-Mo_2C materials (Figure 3.11b). This is most likely due to its larger pore size (3.2 nm), which is sufficiently wide enough for the adsorption and desorption of solvated OH^- ions, consistent with our hypothesis. In H_2SO_4

electrolyte, the areal specific capacitances for the mixture, (α+β)-Mo_2C, and β-Mo_2C were higher than that for α-Mo_2C (Figure 3.11a). This suggests higher adsorption of H^+ in smaller pores (~1.5 nm) during charge storage. In terms of operating voltage window, similar voltage ranges were observed for all three materials in both aqueous H_2SO_4 and KOH electrolytes (see Table 3.1).

3.3.3. Effects of Composition on Charge Storage

To isolate the effect of composition on the capacitance, we compared the electrochemical properties of the fcc metal (Ti, V, Nb, Mo, and W) carbides and nitrides. To account for any variations due to the synthesis procedures, capacitances normalized to the surface areas were plotted as a function of composition (metal and non-metal) (see Figures 3.12 and 3.13). In general the nitrides possessed higher areal specific capacitances than the carbides. With the exception of W-based materials in basic electrolyte, ratios of the areal specific capacitances (nitrides/carbides, i.e. VN/VC) in both aqueous electrolytes are significantly greater than 1. The lower performance observed for carbides is due to excess carbon deposited on the materials during synthesis, as corroborated by results from Auger electron spectroscopy (see chapter two). Upon application of potential, electrolytes active ions interact more frequently with the carbon than the carbide. Such an interaction leads to electrostatic double-layer storage.

Interestingly, the nitride of V exhibited the highest areal specific capacitances. It is likely that V metal was subject to redox reactions on application of potential; the VN material may change oxidation state more rapidly than the other metals [11,12]. However, due to excess carbon on the surface, the carbide form, VC, showed low areal specific capacitance and no pseudocapacitance. When pretreated with H_2 gas to remove

excess carbon, VC exhibited pseudocapacitance, and possessed higher areal specific capacitance, and wider voltage window than the non-pretreated VC (standard) as shown in Figure 3.14. We noticed that α-Mo_2C and β-WC_{1-x} performed as good as γ-Mo_2N and β-W_2N, respectively, due to the absence of undesirable carbon on their surfaces, a consequence of their synthesis procedures as compared to the other carbides (see Table 2.2 in chapter two). The synthesis procedures for α-Mo_2C and β-WC_{1-x} are similar to those for γ-Mo_2N and β-W_2N.

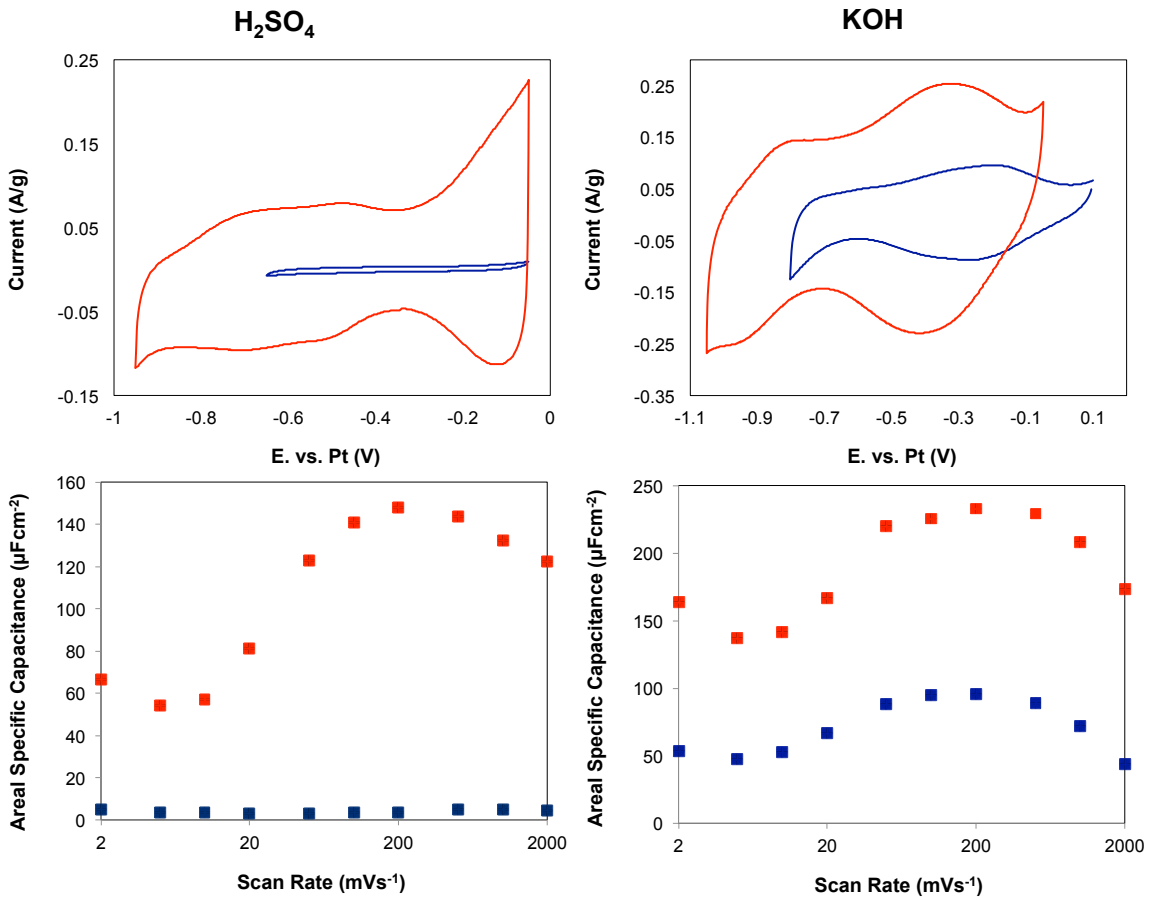

Figure 3.14: Cyclic voltammograms and areal specific capacitances for H_2-pretreated VC (red) and non-pretreated VC (blue). Voltammograms collected at 20 mVs^{-1} showing 2nd cycle.

The following section aims to quantify the pseudocapacitance contribution to the charge storage for the carbides and nitrides. As discussed in chapter one, pseudocapacitance is capacitance that derives from reversible surface redox reactions, electrosorption and intercalation, involving electron transfer between the electrode and the electrolyte, and is experimentally observed via redox couples in the voltammogram, the logarithmic behavior of capacitance with scan rate, and the magnitude of the areal specific capacitance (>> 50 μFcm^{-2}).

3.3.4. Pseudocapacitance and Double-Layer Capacitance Contributions

EIS was used to quantitatively determine the extent of pseudocapacitance in selected materials. Figure 3.15 shows the phase angle as function of frequency (Bode plot) for γ-Mo_2N, VN, TiN, (α+β)-Mo_2C and WC_{1-x} in aqueous electrolytes at selected potentials within the stable potential window. These materials were selected because of their high areal specific capacitances as shown in Figures 3.12 and 3.13. The total capacitive behavior of the system is obtained at low frequencies, where the phase angle approaches a maximum value [13,14]. At that frequency, the derivative of the phase angle with respect to frequency goes to zero as shown in the equation below:

$$\frac{d\emptyset}{df} = 0, \qquad when\ f = f_{max} \qquad (2)$$

where Φ and f_{max} are the phase angle and maximum frequency, respectively. At a potential where only double-layer or electrostatic charge forms, the derivative of the phase angle goes to zero faster than at a potential where pseudocapacitive storage also occurs as shown in Figure 3.16. This is expected, given that the two charge-storage mechanisms have different time constants. The double layer time constant is faster than the pseudocapacitve time constant. In the case of γ-Mo_2N (Figure 3.16g), the maximum

phase angle of both the pseudocapacitive storage and double-layer storage are similar. We believed this is due to the fast surface adsorption rate of hydrogen on γ-Mo_2N, hence making isolation of the double-layer charge difficult.

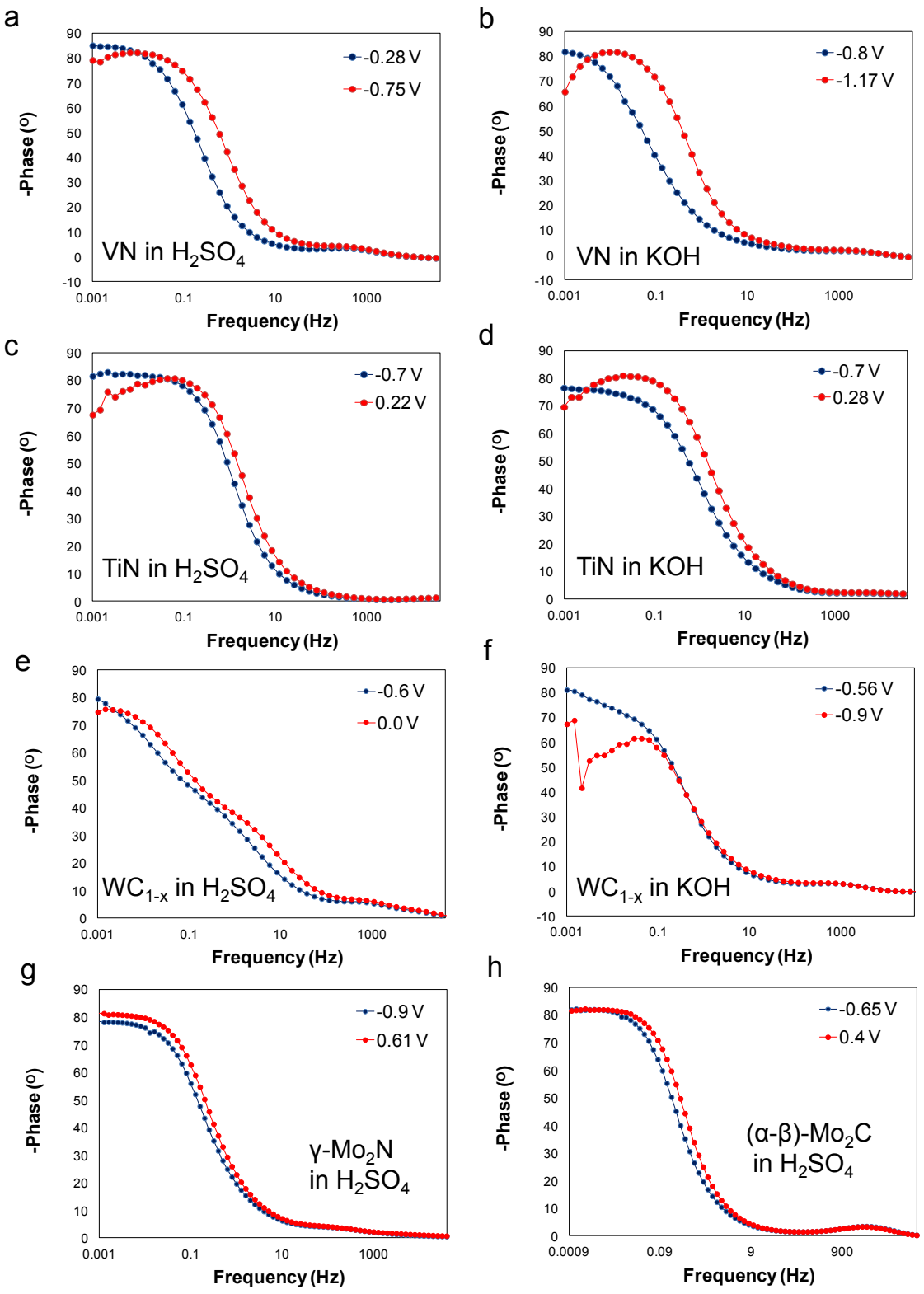

Figure 3.15: Plot of Bode phase angle as function of frequency at selected potential for carbides and nitrides in aqueous electrolytes, blue curve represents pseudocapacitance behavior and red curve represents double-layer capacitance behavior.

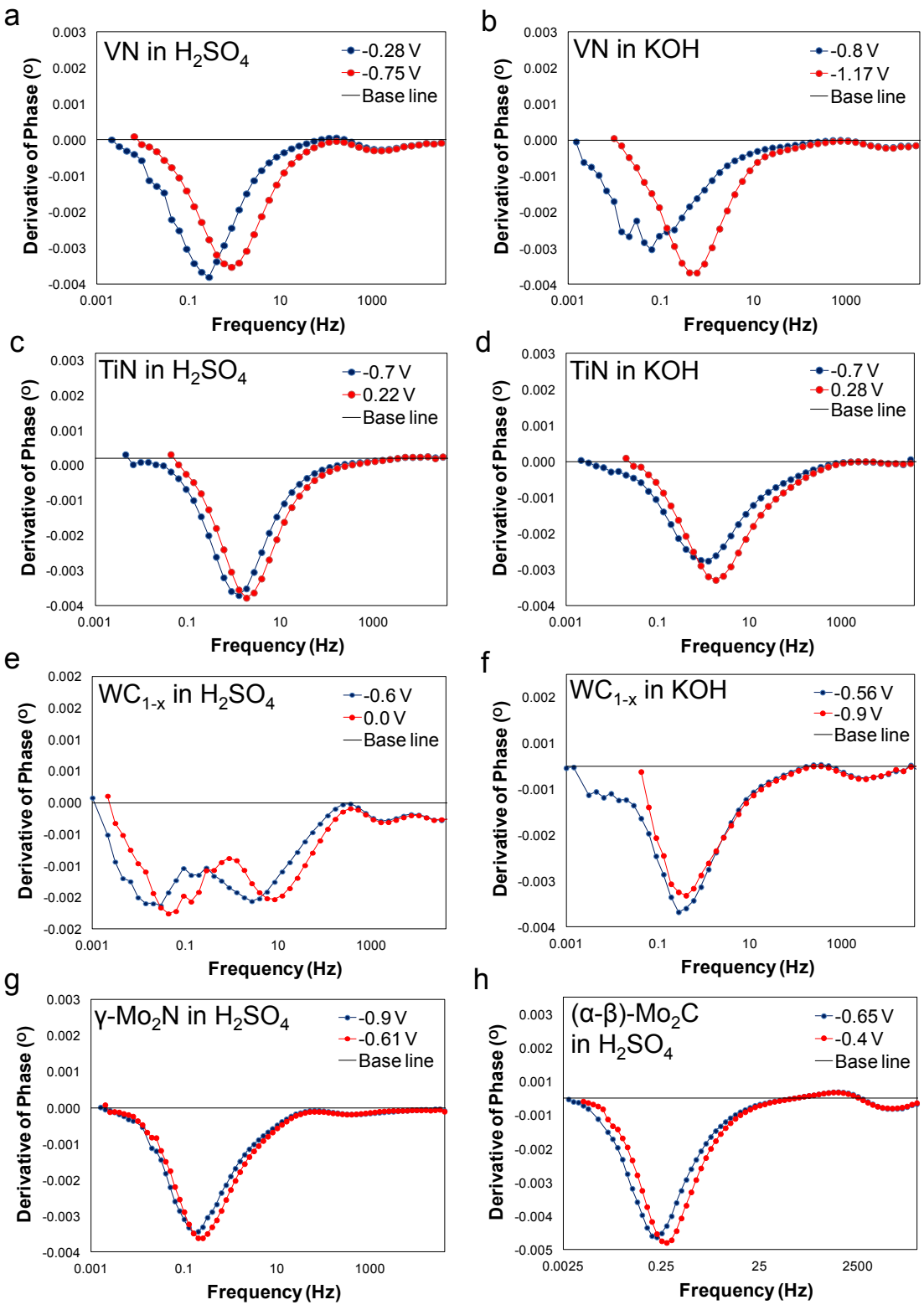

Figure 3.16: Derivative of Bode phase angle as function of frequency at selected potentials for carbides and nitrides in aqueous electrolytes, blue curve represents pseudocapacitance behavior and red curve represents double-layer capacitance behavior.

The capacitance at each selected potential was calculated using the following equation [15,16]:

$$C = \frac{-1}{2\pi f_{max} Z''_{max}} \qquad (3)$$

Where Z''_{max} is the imaginary impedance at the maximum frequency f_{max}. Table 3.2 lists the Z''_{max}, f_{max} and capacitance values for all the selected carbides and nitrides in aqueous electrolytes at selected potentials within the stable voltage window. A plot of capacitance as a function of potential allows for distinction between double-layer charge and pseudocapacitive charge, which generally varies with applied voltage (as indicated in chapter two). The total capacitive behavior of the system was obtained at a maximum phase angle, near -90°, where the system behaves like an ideal supercapacitor [13,14]. Figure 3.17 shows the capacitances obtained from EIS (red markers) plotted on top of the cyclic voltammograms for all the materials at selected potentials within the stable voltage window. For all the materials, the capacitance goes to a minimum value in the double-layer region (the flat region on the CV) indicating absence of faradaic electron transfer or pseudocapacitance. The double-layer capacitance of each material in aqueous electrolytes is highlighted in red in Table 3.2. The capacitance increases at the potentials where redox peaks occurred, indicating presence of pseudocapacitive charge storage or electron transfer on the surface of the carbide or nitride. The γ-Mo_2N and (α+β)-Mo_2C (Figures 3.17 g and h, respectively) materials in acidic electrolyte show low areal specific capacitances with applied potentials across the entire voltage window. A plausible explanation for this is the lack of full accessibility of the pores by the electrolyte ions. These high surface-area materials are composed of mainly micropores. It takes a much longer time for electrolyte ions to diffuse into micropores than into mesopores or

macropores. The Ti-based systems exhibit pseudocapacitance at more negative potentials as indicated by the increase over the double-layer capacitance. At more positive potentials, the capacitance goes to a minimum value, again suggesting the absence of pseudocapacitive charge storage. The lack of pronounced redox peaks in the voltammograms of WC_{1-x} (in H_2SO_4), (α+β)-Mo_2C (in H_2SO_4) and TiN (in KOH), suggest fast ion adsorption (similar to RuO_2 and MnO_2 systems) [3]. The V and Mo-based systems show pronounced redox couples. The peak locations and separation are in good agreement with those reported previously [17-24].

The extent of pseudocapacitance in the selected carbides and nitrides was estimated by subtracting the electrostatic or double-layer capacitance from the total capacitance. It is worth mentioning that the double-layer capacitance obtained in this study using EIS was similar to that from the CV method. Table 3.3 lists the value of and the percent contribution of pseudocapacitance for each of the materials in aqueous electrolytes. The extent of the pseudocapacitive charge-storage contribution ranges from 63% for TiN to 87% for VN in acidic electrolyte. This indicates that pseudocapacitance is the dominant charge-storage mechanism in these carbides and nitrides. This is expected given that these materials are highly electroactive and can go through successive oxidation state changes during electrochemical cycling [11,12]. In fact, this is the primary reason why the areal specific capacitances shown in Figures 3.12 and 3.13 are much higher than that of the commercialized material, activated carbon (11 μFcm^{-2}) [25,26]. Interestingly, the pseudocapacitance contributions in H_2SO_4 and KOH electrolytes are similar, in particular for WC_{1-x} and VN, suggesting that the number of electron transfers

implicated in the charge-storage mechanisms in these electrolytes might be similar. This is further discussed in the next chapter.

Table 3.2: Capacitance, Z''_{max} and f_{max} values for all carbides and nitrides in aqueous electrolytes at selected potentials within the stable voltage window.

VN (H_2SO_4)

Potential (V)	Z''_{max}	f_{max}	Capacitance (F/g)	Specific capacitance (μFcm^{-2})
-1.10	45.735	0.02947	41.00	102.49
-0.80	234.69	0.00954	24.68	61.70
-0.75	242.19	0.0095411	23.91	59.78
-0.65	154.31	0.013895	25.77	64.43
-0.45	212.48	0.0044984	57.81	144.52
-0.35	544.86	0.0014563	69.64	174.09
-0.28	679.12	0.001	81.36	203.41

VN (KOH)

Potential (V)	Z''_{max}	f_{max}	Capacitance (F/g)	Specific capacitance (μFcm^{-2})
-1.20	117.75	0.013895	33.77	84.43
-1.17	118.67	0.013895	33.51	83.77
-1.00	869.75	0.001	63.53	158.82
-0.85	308.33	0.001	179.21	448.02
-0.63	66.869	0.0065512	126.13	315.33
-0.40	647.2	0.001	85.38	213.44
-0.05	214.84	0.0044984	57.17	142.93

TiN (H_2SO_4)

Potential (V)	Z''_{max}	f_{max}	Capacitance (F/g)	Specific capacitance (μFcm^{-2})
-0.58	71.954	0.02947	39.09	217.15
-0.50	1307.3	0.00212	29.91	166.14
-0.35	459.4	0.0065512	27.54	153.00
-0.21	400.33	0.009541	21.70	120.55
0.04	101.59	0.042918	19.01	105.61
0.10	119.66	0.042918	16.14	89.66
0.23	134.15	0.042918	14.40	79.98

TiN (KOH)

Potential (V)	Z''_{max}	f_{max}	Capacitance (F/g)	Specific capacitance (μFcm^{-2})
-0.70	2790	0.001	24.59	136.58
-0.60	2450.3	0.001456	19.23	106.81
-0.54	2663.6	0.001456	17.69	98.26

-0.35	2402	0.00212	13.47	74.83
0.13	628	0.013895	7.86	43.67
0.20	686.32	0.013895	7.19	39.96
0.29	506.77	0.020236	6.69	37.16

WC_{1-x} (H_2SO_4)

Potential (V)	Z''_{max}	f_{max}	Capacitance (F/g)	Specific capacitance (μFcm^{-2})
-0.70	397.76	0.001	90.93	139.89
-0.60	424.5	0.001	85.20	131.08
-0.50	580.28	0.001	62.33	95.89
-0.40	605.53	0.001	59.73	91.89
-0.30	629.68	0.001	57.44	88.36
-0.10	808.1	0.001	44.76	68.85
0.09	26.291	0.042919	32.05	49.31

WC_{1-x} (KOH)

Potential (V)	Z''_{max}	f_{max}	Capacitance (F/g)	Specific capacitance (μFcm^{-2})
-0.90	40.222	0.042918	46.09	70.91
-0.86	718.28	0.0014563	76.07	117.02
-0.72	682.46	0.0014563	80.06	123.17
-0.56	657.25	0.0014563	83.13	127.89
-0.32	335.06	0.0030888	76.88	118.28
-0.21	245.29	0.0044984	72.11	110.94
-0.11	85.846	0.013895	66.70	102.62

γ-Mo_2N (H_2SO_4)

Potential (V)	Z''_{max}	f_{max}	Capacitance (F/g)	Specific capacitance (μFcm^{-2})
-0.95	40.833	0.015849	61.47	58.55
-0.90	373.85	0.0015849	67.14	63.95
-0.78	336.54	0.0019953	59.25	56.42
-0.61	433.62	0.0019953	45.98	43.79
-0.45	352.5	0.0019953	56.56	53.87
-0.38	163.92	0.0039811	60.96	58.06
-0.15	189.92	0.0031623	66.24	63.09

(α+β)-Mo_2C (H_2SO_4)

Potential (V)	Z''_{max}	f_{max}	Capacitance (F/g)	Specific capacitance (μFcm^{-2})
-0.80	60.983	0.012599	117.68	117.68
-0.65	235.4	0.0031623	121.46	121.46
-0.40	211.19	0.0050119	85.42	85.42
-0.30	102.79	0.01	87.96	87.96
-0.20	55.73	0.015849	102.37	102.37

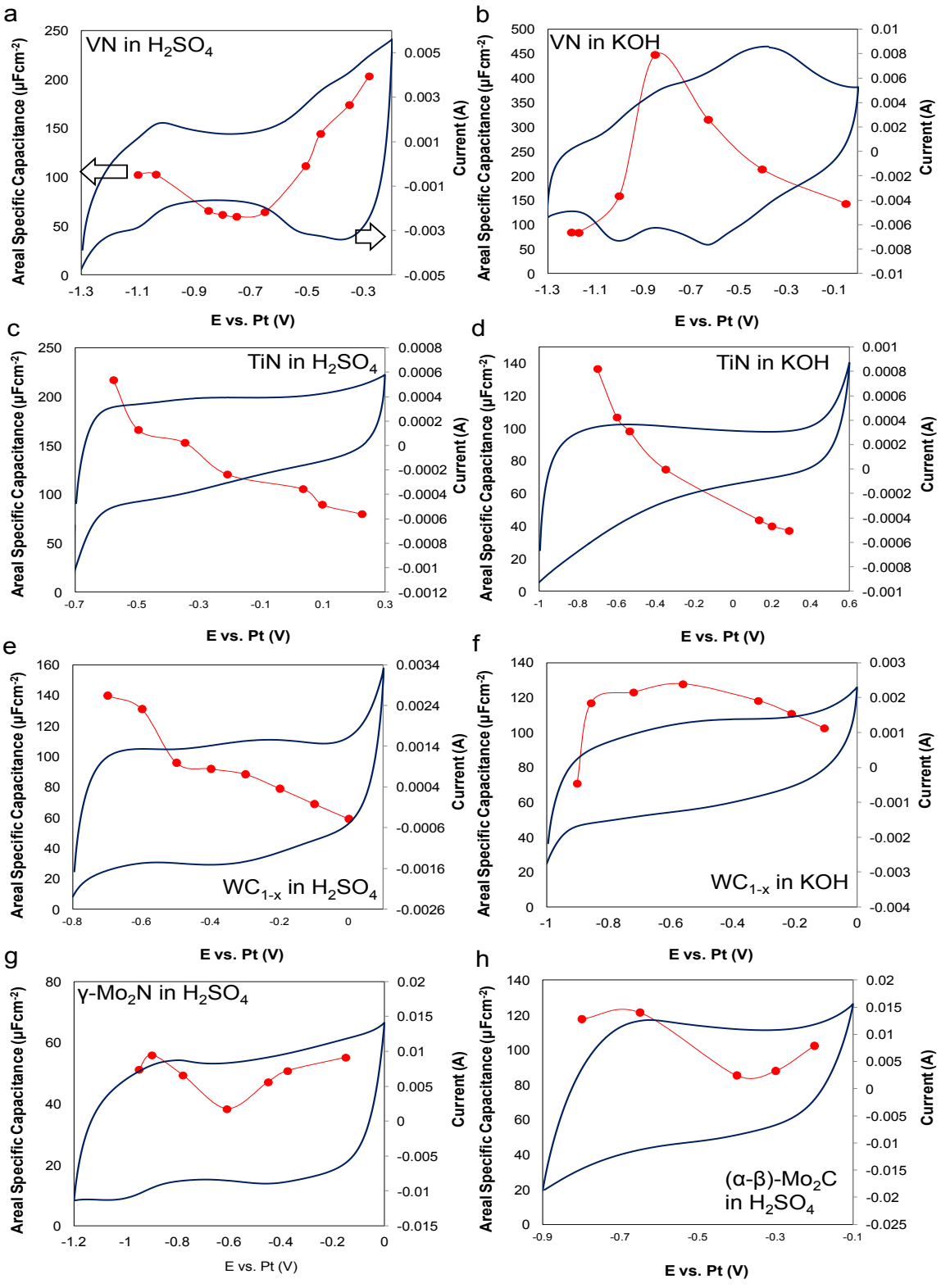

Figure 3.17: Plot of capacitance (red dot circle, from EIS) and cyclic voltammograms (collected at10 mVs^{-1}) of carbides and nitrides in aqueous electrolytes, the scan shown is the 5^{th}.

Table 3.3: Extent of pseudocapacitance in carbides and nitrides in aqueous electrolytes.

Material	Pseudocapacitance ($\mu F\ cm^{-2}$)		Extent of Pseudocapacitance (%)	
	0.1M H_2SO_4	0.1M KOH	0.1M H_2SO_4	0.1M KOH
WC_{1-X}	142	281	74	80
TiN	137	191	63	84
VN	390	469	87	85
γ-Mo_2N	183	-	81	-
(α+β)-Mo_2C	165	-	66	-

3.4. Conclusion

A series of nanostructured Ti, V, Nb, Mo, and W interstitial compound carbides and nitrides were synthesized using a temperature-programmed reaction method. The materials were found to be electrochemically stable in both aqueous H_2SO_4 and KOH electrolytes. Areal specific capacitances for all materials except for NbC and VC in H_2SO_4 electrolyte exceeded double layer charging, varied logarithmically with scan rate, and reached a maximum value at a lower scan rate (2 mVs^{-1}). These indicate the contribution to charge storage from a pseudocapacitive storage mechanism.

The percent contribution of pseudocapacitance was evaluated using electrochemical impedance spectroscopy and cyclic voltammetry. The pseudocapacitive charge-storage mechanism was found to be the most dominant mechanism in all carbides and nitrides. The extent of the pseudocapacitance contribution ranges from 63% for TiN to 87% for VN in H_2SO_4 electrolyte. This pseudocapacitance is the key component in the full utilization of carbide and nitride-based supercapacitors.

Correlation between crystal structure, composition, and charge storage properties was also investigated. The fcc-structured Mo_2C exhibited higher areal specific capacitance in KOH electrolyte due to their larger pore size, while hcp-based structured

Mo_2C materials possessed higher areal specific capacitance in H_2SO_4 electrolyte. The nitrides had higher areal specific capacitance than the carbides. The relatively lower performance observed for the carbides is due to the presence of excess carbon on their surfaces, which inhibits pseudocapacitive charge storage. In terms of metal, V exhibited higher areal specific capacitance in its nitride form, while in their carbide form, Mo and W metals showed improved charge storage capacity due to the absence of excess surface carbon, a consequence of their synthesis procedures. Ultimately, these findings can serve as useful correlation and prediction tools for the design of higher-energy-density carbide and nitride-based supercapacitor electrode materials.

3.5. References

1. P. Pande, A. Deb, A. S. Sleightholme, A. Djire, P. Rasmussen, J. Penner-Hahn, L. T. Thompson, J. Power Sources, 289 (2015) 154-159.
2. P. Simon, Y. Gogotsi, Nature Materials, 7 (2008) 845.
3. B. E. Conway, Electrochemical Supercapacitors, Kluwer Academic/ Plenum Publishers, (1999).
4. B. E. Conway, J. Electrochem. Soc., 6 (1991) 138.
5. S. C. Pang, B. H. Wee, S. F. Chin, International J. Electrochemistry, 10 (2011) 4061.
6. E. Beaudrouet, A. Le Gal La Salle, D. Guyomard, Electrochimica Acta, 54 (2009) 1240-1248.
7. Q. Huang, X. Wang, J. Li, Electrochimica Acta, 52 (2006) 1758-1762.
8. J. P. Xheng and T. R. Jow, J. Electrochem. Soc., 1 (1995) 142.
9. L. He, Y. B. Melnichenko, N. C. Gallego, C. I. Contescu, J. Guo, and J. Bahadur, Carbon, 80 (2014) 82-90.
10. W. C. Conner, J. P. Fraissard, Fluid Transport in Nanoporous Materials: Proceedings of the NATO Advanced, Springer (2006).
11. D. W. Choi, G. E. Blomgren, P. N. Kumta, Adv. Mater., 18 (2006) 1178.
12. L. Soriano, M. Abbate, H. Pen, P. Pierto, J. M. Sanz, Solid State Comm. 102, 4, (1997) 291-296.
13. E. Frackowiak, F. Beguin, Carbon, 39 (2001) 937-950.
14. A. Portet, G. Yushin, Y. Gogotsi, Carbon, 45 (2007) 2511-2518.

15. L. Andrzej, Electrochemical Impedance Spectroscopy and its Application, Kluwer Academic/Plenum Publisher, NY, (1999).
16. M. E. Orazem, Electrochemical Impedance Spectroscopy, Wiley Publisher, NY, (2008).
17. A. Djire, O. Ajenifujah, A. S. Sleigtholme, P. Rasmussen, L. T. Thompson, J. Power Sources, 47 (2015) 159-166.
18. P. Pande, P. Rasmussen, L. T. Thompson, J. Power Sources, 207 (2012) 212-215.
19. T. C. Liu, W. G. Pell, B. E. Conway, J. Electrochem. Soc., 145 (6) (1998) 1882.
20. A. M. Glushenkov, D. Hulicova, D. Llewellyn, G. Q. Liu, Y. Chen, Chem. Mater., 22 (2010) 914.
21. O. Kartachova, A. M. Glushenkov, Y. Chen, H. Zhang, X. Dai, Y. Chen, J. Power Sources, 220 (2012) 298-305.
22. O. Kartachova, A. M. Glushenkov, Y. Chen, H. Zhang, Y. Chen, J. Mater. Chem. A, 1 (2013) 7889.
23. R. L. Porto, S. Bouhtiyya, J. F. Pierson, A. Morel, F. Caon, P. Boulet, T. Brousse, Electrochimica Acta, 141 (2014) 203-211.
24. O. Kartachova, Y. Chen, R. Jones, H. Zhang, Y. Chen, A. M. Glushenkov, J. Mater. Chem. A, 2 (2014) 12940.
25. M. Galinski, K. Babel, K. Jurewicz, J. Power Sources, 228 (2013) 83-88.
26. A. Lewandowski, P. Jakobczyk, M Galinski, Electrochemical Acta, 86 (2012) 225-231.

Chapter 4

Charge Storage Mechanism

4.1. Introduction

Among the carbides and nitrides, VN (in aqueous KOH electrolyte) and Mo_2N (in aqueous H_2SO_4 electrolyte) are the most promising systems for commercial applications. The full exploitation of VN and Mo_2N materials in a supercapacitor requires a detailed understanding of their charge storage mechanisms. This chapter characterizes the charge-storage mechanisms for VN and Mo_2N in aqueous KOH and H_2SO_4 electrolytes, respectively, using *in-situ* small angle neutron scattering (SANS) and *in-situ* x-ray absorption spectroscopy (XAS) combined with physical and electrochemical characterization techniques. The average oxidation state of the metals (V and Mo) and changes in the bulk structure were determined while the materials were electrochemically cycled within their operating potential windows (~1.2 V for both). The amount of inserted hydroxide ions (in VN) and hydrogen ions (in Mo_2N) per mole of electron transferred during charge storage was determined. The location and distribution of inserted hydroxide and hydrogen ions in pores were also determined. Combining results from *in-situ* experimental techniques and electrochemical characterization techniques, the charge-storage mechanisms of the materials in aqueous electrolytes were established. Full utilization of the materials yields charge storage capacities in excess of 1300 F g^{-1} (3550

μF cm^{-2}) for VN and 1500 F g^{-1} (1040 μF cm^{-2}) for Mo_2N, in 1.2 V operating voltage windows.

4.2. Experimental Methods

4.2.1. *In-Situ* X-Ray Absorption Spectroscopy (XAS)

In order to characterize the changes in the material during charge storage, we applied spectroscopic techniques in conjunction with electrochemical measurements. *In-situ* XAS allows monitoring of the detailed local atomic coordination and chemical oxidation state of a specific element of interest [1].

During XAS measurement, the x-ray energy is scanned through the binding energy of the core electron shell of an element, which leads to a substantial increase in absorption, giving rise to an absorption edge. The energy at which x-rays are absorbed by an atom is element specific and is called the edge energy [1]. Core shells (K, L or M shell) for an element have discrete binding/edge energies giving rise to K, L or M x-ray absorption edges [1]. The XAS spectra are typically divided into two regions: (i) x-ray absorption near-edge spectra (XANES) and (ii) extended x-ray absorption fine structure (EXAFS). The XANES region is about 20 eV above and below the absorption edge, while the EXAFS region can extend as much as 1000 eV beyond the absorption edge [1].

Generally, XAS can be carried out in transmission and/or fluorescence mode. In transmission mode, ionization chambers are placed in front of and behind the sample. Incident and the transmitted x-ray flux are measured to account for the absorption. In fluorescence mode, the absorption of x-ray results in photoelectron emission, which leaves the atom in an excited state. Fluorescent x-rays are emitted to repopulate the core-

hole. The fluorescent x-rays interact with the core, proportional to the x-ray absorption coefficient of the material [1].

4.2.1.1. Electrochemical System

The *in-situ* XAS measurements, carried out in a transmission mode, were performed on the VN and Mo_2N systems using a custom-made electrochemical cell [2]. In this chapter, we will focus on the XAS analysis for VN. Details regarding the XAS analysis for Mo_2N are reported elsewhere [3]. Pt wire and Pt black (Alfa Aesar) coated on Ti foil (99.7%, Aldrich) were used as the quasi-reference electrode and counter electrode, respectively. In efforts to minimize x-ray absorbance from the electrolyte ions, the measurements were performed in an aqueous solution of 0.1 mol dm^{-3} LiOH instead of KOH due to the low x-ray absorption energy of Li (54 eV) compared to that of K (3608.4 eV). Celgard 3501 was used as the separator. The electrolyte solution was deaerated with N_2 (99.998% with an oxygen trap) for at least 30 min before addition into the cell. After the electrolyte solution was added, the cell was sealed.

4.2.1.2. Experimental Method

The XAS measurements were performed in transmission mode at the bending magnet beam line station D of the DND-CAT (Sector 5) at the Advanced Photon Source (APS) at Argonne National Laboratory. A water cooled Si(111) double-crystal monochromator was used for energy selection, and incident and transmitted x-ray intensities were measured using Ar filled ion chambers at 1 atm pressure with an applied potential of 300 V. Harmonic rejection at the station D, was achieved by detuning the beam to 65% of the maximum value of the monochromator rocking curve. The beam size was defined as 1 x 3 mm^2 using slits and had an incident photon flux of ~10^{10} photons s^{-1}.

Before adding the electrolyte solution, XAS measurements were made on the "as-is" sample. The deaerated electrolyte solution was then added and the cell was sealed. Cyclic voltammograms were acquired using a CH-instruments CH-600D potentiostat. The scan rate was 5 mV s^{-1} and the stable-operating potential range was determined vs. the Pt wire quasi-reference electrode. To avoid H_2 gas evolution, the potential window was restricted to 1.1 V. The potential window was divided into discrete potential steps (listed in Table 4.1) and *in-situ* XAS measurements were performed at these potentials. The samples were allowed to equilibrate for at least 1000 s at each potential prior to collecting the XAS spectra. Three scans (5315 to 6200 eV using 5 eV steps in the pre-edge region, 0.5 eV steps in the near-edge region and 0.05 $Å^{-1}$ steps in the EXAFS region) were taken at each applied potential and averaged for further analysis. The data were integrated for 1 s in the pre-edge, 1.5 s in the near edge region and 1.5 to 25 s in the EXAFS region for a total scan time of about ~2300 s. The energy was calibrated by simultaneously collecting spectra for a V foil, with the first inflection point of the V foil defined as 5465 eV. The raw data were converted into EXAFS spectra using ATHENA [4], with E_0 defined as 5465 eV and a cubic spline used to remove the EXAFS background. The resulting $\chi(k)$ function was weighted with k^3 to account for the damping of oscillations with increasing k. The radial structure functions presented here were obtained by Fourier transformation of $k^3\,\chi(k)$ using a k range of 1.5-13 $Å^{-1}$.

4.2.1.3. Data Analysis

Data were fitted using IFFEFIT [4] with *ab initio* amplitude and phase functions calculated using FEFF9.0 [5], and using the crystallographic coordinates for VN. The backgrounds were subtracted by extrapolating a Victoreen-type function from the pre-

edge region, and EXAFS oscillations χ(k) were extracted using cubic spline baseline functions. The radial structure functions presented here were obtained by Fourier transformation of $k^3\chi(k)$ using a k-range of 1.5−13.0 $Å^{-1}$. The first peak ~2 Å in the FT is attributed to the V-N interactions, while the second peak ~ 2.9 Å is due to the V-V interactions. To understand the structural changes during the electrochemical cycling, for each potential step, data were collected two times once from OCP to -0.9 V and then back to -0.1 V, the results of the fits are summarized in Table 4.1.

Table 4.1: EXAFS fit results; Forward (F), Reverse (R).

Potential (V)	V-N	
	R (Å)	σ^2
OCP	2.069	0.0066
-0.9(F)	2.072	0.0069
-0.9(R)	2.072	0.0071
-0.7(F)	2.071	0.0071
-0.7(R)	2.071	0.0069
-0.5(F)	2.069	0.0072
-0.5(R)	2.068	0.0070
-0.3(F)	2.066	0.0071
-0.3(R)	2.065	0.0070
-0.1(F)	2.064	0.0071
-0.1(R)	2.064	0.0072
Crystallographic	R (Å)	
	2.066	

4.2.2. *In-Situ* Small Angle Neutron Scattering (SANS)

SANS technique uses elastic neutron scattering at small scattering angles to investigate structures at a mesoscopic scale of about 1 to 100 nm. SANS is in many respects very similar to small angle x-ray scattering (SAXS): both techniques are jointly referred to as small angle scattering (SAS). Advantages of SANS over SAXS include its sensitivity to light elements, the possibility of isotope labeling, and the strong scattering by magnetic moments.

During SANS experiments, a beam of neutrons is directed at a sample, which can be an aqueous solution, a solid, a powder, or a crystal. The neutrons are elastically scattered by nuclear interaction with the nuclei or interaction with magnetic momentum of unpaired electrons. In SAXS, photons interact with the electron cloud (so larger elements show a larger effect), but in neutron scattering, neutrons interact with nuclei. This interaction depends on the isotope; some light elements like deuterium (D) show similar scattering cross sections as heavy elements like lead (Pb).

SANS is characterized by coherent and incoherent contributions to scattering. Coherent scattering depends on q (scattering vector) and is therefore the part that contains information about scattering structures, and is used to analyze the interaction of adsorbed ions with the pore wall. Incoherent scattering is featureless (q independent) and contains information about the material scattering density, and is used to monitor the density of the adsorbed ions into the material.

4.2.2.1. Sample Preparation

Prior to the *in-situ* SANS experiment, VN and Mo_2N working electrodes were made by welding together 24 electrodes of each material (approximately 1 g of active material) using Ti wire (0.1 cm by 5 cm). The electrodes were made by slurry-coating the materials onto Ti foil substrates (99.97%, Alfa Aesar, 0.032 mm thickness, US). The approximate coated area on both sides of the Ti foil was 0.8 cm wide by 1.5 cm long and 300 μm thick. A Pt wire (1 mm diameter) and activated carbon (Kynol activated carbon fabric ACC-507-15, sp. S. A. 1500 $m^2 g^{-1}$) were used as the quasi-reference and counter electrodes, respectively. A quartz cell (1 cm x 2 cm wide and 5 cm long) from Hellma Company was used. The cell was air tight, sealed using a PTFE lid and vacuum grease

seal. A PTFE sample holder was used and the cell was mounted in an aluminum block. A simplified schematic of the *in-situ* experimental setup is shown in Figure 4.1.

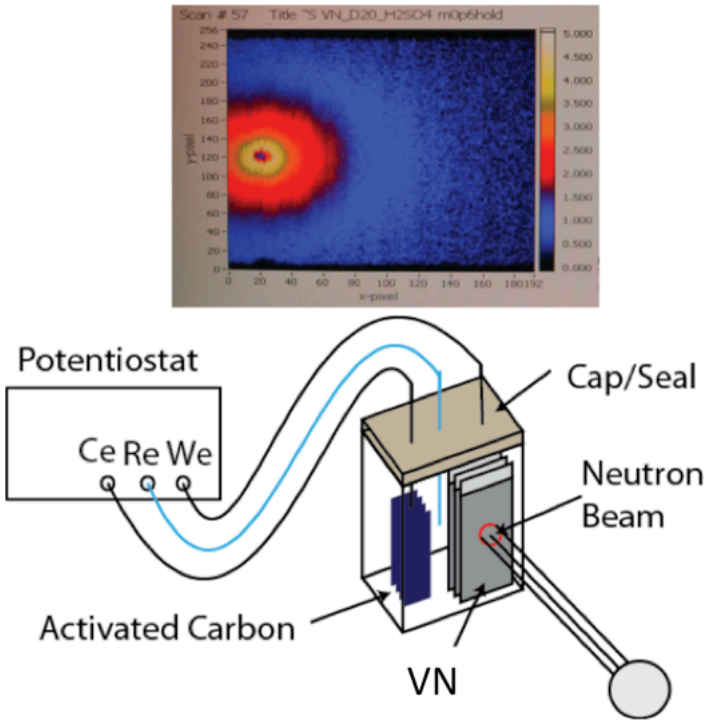

Figure 4.1: Schematic of the in-situ SANS experimental set up, showing the electrochemical cell with electrodes and electrolyte, potentiostat, and neutron beam. A typical 2D plot of the data is shown above.

4.2.2.2. Experimental Method

The SANS technique was used to quantify the amount and the location of the electrochemically active ions into the VN and Mo_2N materials during electrochemical charge storage. VN was characterized in KOD electrolyte and Mo_2N in H_2SO_4. Approximately 10 ml of 0.1 mol dm^{-3} electrolytic solution was used for each measurement. We replaced KOH with KOD due to the small scattering length density (SLD) difference between OD and VN. The SLD is a measure of the strength of the interaction of a neutron wave with a given nucleus. Typically, the smaller the difference

in SLD between two substances, the greater the scattering contrast. The small SLD difference between OD ($6.237x10^{-13}$ cm) and VN ($5.068x10^{-13}$ cm) enhances the scattering contrast between the porous solid and adsorbed active species (deuteroxide ions). Similarly, due to the small SLD difference between D_2O and the materials (VN and Mo_2N), D_2O was used as solvent for both materials instead of H_2O. The choice of D_2O minimizes significantly the incoherent scattering contribution from the solvent. The SLD of D_2O is $6.335x10^{-13}$ cm, that of Mo_2N is $6.133x10^{-13}$ cm, and $-0.558x10^{-13}$ cm for H_2O.

SANS experiments were conducted at Oak Ridge National Laboratory (ORNL), using a General Purpose SANS instrument with a neutron wavelength of $\lambda = 4.75$ Å and a wavelength spread ($\Delta\lambda/\lambda$) of 0.13 [6]. Two sample-to-detector distances, 12 m and 0.26 m, were used to cover a q range between 0.005 $Å^{-1}$ and 0.9 $Å^{-1}$, where q is the scattering vector. Average acquisition time for each scattering curve was approximately 30 min. The measurements were conducted at room temperature. Similar to the XAS experiment, before adding the electrolyte solution, SANS measurements were made on the dry sample. After addition of deaetered electrolyte into the sealed *in-situ* electrochemical cell, SANS measurements were performed on the wet electrode at an open circuit potential (OCP) or rest potential. Subsequently, cyclic voltammograms were acquired using a CH-instruments CH-600D potentiostat. The scan rate was 1 mV s^{-1} and the stable-operating potential range was determined vs. the Pt wire quasi-reference electrode. Similar to the XAS experiment, the potential windows were restricted to 1.1 V and 0.8 V for the VN and Mo_2N, respectively, in order to avoid H_2 gas evolution. The potential windows were divided into discrete potential steps (listed in Tables 4.2 and 4.3) and *in-situ* SANS measurements were performed at these potentials to monitor the changes in the

distribution of deuteroxide or hydrogen ions as a function of applied potentials and pore sizes. The samples were allowed to equilibrate for at least 30 min at each potential prior to collecting the SANS intensities.

4.2.2.3. Data Analysis

The raw data was corrected for the instrument background, detector efficiency, and transmission. The corrected data were azimuthally averaged to produce the 1D profile I(q) vs. q, where $q = 4\pi\sin\theta/\lambda$ and 2θ is the scattering angle. Data were placed on an absolute scale (cm^{-1}) through the use of calibrated standards (vitreous carbons) [7]. The total scattering intensity is given by:

$$I_q = I(q)coherent + I(q)incoherent \quad (1)$$

At very high q, incoherent scattering dominates and coherent scattering is negligible.

$$I_q = I(q)incoherent \quad (2)$$

or

$$I_q = A\frac{(1-T)}{4\pi} \quad (3)$$

where A is a pre-factor that is related to the incident neutron flux, the solid angle subtended by the detector and the illumination area on the sample and T is the transmission. The amount of deuteroxide or hydrogen (electrochemical reactants) insertion in the illuminated volume was determined by using the following equation:

$$T = e^{(-n\sigma d)} \quad (4)$$

where n denotes the number density of scatters (OD^- and H^+) in the illuminated sample area, which have an effective total scattering cross-section σ ($\sigma = \sigma_{incoherent}$ for OD^- and for H^+) and d is the thickness of the sample. Subsequently, the number of electrons

transferred was determined by dividing the charge at each potential (area under the current-time plot) by Faraday's constant.

From the coherent scattering, we determined the extent of interaction of ion (H^+ or OH^-) with the pore walls using Beaucage model. This model allows deconvolution of the coherent scattering intensities from pores of different sizes (mesopores and micropores). The empirical mathematical equation of the model is shown below [8,9]:

$$I(q) = Bkgd + \sum_{i=1}^{N} G_i \exp\left(-\frac{q^2 R_{g,i}^2}{3}\right) + \frac{B_i[\text{erf}(\frac{qR_{g,i}}{\sqrt{6}})]^{3P_i}}{q^{P_i}} \qquad (5)$$

This models the Guinier (low q) and Porod (high q) regions of the scattering intensity with a smooth transition between them, where, R_g is the radius of gyration, P is the Porod exponent, and G and B are the Guinier and Porod scaling factors, respectively. The interaction of the adsorbed ion with the pore walls (in mesopores and micropores) was determined using the following equation:

$$\rho_{p,V} = \left(\rho_{Mo_2N\ or\ VN} \pm (\rho_{D_2O} - \rho_{Mo_2N\ or\ VN})\sqrt{\frac{Q_{OCP}}{Q_V}}\right) \qquad (6)$$

where $\rho_{p,V}$ represents the SLD of adsorbed ion (H^+ or OH^-) in the pores (with electrolyte), ρ_{VN} or ρ_{Mo2N} are the SLD of dry VN and Mo_2N materials, respectively, and Q is the Porod Invariant, and is expressed as:

$$Q = \int_0^\infty q^2 I(q) dq = 2\pi^2(\rho_{VNor\ Mo_2N} - \rho_p)^2 \varphi_p(1 - \varphi_p) \qquad (7)$$

where φ_p is the volume fraction of the pore of interest. The SLD of adsorbed ion reflects the interaction of the ion (H^+ or OH^-) with the pore walls. Higher SLD means higher ion-

pore wall interaction. The extent of interaction of H^+ or OH^- with the pore walls caused by the applied potential is given by:

$$\rho_{H^+ or OH^-(V)} = \rho_{p,V} - \rho_{OCP} \qquad (8)$$

Integration of experimental data in Eq. (7) is inherently performed over a limited q range. For integration over the full q range, extrapolation at both ends was made based on Guinier and Porod laws, which was done using the NIST SANS data analysis package [10].

4.3. Results and Discussion

This section discusses the charge storage mechanisms. Key aspects include metal electronic structure, metal local structure, active cation or anion adsorption/desorption and location in pores. The results for VN and Mo_2N will be discussed in separate sections.

4.3.1. VN Charge Storage Mechanisms

4.3.1.1. Physical and Electrochemical Properties

X-ray diffraction patterns, pore sizes distribution, and scanning electron micrographs for the VN (face-centered cubic, fcc) material are reported in chapter two. The pore size distributions indicated the presence of micropores (< 2 nm) and mesopores (2-50 nm). The surface area was 38 $m^2 g^{-1}$.

Figure 4.2a shows cyclic voltammograms for VN in KOH and LiOH electrolytes in H_2O, and in KOD electrolyte in D_2O using a 0.1 mol dm^{-3} electrolytic solution. There is a slight shift of peak position due to changes in the pH of the electrolyte solutions; otherwise, as expected, the voltammograms are nearly identical. The voltammograms include evidence for several redox events in the stable voltage window (1.2 V). These

features are consistent with faradaic or pseudocapacitive charge storage mechanisms involving fast, near-surface redox reactions of the electrolyte ions with the electrode material (as discussed in chapter three) [11-15]. In all the electrolytic solutions, the capacitance increases logarithmically with decreasing scan rate (see Figure 4.2b), again consistent with pseudocapacitive charge storage mechanism [16]. The capacitance plateaued at the lowest scan rates (~2 mV s^{-1}) indicating the total capacitance of the material. Slightly higher capacitances were observed for the material in the H_2O-based electrolytes compared to the D_2O-based electrolytes, owing to the higher ionic conductivity and lower viscosity of the H_2O solvent, which facilitates the mobility of OH^- into and out of pores.

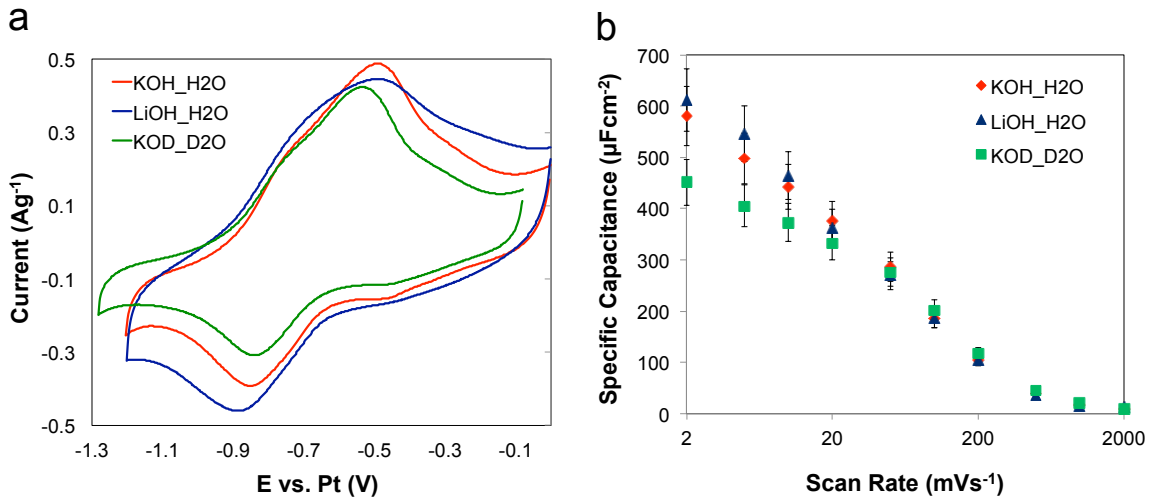

Figure 4.2: (a) Cyclic voltammetry and (b) capacitance behavior with scan rate for VN in in 0.1 mol dm^{-3} KOH/H_2O, $LiOH/H_2O$, and KOD/D_2O electrolytes, revealing pseudocapacitive redox activities and total capacitance, all data collected at room temperature.

4.3.1.2. V Electronic Structure

To determine the oxidation state of the V metal during pseudocapacitive charge storage, in-situ XAS analysis was performed on the VN material in 0.1 mol dm^{-3} LiOH in

H_2O solvent during operating condition. The XANES spectra were collected at selected potentials within the stable potential window as shown in Figure 4.3a. The spectra are characterized by a weak 1s-3d transition (the peak at ~5469 eV) followed by a rising edge. The weak 1s-3d transition is characteristic of a typical octahedral V environment. The lack of change in either the 1s-3d transition or the edge shape indicates that there was no significant change in the VN structure as the potential was changed. There was a shift in the edge energy to slightly lower values as the potential was decreased, which was consistent with the decrease in the average V oxidation state (see Figure 4.3b). The change in oxidation state was determined quantitatively using model compounds. The average oxidation state of the metal in the "as-prepared" VN was $V^{3.2+}$, and decreased to $V^{2.2+}$ as the applied potential was decreased (see Figure 4.3b). The average oxidation state of the electrode at different potentials was obtained in comparison with the edge energy of the model compounds (V_2O_5, V_2O_4, V_2O_3, VO) that were measured at the same time and are shown in the inset of Figure 4.3b. Both forward and reverse cycles showed a high degree of reproducibility and reversibility. Overall, the V metal in the VN material changed oxidation state by ~1 unit (e^- per V) as the potential was decreased from -0.1 V to -0.95 V, within the operating voltage window.

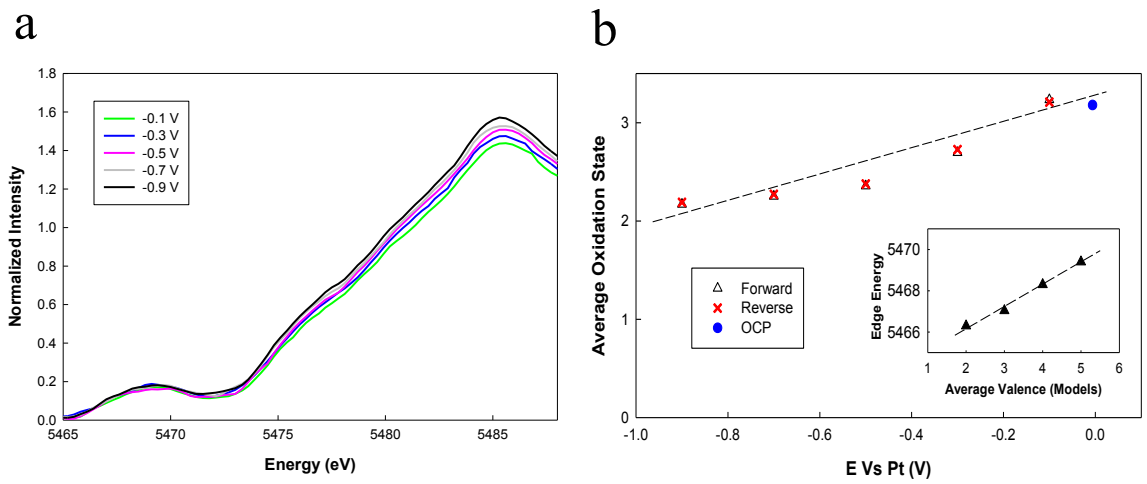

Figure 4.3: (a) *In-situ* XANES spectra for VN as a function of potential, data shown are for the forward cycle, identical spectra are seen during the reverse cycle; (b) Average oxidation state as a function of applied potential for VN in 0.1 mol dm^{-3} LiOH in H_2O. Oxidation state was calculated from the in situ XANES edge energy. The inset shows the change in the edge energy of the model compounds with respect to the average valance change. This information was used to obtain the average oxidation state change of the electrode at different potentials.

4.3.1.3. V Local Structure

The Fourier transforms of the EXAFS region for forward and reverse cycles are shown in Figures 4.4. The EXAFS spectrum for all selected potentials shows six main features, consistent with the known rock salt structure for VN. The peaks at ~2 Å and ~3 Å correspond to 6 V-N nearest neighbors and 12 V-V next nearest neighbors. There are two main outer shells at around ~3.5 Å and ~4.1 Å corresponding to V-N and V-V bond distances, and two other outer-shell peaks at ~4.6 Å and ~5 Å representing 24 N and 24 V. From Figure 4.4, it's interesting to note that there is significant change in amplitude of FT with respect to the change in potential around the peak at 4.7 Å. This can be attributed to the higher disorder in the system under higher potential. There are small variations in distance as a function of applied potential, but no significant change in the overall structure was observed. Consistent with the XANES results, the EXAFS spectra

for the forward and the reverse cycles showed outstanding reproducibility (Figure 4.4). The data were fit using the known rock salt structure with a minimum number of variable parameters. Table 4.1 lists the fitting parameters for the first shell V-N and V-V bond distances for selected potentials within the stable potential window. For the fits performed here the first shell was allowed to float (for R, σ^2, ΔE_0), while the rest of the paths were all linked. The fitted parameters show good agreement with the expected structure. The fitted distances are consistent with the crystallographic distances, with reasonable Debye-Waller factors. The EXAFS clearly shows that within the cycling window of -0.1 V and -0.9 V the nearest V-N and the V-V distances decreases by ~0.4% as the potential is increased from -0.9 V to -0.1 V. The same increase is observed on the reverse cycle, indicating reversibility of the change in distance (Table 4.1). Overall, the fitted distances for forward and reverse cycles are highly reproducible (±0.002 Å) and there are no significant changes in the bulk structure as a function of applied potential, indicating good electrochemical stability of the material in aqueous alkaline electrolytes.

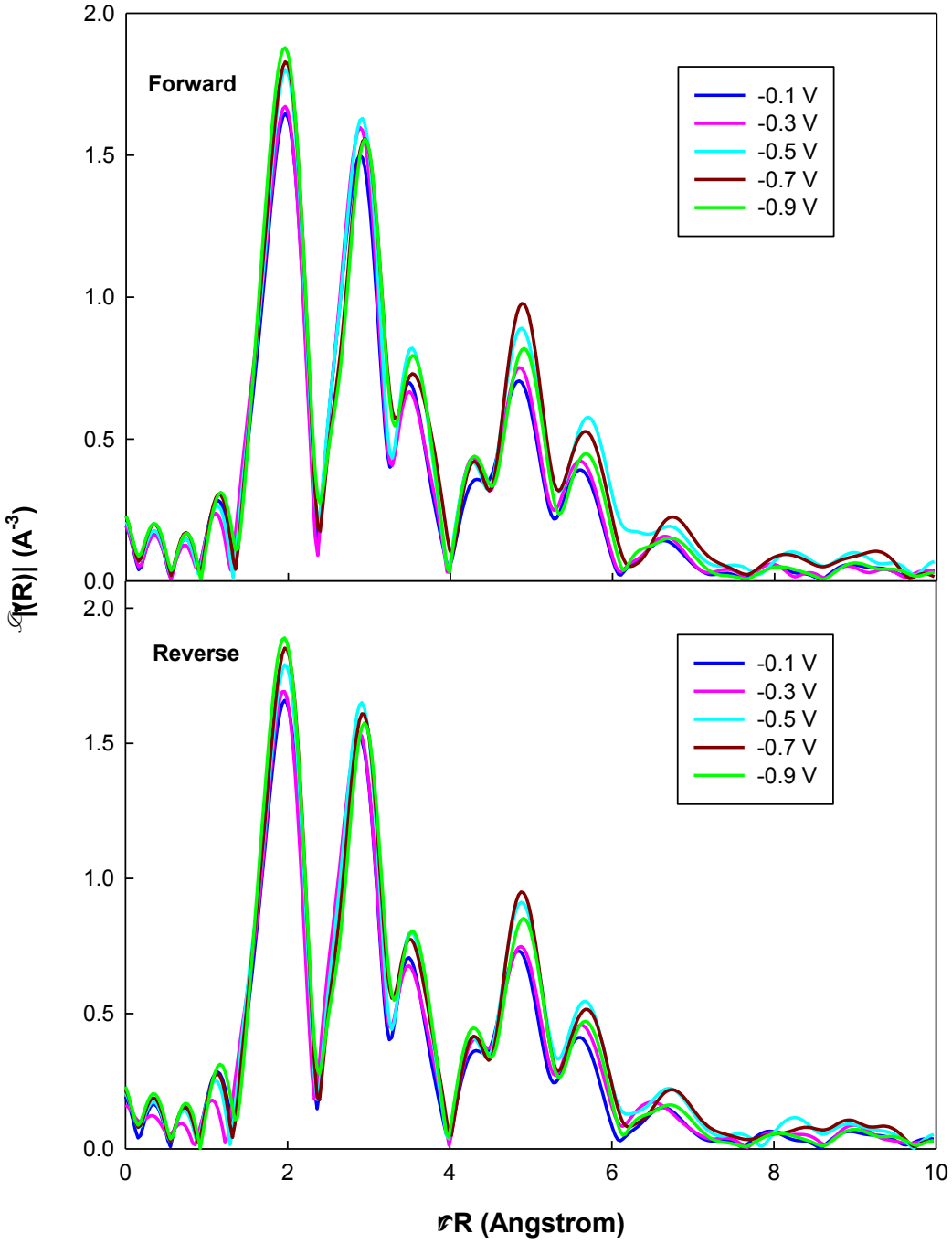

Figure 4.4: Fourier transforms of the in situ EXAFS data for VN as a function of applied potential during charge (top) and discharge (cycles).

4.3.1.4. Anion Adsorption/Desorption

To determine the quantity of adsorbed active species during pseudocapacitive storage, SANS intensities were collected at six different potentials (including OCP) within the stable potential window as listed in Table 2. The material was held at these selected potentials for approximately an hour, and there was no evidence of any gas evolution, indicating stability. The scattering intensity for the dry material, material at OCP, and material held at selected potentials are shown in Figures (4.5a, 4.5b, 4.5c and 4.5d). There were significant differences in the intensities for dry and wet samples. At low q values, which corresponds to large pores, the addition of electrolyte greatly reduced the scattering intensity which did vary significantly with applied potential. Also the peak at ~0.035 $Å^{-1}$ disappeared after addition of electrolyte, indicating pore filling. At high q values, which correspond to incoherent scattering and small pores, the scattering intensity increased after addition of electrolyte, suggesting insertion of deuteroxide ions into the pores. The decrease of the scattering intensities with applied potential is expected given that adsorption of deuteroxide (OD^-) ion onto VN reduces the scattering intensity based on the SLD of OD, and the angle at which the neutrons are scattered is proportional to the pore size [17,18].

The number of moles of inserted deuteroxide and electrons transferred as a function of applied potential are shown in Figure 4.6. The data are plotted with respect to the OCP. The number of moles of inserted deuteroxide and electrons transferred increased with potential and showed similar slopes. To better understand the charge storage process, the change in OD^- and the change in e^- between -1.0 V and -0.3 V were evaluated. The ratio of the change is ~1. This suggests one mole of e^- transferred per one mole of OD^- adsorbed/desorbed during electrochemical charge storage.

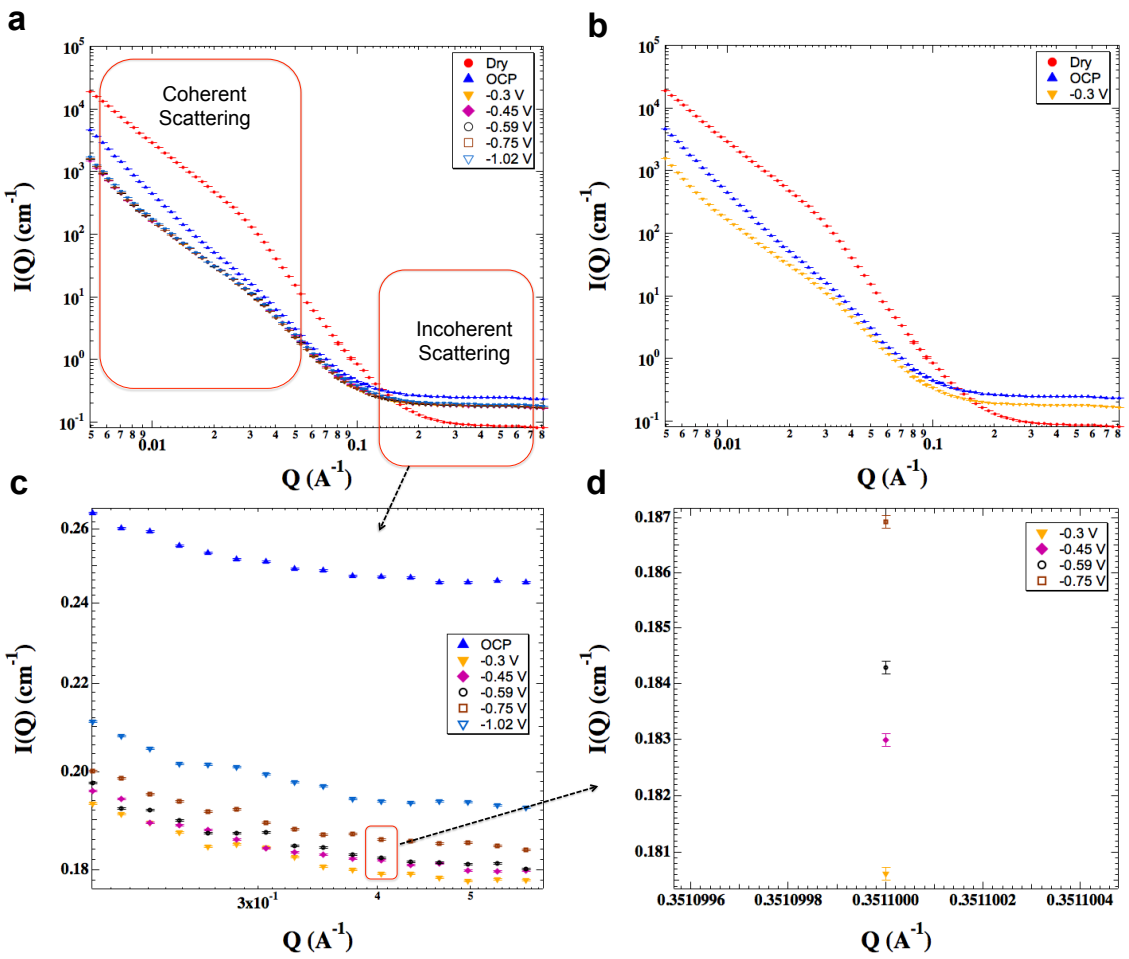

Figure 4.5: (a) Scattering intensities for VN for dry, wet (at OCP), and all selected potentials within the stability window, in 0.1 mol dm^{-3} KOD electrolyte in D_2O solvent, (b) dry, OCP, -0.3 V, (c), (d), enlarged inset plots; revealing significant changes between dry and wet, and subtle changes between selected potentials, all data collected at room temperature.

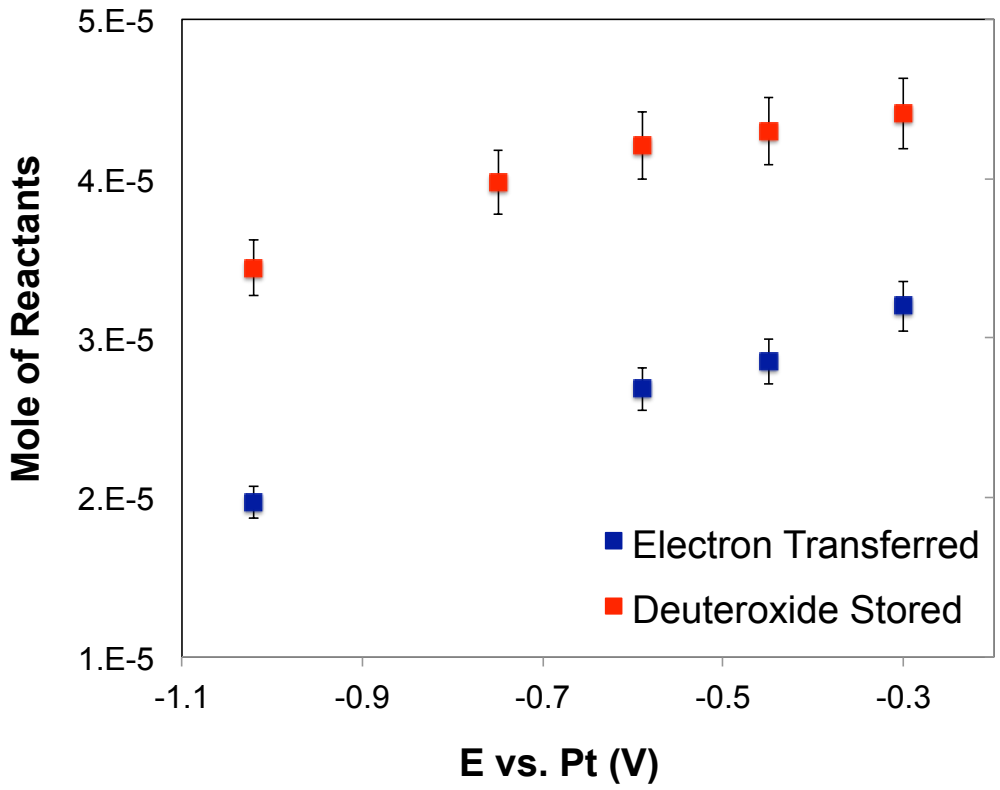

Figure 4.6: Moles of inserted deuteroxide and electrons transferred (with respect to OCP, absolute values are reported), in 0.1 mol dm^{-3} KOD electrolyte in D_2O solvent, revealing adsorption/desorption of deuteroxide and electron transfer into VN material, as a function of applied potential, all data collected at room temperature.

4.3.1.5. Adsorbed Anion-Pore Wall Interactions

To gain greater insight regarding the distribution and the interaction of adsorbed active anions (OD^-) with the pore walls for VN during electrochemical charge storage, the Beaucage model was used to decouple the contribution of the interaction of OD^- with meso- (2-50 nm) and micro-pore walls (<2 nm) from the total scattering. This empirical model links the Guinier (low q, large pores) and Porod (high q, small pores) regimes without introducing new parameters beyond those used in the local fits [8,9]. An excellent fit was obtained for all the scattering data. The fitting parameters are listed in Table 4.2. The Guinier and Porod parameters for mesopores and micropores for the dry

sample, wet sample, and for all selected potentials within the stable potential window are also listed in Table 2. The radius of gyration (R_g) in Eq. (5) is a parameter fit to the data, which corresponds to the size of the pore. The identified values were ~13 nm and ~1.6 nm. These values fall within the mesopore and micropore ranges, suggesting the presence of these pore size ranges in the material. These findings are corroborated by the measured pore size distribution (chapter two). From the Beaucage model, the SLD of ion was calculated using Eq. (6) as shown in Figure 4.8. The SLD reflects the interaction of ion with the pore walls. In general, higher SLD means higher ion-pore wall interaction [6-10]. The SLD from the micropores was higher than that from the mesopores. This indicates that the interaction of ion with the pore walls was greater in micropores than in mesopores.

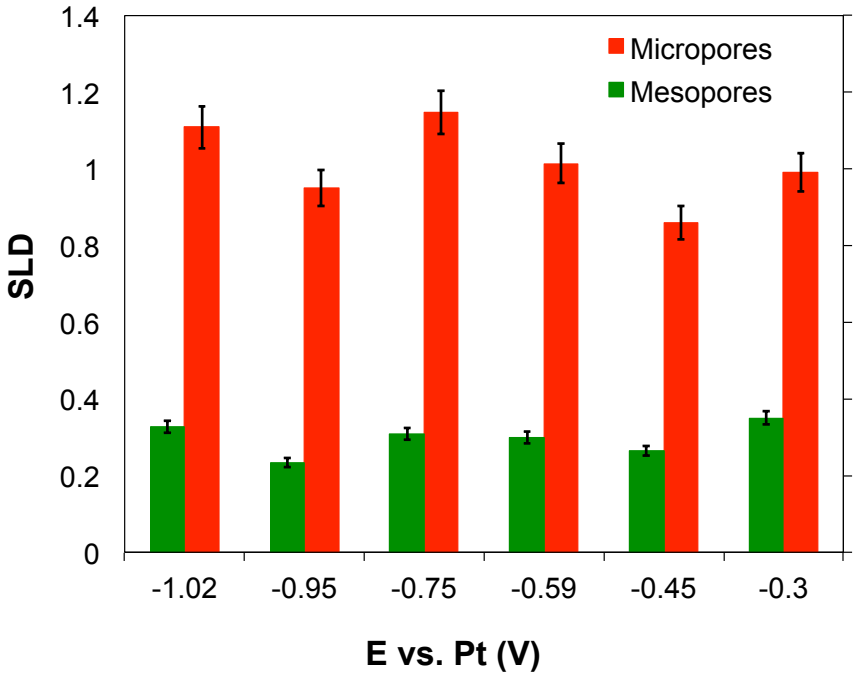

Figure 4.7: Scattering length density from mesopores and micropores as a function of potential in 0.1 mol dm^{-3} KOD electrolyte in D_2O solvent, revealing higher interaction of deuteroxide in the micropores relative to the mesopores.

Table 4.2: Beaucage model parameters for dry, wet (OCP), and all selected potentials (in Volts) within the electrochemical stability window, showing pore sizes (mesopores and micropores), and Guinier and Porod parameters. The units are: Bkg: cm^{-1} sr^{-1}; R: nm.

	Bkg	Mesopores		Micropores	
		Guinier	Porod	Guinier	Porod
		R	P	R	P
Dry	0.029	13.7	4.37	2.1	3.79
OCP	0.080	13.0	3.66	1.5	1.01
-0.30	0.058	12.3	3.59	1.7	1.84
-0.45	0.059	12.5	3.53	1.5	1.59
-0.59	0.060	12.3	3.62	1.6	1.91
-0.75	0.062	12.4	3.62	1.6	2.47
-1.02	0.064	12.4	3.50	1.7	2.26

4.3.1.6. Discussion

The change in edge energy provides direct evidence that electrons were added to a band that is primarily vanadium in character as the material was cycled within its stable window (1.2 V). The overall change is consistent with a unit change in oxidation state leading to reduction of the V metal. From a charge compensation perspective, this would be consistent with a release of one OH^- per e^- as the potential is changed. This was also confirmed using SANS analysis. From SANS, the ratio of OD^-/e^- was ~1 as the potential was changed from an initial potential to the end of the potential window, consistent with XAS analysis. Combining the metal oxidation state change (~1) and the ratio of active species to electron transferred (OH^-/e^- or OD^-/e^- = ~1), the following pseudocapacitive charge storage mechanism was established for VN in aqueous alkaline media:

$$V^{3+}N^{3-} + OH^- \leftrightarrow V^{2+}N^{3-}(\mathrm{OH}) \quad (9)$$

The proposed reaction mechanism differs from the equilibrium reaction mechanism proposed for VN in aqueous alkaline electrolyte by Kumta and co-workers [12]:

$$VN_xO_y + OH^- \leftrightarrow VN_xO_y \parallel OH^- + VN_xO_y - OH \quad (10)$$

While this electrochemical reaction represents a combination of the electric double layer and the pseudocapacitive components for VN_xO_y, it was proposed based on results from *ex-situ* experimental techniques. However, an *ex-situ* approach might be inadequate to understand the dynamic charge storage process in nitride materials. Our proposed reaction mechanism, however, was obtained based on results from *in-situ* experimental techniques. It represents the pseudocapacitive function of the VN material, which accounts for its high capacitance. During charging, OH^- anions adsorb on the VN material, and are released during discharging, as corroborated by the results from SANS. The results indicated that there is more OD present in any of the voltage-dependent measurements than there was in the wet, OCP measurement. Based on Eq. (9), full exploitation of the VN can lead to capacitance of 1350 F g^{-1} within a 1.2 V potential window. Previously, a capacitance of 1340 F g^{-1} was reported for thin film VN electrode in aqueous alkaline electrolyte [12], which is in excellent agreement with our reported value. However, our observed capacitances from CV (Figure 4.2b) are lower than the reported capacitance. The ratio of observed capacitance (240 F g^{-1}) over expected capacitance (1350 F g^{-1}) is ~0.18, suggesting that we were accessing about 20% of the expected capacitance using CV. Unlike SANS or XAS, which can probe the insertion of ions into the bulk and in the pores, CV can only probe charges accumulated on the electrode surface, which may explain the low observed capacitance.

EXAFS analysis revealed that the overall structure is broadly consistent with that expected for VN [19]. During cycling, there are no obvious structural changes as a consequence of V reduction. Perhaps, the insertion of anions (i.e. OH^- or OD^-) occurred in the pores rather than in the bulk. The distribution of adsorbed anions in the pores was

examined using the Beaucage model as mentioned previously. During charging, application of potential induced adsorption of OD^- into the pores, thus decreasing the scattering intensity (Figures 4.5a, b, c and d). The SLD from the micropores was higher than that from the mesopores. This indicates that the interaction of ion with the pore walls was greater in micropores than in mesopores [20-26]. This makes sense given that in micropores, ions are likely to be influenced by the adjacent pore walls, whereas in mesopores ions are likely to be influenced by one pore wall. Therefore, for every inserted ion, there is most likely more interaction in micropores than in mesopores, consistent with our data. Unfortunately, it is very difficult to quantify the total mole of ion confined in the pores given the unknown total accessible volume of micropores using the scattering method. A schematic of the interaction of adsorbed OH^- ions with the pore walls is illustrated in Figure 4.8.

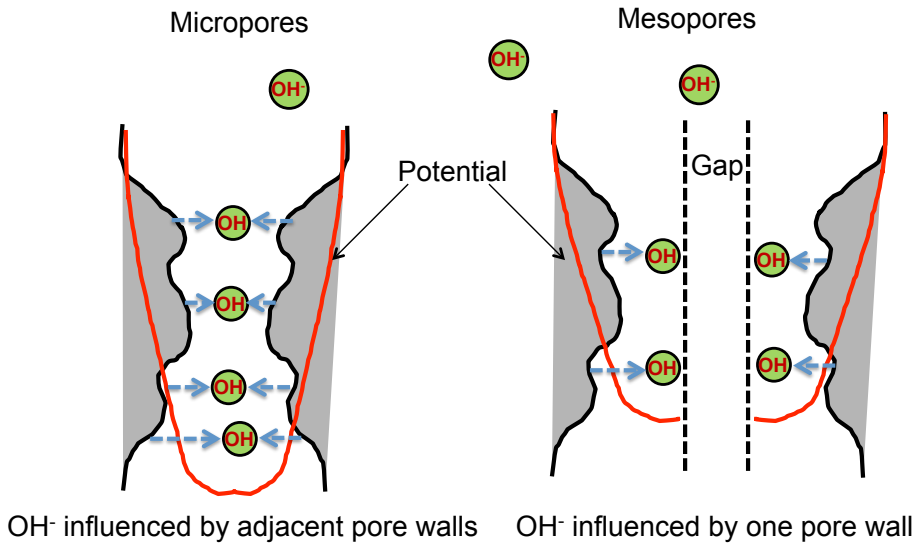

Figure 4.8: Graphical interpretation of the OH^-/wall interaction within micropores and mesopores.

4.3.2. Mo_2N Charge Storage Mechanisms

4.3.2.1. Physical and Electrochemical Properties

X-ray diffraction patterns, pore sizes distribution, and scanning electron micrographs for the γ-Mo_2N (fcc structure) material are reported in chapter two. For convenience, this material will be referred to simply as Mo_2N in this chapter. The pore size distributions indicated the presence of micropores (< 2 nm) and mesopores (2-50 nm). The surface area was ~140 $m^2 g^{-1}$.

Figure 4.9a shows cyclic voltammograms for Mo_2N in aqueous H_2SO_4 electrolytes (H_2O and D_2O solvents). As expected, the voltammograms are nearly identical. The voltammograms include evidence for several redox events in the stable voltage window (1.2 V); these features are consistent with faradaic or pseudocapacitive charge storage processes involving fast, near-surface redox reactions of the electrolyte ions with the electrode material [11-16]. In H_2O and D_2O (see Figure 4.9b), the capacitance decreased logarithmically with increasing scan rate, again, consistent with pseudocapacitive charge storage mechanisms [16]. In both electrolytes, the smallest capacitance was observed at the highest scan rate (~2000 mV s^{-1}). At high scan rates, diffusion limitations reduce the accessibility of protons to the inner surface of the material, and consequently some pores, particularly micropores, are inaccessible [27,28]. The capacitance plateaued at the lowest scan rates (~2 mV s^{-1}). Slightly higher capacitances were observed for Mo_2N in the H_2O-based electrolytes compared to the D_2O-based electrolytes, owing to the higher ionic conductivity of the H_2O solvent, which facilitates the mobility of H^+ into and out of the pores. These observations are similar to those discussed for the VN material.

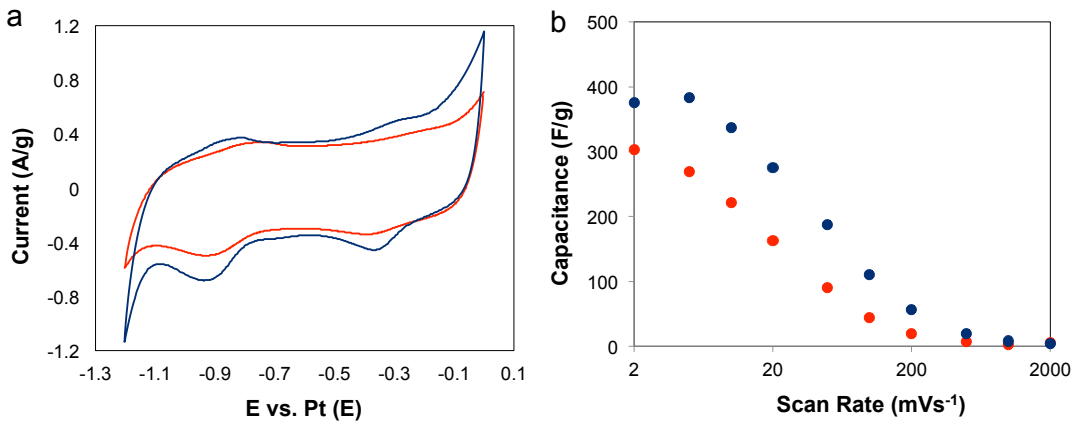

Figure 4.9: (a) Cyclic voltammetry and (b) capacitance behavior with scan rate for Mo_2N in in 0.1 mol dm^{-3} H_2SO_4 electrolytes in H_2O (blue) and D_2O (red) solvents, revealing pseudocapacitive redox activities and total capacitance, all data collected at room temperature.

4.3.2.2. Surface and Bulk Properties

SANS intensities for the dry material, material at the OCP, and material at all selected potentials are shown in Figures (4.10a, 4.10b, 4.10c and 4.10d). For legibility, the material held at -0.46 V is compared to the SANS intensities for the dry material and material held at the OCP in Figure 4.10b. There were significant differences in intensities for the dry and wet samples. At low q values, which corresponds to large pores, the addition of electrolyte reduces significantly the scattering intensity, which does not vary significantly with potential. Also, the peak at ~0.1 $Å^{-1}$ was dissipated after addition of the electrolyte, indicating pore filling. At high q values, which corresponds to incoherent scattering and small pores, the scattering intensity increased after the addition of electrolyte and varied with applied potential. The insertion of hydrogen ions into the material increases the neutron scattering intensity, and the angle at which the neutrons are scattered is proportional to the pore size [17,18].

The moles of inserted hydrogen and electrons transferred are plotted as a function of the applied potential in Figure 4.11a. Both varied significantly with potential and generally followed similar trends, suggesting that during charge storage H^+ and e^- simultaneously interacted with Mo_2N. The minimum amounts of hydrogen and electrons transferred were observed at -0.73 V (versus Pt wire), which is located in the double-layer region (which corresponds to the flat region on the voltammogram, see Figure 4.9a). This is reasonable given that formation of the electrostatic double-layer represents the minimum storage capacity. To better understand the charge storage process, the ratios of H^+ to e^- were analyzed and are plotted in Figure 4.11b. The H^+/e^- remains relatively constant at ~0.5 as the potential was increased from -1.0 V to -0.2 V. This suggests insertion of $2e^-$ for every H^+ into the Mo_2N.

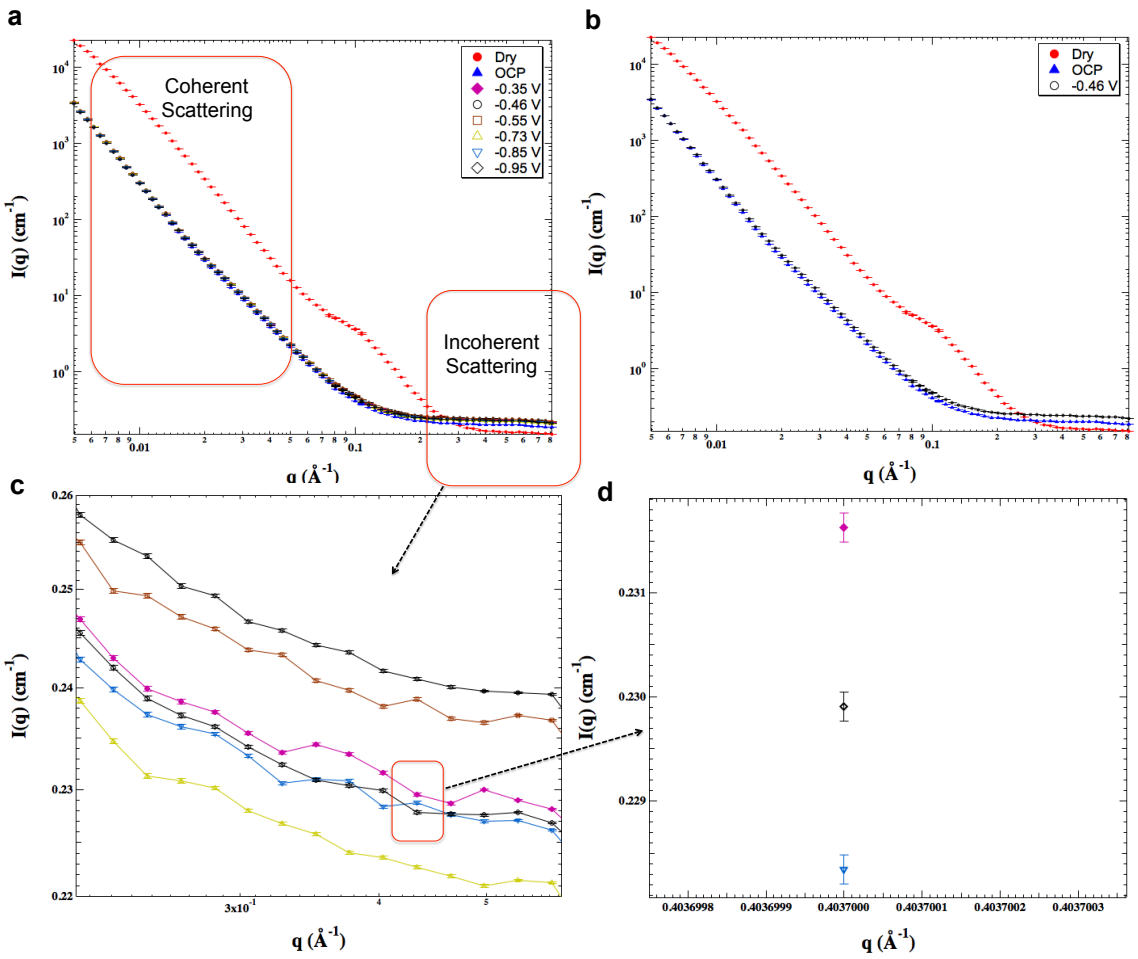

Figure 4.10: (a) Scattering intensities for VN for dry, wet (at OCP), and all selected potentials within the stability window, in 0.1 mol dm^{-3} KOD electrolyte in D_2O solvent, (b) dry, OCP, -0.3 V, (c), (d), enlarged inset plots; revealing significant changes between dry and wet, and subtle changes between selected potentials, all data collected at room temperature.

The Beaucage model was used to understand the interaction of adsorbed H^+ ion with meso- (2-50 nm) and micro- (<2 nm) pore walls. An excellent fit was obtained for all of the scattering data. The fitting parameters are listed in Table 4.3. The identified values for R_g were ~6.8 nm and ~1.8 nm. This suggests the presence of mesopores and micropores as corroborated by the measured pore size distribution (in chapter two). Figure 4.12 shows the SLD as a function of applied potential for the mesopores and the micropores. Note that SLD is a measure of the interaction of the adsorbed H^+ with the

pore walls. Similar to the VN system, the SLD from the micropores was higher than that from the mesopores indicating that the interaction of ion with the pore walls was greater in micropores than in mesopores.

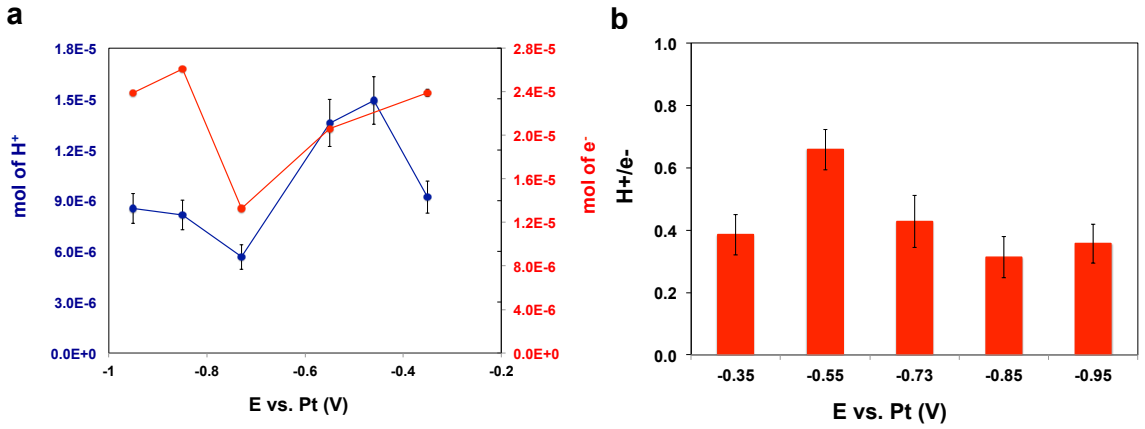

Figure 4.11: (a) Moles of inserted hydrogen and electrons transferred and (b) ratio of adsorbed hydrogen over electron in 0.1 mol dm^{-3} H_2SO_4 electrolyte in D_2O solvent, revealing adsorption of hydrogen and electrons into Mo_2N as a function of applied potential; all data collected at room temperature.

Table 4.3: Beaucage model parameters for dry, wet (OCP), and all selected potentials (in Volts) within the electrochemical stability window, showing pore sizes (mesopores and micropores), and Guinier and Porod parameters. The units are: Bkg: cm^{-1} sr^{-1}; R: nm.

	Bkg	Mesopores		Micropores	
		Guinier	Porod	Guinier	Porod
		R	P	R	P
Dry	0.066	6.8	7.77	1.8	4.02
OCP	0.081	6.6	4.47	1.6	2.75
-0.35	0.093	7.0	3.50	1.8	1.99
-0.46	0.097	6.7	3.50	1.9	2.19
-0.55	0.096	6.7	3.47	1.8	2.19
-0.73	0.089	6.9	3.54	1.9	2.21
-0.85	0.092	6.8	3.51	1.8	2.14
-0.95	0092	6.9	3.58	1.9	2.37

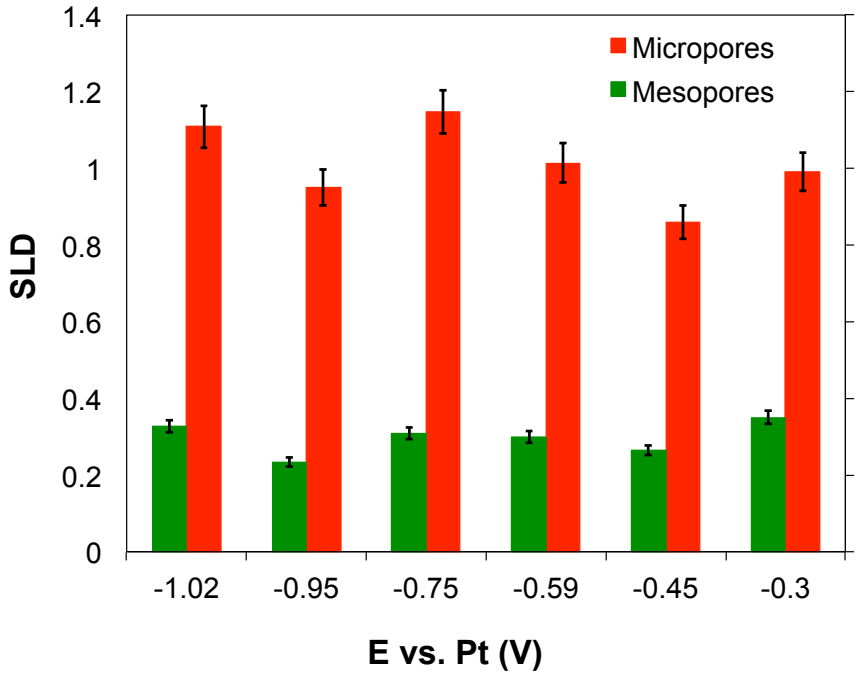

Figure 4.12: Scattering length density from mesopores and micropores as a function of potential in 0.1 mol dm^{-3} H_2SO_4 electrolyte in D_2O solvent, revealing higher interaction of hydrogen in the micropores relative to the mesopores.

4.3.2.3. Discussion

The insertion of hydrogen as a function of potential was characterized by tracking the incoherent scattering intensity as indicated by Eq. 4. The incoherent scattering intensity increased after addition of the electrolyte and continued to increase with applied potential (Figures 4.12a and b). This indicates insertion of more hydrogen into the material, consistent with previous reports [13,14]. In non-electroactive materials such as carbons, changing the applied potential does not affect the capacitance as indicated by the following equation [29]:

$$C_{dl} = \frac{\varepsilon_r \varepsilon_O}{d} A \quad (11)$$

where $\boldsymbol{\varepsilon}_r$ is the electrolyte dielectric constant, $\boldsymbol{\varepsilon}_o$ is the dielectric constant of the vacuum, d is the effective thickness of the double layer (charge separation distance) and A is the

electrode surface area. However, the amount of inserted hydrogen varied non-linearly with the applied potential. This result is consistent with pseudocapacitive charge storage in which the capacitance depends on the applied potential according to the following equation [29]:

$$C_p = \frac{dQ}{dE} \quad (12)$$

where Q is the charge and E is the potential. For a given electrochemical reaction, the charge should be always balanced as dictated by charge neutrality. Therefore, given that the ratio of H^+/e^- is approximately 0.5, the Mo metal in the Mo_2N material must be reduced. The reduction of the Mo was confirmed by XAS. Previous work from the Thompson group has shown that the Mo was reduced by 1 oxidation state during electrochemical charge storage [3,13]. This is consistent with our current findings: both XAS and SANS analysis indicates a proton-coupled electron transfer ($2e^-$ for every H^+) in the charge storage mechanisms. Considering the metal oxidation state change (~1) and the ratio of H^+/e^- (~0.5), we proposed the following charge storage mechanism for Mo_2N in aqueous acidic media:

$$[Mo_2^{\delta}N] + 2H^+ + 4e^- \leftrightarrow [Mo_2^{\delta}N(H)_2]^{2-} \quad (13)$$

Based on this equation, full exploitation of the Mo_2N can lead to a capacitance of 1560 F g^{-1} within a 1.2 V voltage window. As with VN, our observed capacitances from CV (Figure 4.11b) are lower than this expected capacitance. The ratio of observed capacitance (400 F g^{-1}) over expected capacitance (1560 F g^{-1}) is ~0.25, suggesting that we were accessing about 25% of the expected capacitance using CV. The high expected capacitance observed for the Mo_2N material was previously attributed to the insertion of

H^+ into octahedral and tetrahedral interstitial sites in the bulk material [13]. This cannot be accessed using CV.

The significant difference in scattering intensity between dry and wet (at OCP) materials is indicative of pores filled with electrolyte (Figures 4.12a and 4.12b). At the rest potential (before application of potential), ions moved to the Mo_2N (working electrode) and formed an electrostatic double layer at the electrode/electrolyte interface [18]. Upon application of potential, the scattering intensity from pores increased, indicating the adsorption of H^+ into the pores of the material. The interaction of adsorbed H^+ ion with the pore walls was higher in micropores than in mesopores, and varied slightly with applied potential (see Figure 4.12). As illustrated in Figure 4.13, similar to the VN system, the higher SLD of adsorbed H^+ ion in the micropores is due to the shorter distance between the adjacent pore walls. In micropores, ions are likely to be influenced by the adjacent pore walls, whereas in mesopores ions are likely to be influenced by one pore wall [20-26].

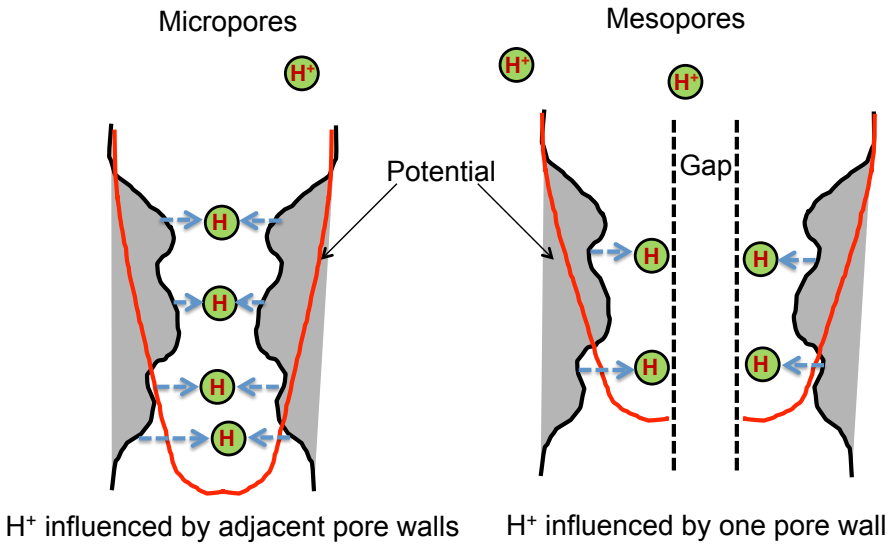

Figure 4.13: Graphical interpretation of the H^+/wall interaction within micropores and mesopores.

4.4. Conclusions

In this chapter, we investigated the pseudocapacitive charge storage mechanisms for VN and Mo_2N using *in-situ* experimental techniques. The results indicated that pseudocapacitive charge storage derived primarily from the adsorption of anions and cations in the pores, leading to reduction of the metals (V^{3+} ➔ V^{2+}, $Mo^{3/2+}$ ➔ $Mo^{1/2+}$), as the VN and Mo_2N materials were electrochemically cycled within their stable potential windows. Pseudocapacitive charge storage mechanisms were proposed based on the combined results from XAS and SANS. High capacitances of over 1300 F g^{-1} (3550 μF cm^{-2}) and 1500 F g^{-1} (1040 μF cm^{-2}) are expected from the VN and Mo_2N materials in full utilization. These values exceeded those reported in the literature for any metal oxides, carbides, and nitrides in aqueous media.

4.5. References

1. J. E. Penner-Hahn, X-ray Absorption Spectroscopy. eLS, (2005).
2. P. Pande, P. Rasmussen, L. Thompson, J. Power Sources, 207 (2012) 212-215.
3. P. Pande, Investigation of Charge-Storage Mechanisms of Early-Transition-Metal Nitrides and Carbides as Electrodes for Electrochemical Capacitors, PhD Thesis, University of Michigan, (2013).
4. B. Ravel, M. Newville, J Synchrotron Radiat., 12 (2005) 537.
5. A. L. Ankudinov, B. Ravel, J. J. Rehr, S. D. Conradson, Phys. Rev., *B* 58 (1998) 7565.
6. G. D. Wignall, K. C. Littrell, W. T. Heller, Y. B. Melnichenko, K. M. Bailey, G. W. Lynn, D. A. Myles, V. S. Urban, M. V. Buchanan, D. L. Selby, P. D. Butler, J. Appl. Cryst., 45 (2012) 990-998.
7. G. D. Wignall, F. S. Bates, J. Appl. Cryst., 20 (1987) 28-40.
8. G. Beaucage, J. Appl. Cryst., (1995), vol. 28, p717-728.
9. G. Beaucage, J. Appl. Cryst., (1996), vol. 28, p717-728.
10. S. R. Kline, J. Appl. Cryst., 39 (2006) 895-900.
11. M. Glushenkov, D. Hulicova, D. Llewellyn, G. Q. Liu, Y. Chen, Chem. Mater., 22 (2010) 914.
12. D. W. Choi, G. E. Blomgren, P. N. Kumta, Adv. Mater., 18 (2006) 1178.
13. P. Pande, A. Deb, A. S. Sleightholme, A. Djire, P. Rasmussen, J. Penner-Hahn, L. T. Thompson, J. Power Sources, 289 (2015) 154-159.
14. T. C. Liu, W. G. Pell, B. E. Conway, J. Electrochem. Soc., 145 (6) (1998) 1882.
15. S. L. Roberson, D. Finello, R. F. Davis, J. Appl. Electrochem., 29 (1999) 75.

16. B. E. Conway, J. Electrochem. Soc., 6 (1991) 138.

17. C. Largeot, C. Portet, J. Chmiola, P. L. Taberna, Y. Gogotsi, and P. Simon, J. Am. Chem. Soc., 130 (2008) 2730-2731.

18. S. Boukhalfa, L. He, Y. B. Melnichenko, and G. Yushin, Angew. Chem., 125 (2013) 4716-4720.

19. V. López-Flores, M. A. Roldán, C. Real, A. Muñoz Páez, G. R. Castro, J. Appl. Phys., 104 (2008) 023519.

20. L. He, Y. B. Melnichenko, N. C. Gallego, C. I. Contescu, J. Guo, and J. Bahadur, Carbon, 80 (2014) 82-90.

21. J. Huang, B. G. Sumpter, V. Meunier, Chem. Eur. J., 14 (2008) 6614-6626.

22. D. Jiang, Z. Jin, D. Henderson, and J. Wu, J. Phys. Chem. Lett., 3 (2012) 1727-1731.

23. S. Boukhalfa, D. Gordon, L. He, Y. B. Melnichenko, N. Nitta, A. Magasinski, and G. Yushin, ACS Nano, 8 (2014) 2495-2503.

24. W. C. Conner, J. P. Fraissard, Fluid Transport in Nanoporous Materials: Proceedings of the NATO Advanced, Springer (2006).

25. P. Simon, A. Burke, J. Electrochem. Soc. Interface, Spring (2008).

26. B. P. Bakhmatyuk, B. Y. Venhryn, I. I. Grygorchak, M. M. Micov, S. I. Mudry, Advanced Study Center Co. Ltd, (2007).

27. R. L. Porto, R. Frappier, J.B. Ducros, C. Aucher, H. Mosqueda, S. Chenu, B. Chavillon, F. Tessier, F. Cheviré, T. Brousse, Electrochimica Acta, 82 (2012) 257-262.

28. M. Toupin, T. Brousse, D. Belanger, Chem. Mater., 14 (2002) 3946-3952.

29. B. E. Conway, Electrochemical Supercapacitors, Kluwer Academic/ Plenum Publishers, (1999).

Chapter 5

Effect of Surface Oxygen

5.1. Introduction

In this chapter, we investigated the effect of surface oxygen on the physical and electrochemical properties of high surface area Ti, V, Nb, Mo, and W carbides and nitrides. The carbides and nitrides were synthesized using the temperature programmed reaction method described in chapter two and passivated to avoid bulk oxidation upon exposure to air. The effects of the oxygen passivation layer on the physical and electrochemical properties were probed in two steps.

First, the passivated materials were pretreated in 0.3 mol dm^{-3} NaOH solution to remove the oxygen-rich passivation layer. This pretreatment resulted in significant changes in the physical and electrochemical properties of the carbides and nitrides. The surface areas of the Mo and W-based materials were higher after activation, with the effect ranging from an 11% increase for Mo_2N to a 208% increase for W_2C. Increases in the pore volume and mesopore density were also observed for most of the materials. The capacitances of all of the materials were increased after pretreatment with the effect ranging from 40% for VN to a 79% increase for (α+β)-Mo_2C. This pretreatment process could be used to improve the performance of carbide and nitride-based supercapacitor electrode materials.

Next, we compared and contrasted the physical and electrochemical properties of passivated and non-passivated carbides and nitrides. There were increases in the surface areas and pore volumes of the non-passivated Mo and W-based materials. These results were consistent with those observed for pretreated materials. Additionally, non-passivated Nb-based materials showed an increase in the surface areas as compared to their passivated counterparts. As expected, the increase in the surface areas of the non-passivated materials led to a significant enhancement in the specific capacitances. Moreover, the areal specific capacitances of the non-passivated materials were slightly higher at low scan rates when compared to those of the passivated materials. This indicated an improved pseudocapacitive storage in the non-passivated materials. This improvement in the electrochemical performance is due to the absence of an oxide layer on the non-passivated materials.

5.2. Experimental Methods

5.2.1. Passivated Materials

All the passivated carbide and nitride materials used in this study were synthesized using the temperature-programmed reaction method described in chapter two. In this chapter, the term passivated materials refers to materials that had a thin oxide layer on their surfaces, unless otherwise stated. Physical properties were evaluated using X-ray diffraction analysis (XRD), N_2 physisorption analysis using the Brunauer–Emmett–Teller (BET) and Barrett-Joiner-Helenda (BJH) methods, and scanning electron microscopy (SEM) (see chapter two). The electrochemical characterization of the materials was carried out in aqueous 0.1 M H_2SO_4 electrolytes using the three-electrode

electrochemical setup shown in Figure 5.1. This type of electrochemical cell is more practical [1] for this kind of study and is different from the one used in chapter three. In order to eliminate oxygen from the electrolytes, a flowing stream of $N_{2\,(g)}$ was bubbled through the aqueous electrolytes for at least 30 min prior to the experimental measurements, and maintained as a blanket over the solution during experiments. A Pt flag and $Hg/HgSO_4$ (Sat. K_2SO_4, Radiometer Analytical) were used as the counter electrode (CE) and reference electrode (RE), respectively. The electrodes were connected to an Autolab PGSTAT302N potentiostat as described in chapter three.

The working electrode (WE) was prepared by mixing the as-prepared material (80 wt. %), carbon black (10 wt. %, Super PLi (TIMCAL) and polyvinylidene fluoride (10 wt. %, Kynar) in a N-methylpyrrolidione solvent (Alfa Aesar). The resulting slurry was spread onto a fresh Ti foil and then dried in a vacuum at 80°C for 8 hours. The mass of the active material was determined by subtracting the mass of the Ti substrate from the mass of the coated electrode (Ti + active material). This preparation technique resulted in electrodes that had approximately 3 mg of the active material coated on the substrate.

5.2.2. Pretreated Materials

After synthesis, prior to physical and electrochemical characterization, the passivated materials were pretreated in 0.3 mol dm^{-3} NaOH for 1 min, then sequentially rinsed with acetone, ethanol, and ultrapure water (18 MΩ.cm, Millipore Milli-Q Advantage A10) to remove the oxygen passivation layer that was deposited on the materials during synthesis. The pretreated materials were dried under vacuum at 100 °C for 48 hours, then transferred to a glove box where samples for the XRD and SEM analysis were placed in a custom-made, air-tight sample holder. Surface area and pore

size distribution analyses were performed after the materials were pretreated, dried, and degassed in a vacuum at 350 ºC for 24 hours. Prior to the electrochemical characterization, the pretreated materials were immediately transferred into the electrochemical cell in order to avoid re-oxidation of the materials.

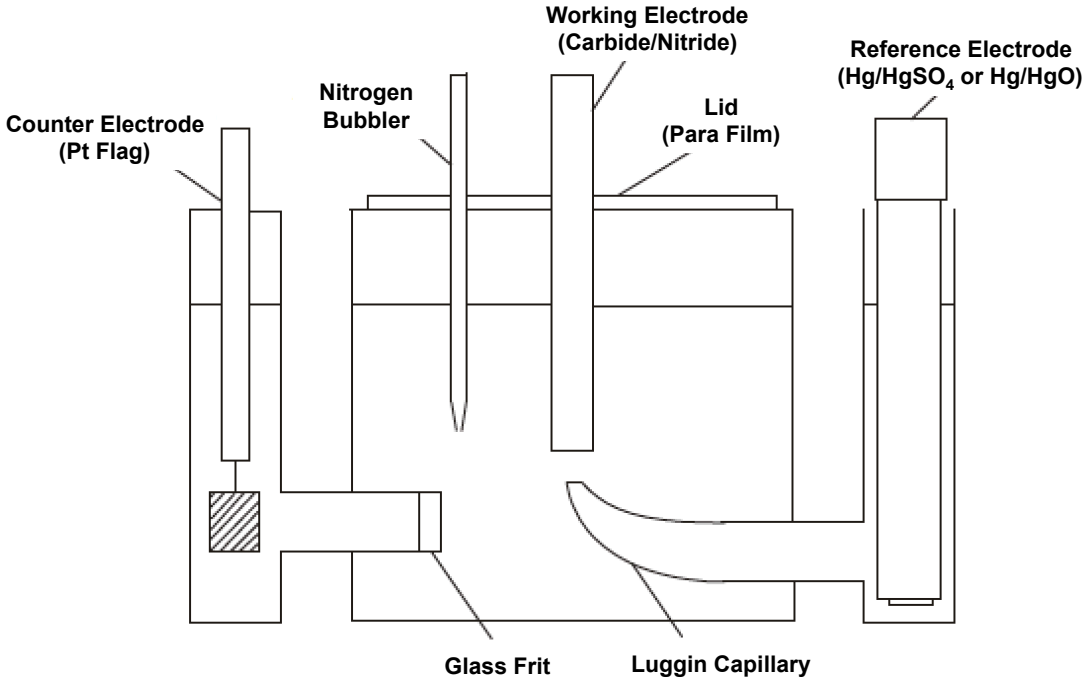

Figure 5.1: Schematic of a quartz three-electrode cell showing the central working electrode chamber and the reference and counter electrode chambers. The luggin capillary connects the working and the reference electrode chambers. The counter electrode chamber is isolated from the working electrode chamber by a porous glass frit.

5.2.3. Non-Passivated Materials

Non-passivated materials had no oxide layer on the surface, and were characterized using the same characterization techniques as described above. Due to the pyrophoric nature of the materials, all experiments were performed in a glove box to avoid exposure of the materials to air. Figure 5.2 shows the experimental flow chart

illustrating the different steps taken prior to the electrochemical characterization. Additionally, the airtight, three-electrode electrochemical cell (ECC-Aqu, EL-Cell FmbH, Germany) described in chapter three (see Figure 3.1) was used in this study to prevent the exposure of the materials to air.

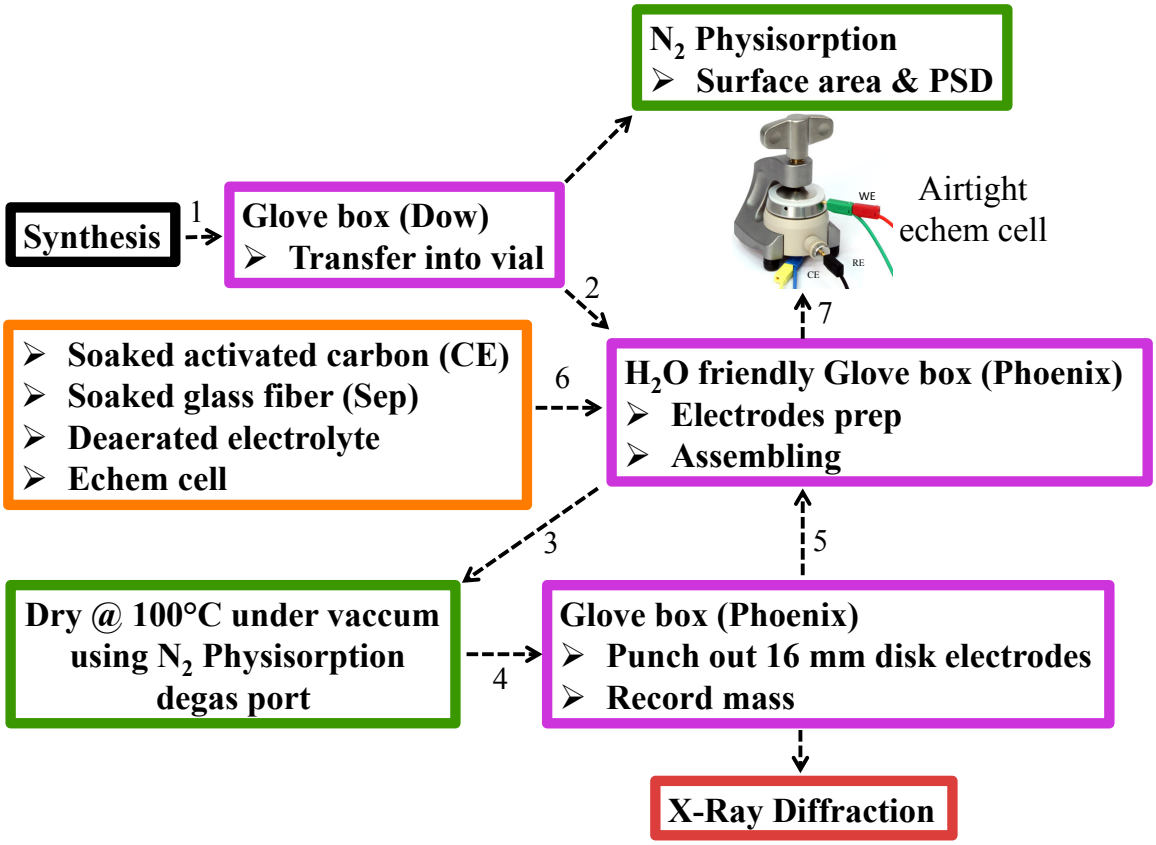

Figure 5.2: Experimental flow chart illustrating the different steps involved in the characterization of native carbides and nitrides.

5.2.4. Surface Oxygen Characterization

H_2 temperature-programmed reduction (H_2-TPR) experiments were used to characterize the oxide on the surface of the materials. These experiments were performed using a Micromeritics AutoChem 2910 Chemisorption Analyzer equipped with thermal

conductivity (TCD) and mass spectrometer detectors. Prior to the H_2-TPR experiments, both the passivated and pretreated materials were purged in flowing He (70 mL min^{-1}) at 200 °C for 2h to remove any residual air present in the reactor. After cooling to room temperature (RT), the catalysts were heated to 800 °C in 10% H_2/Ar at a linear heating rate of 20 °C/min and the TCD signal was recorded.

5.3. Results and Discussion

5.3.1. Effects of Oxygen Passivation Layer on Charge Storage

5.3.1.1. Physical Properties

The XRD patterns for the passivated and pretreated Mo, V and W carbides and nitrides are shown in Figure 5.3. These materials were selected for this study because of their high areal specific capacitances, as described in chapter three. With the exception of (α+β)-Mo_2C, the materials were phase pure. Based on the XRD analysis, the (α+β)-Mo_2C was approximately an equal mixture of α-Mo_2C and β-Mo_2C. No oxide peaks appeared in the XRD patterns of the materials before or after pretreatment. The peak intensities for the passivated and pretreated materials were essentially the same and there were no peak shifts. These results indicated that the passivated and the pretreated materials had the same crystal structure and bulk composition.

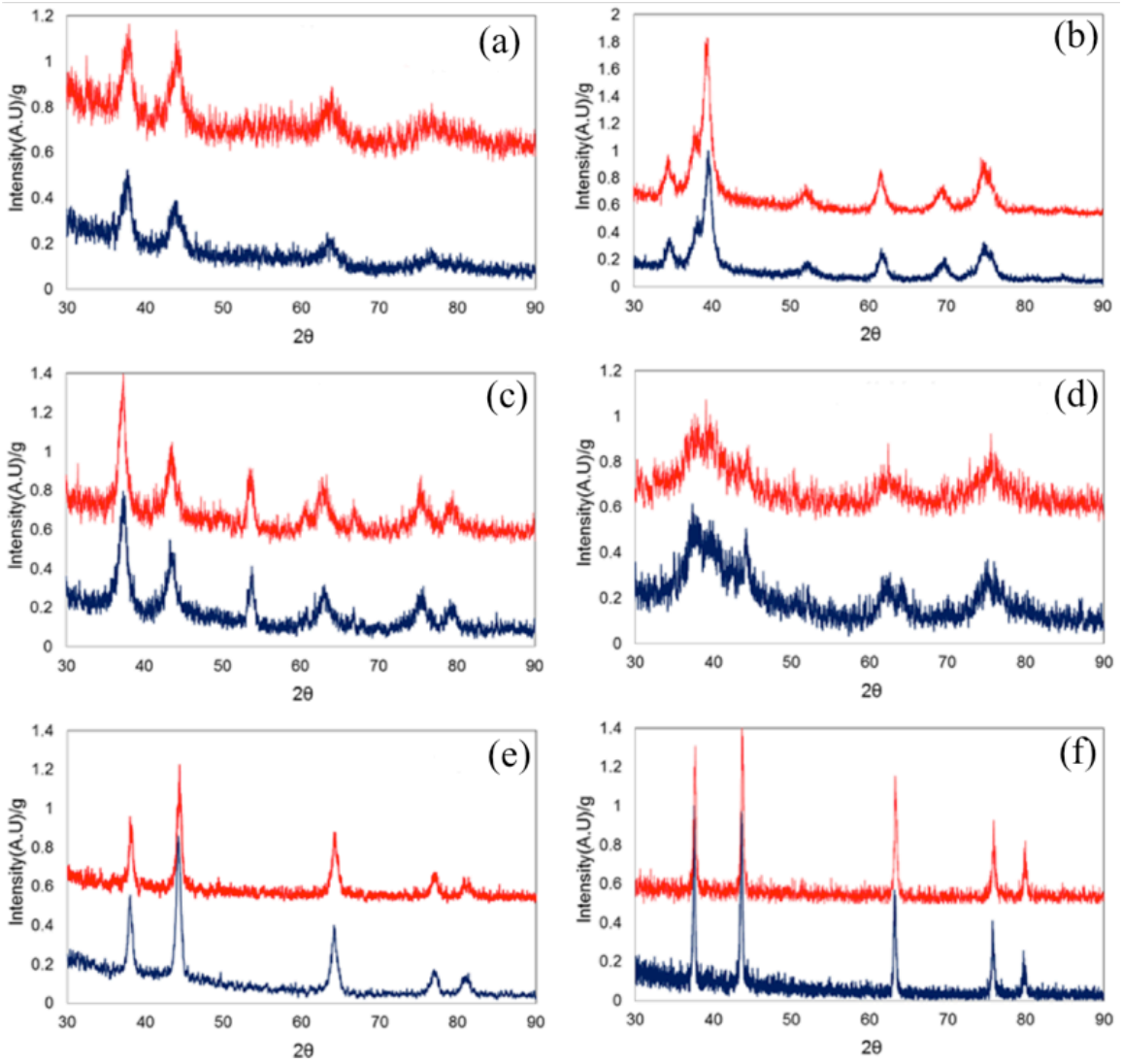

Figure 5.3: X-ray diffraction patterns of passivated (blue) and pretreated (red) (a) W_2N, (b) W_2C, (c) Mo_2N, (d) (α+β)-Mo_2C, (e) VN and (f) VC materials.

Surface areas for Mo, V and W carbides and nitrides are listed in Table 5.1. The surface areas for the Mo and W-based materials were higher after the pretreatment process, with the effect ranging from an 11% increase for Mo_2N to a 208% increase for W_2C. This enhancement is likely due to the removal of the oxygen-rich layer on the surface of the passivated material, allowing greater access of N_2 during physisorption.

Pore size distributions for the materials before and after pretreatment are shown in Figure 5.4. There was an increase in the pore volume for the Mo and W-based materials and an increase in the mesopore density for all of the materials after pretreatment. With the exception of W_2N, all of the materials exhibited at least two maxima, shown on the pore size distributions, indicating the presence of at least two distinctive pore sizes in the materials. The pretreatment process resulted in a ~ 15 nm average pore size increase for VN (Figure 5.4e). The pore size distribution for VC is somewhat different from the rest of the studied materials, possibly due to its relatively low surface area [2-8]. The enhanced density of mesopores in the activated materials would provide greater accessibility for charge storage. No change in the surface area was observed for the VN and VC materials. These materials contained mostly meso- and macropores. The lack of change in the surface area of these materials is likely due to the lack of micropores, particularly in VC. For these materials, the available pores were large enough for N_2 introduction before and after pretreatment.

Table 5.1: Surface areas of passivated and pretreated Mo, V and W carbides and nitrides.

Material	Specific surface areas (m^2 g^{-1})	
	Passivated	Pretreated
Mo_2N	144	160
$(\alpha+\beta)$-Mo_2C	82	102
Mo_2C	51	100
VN	32	32
VC	5	4
W_2N	62	99
W_2C	13	40

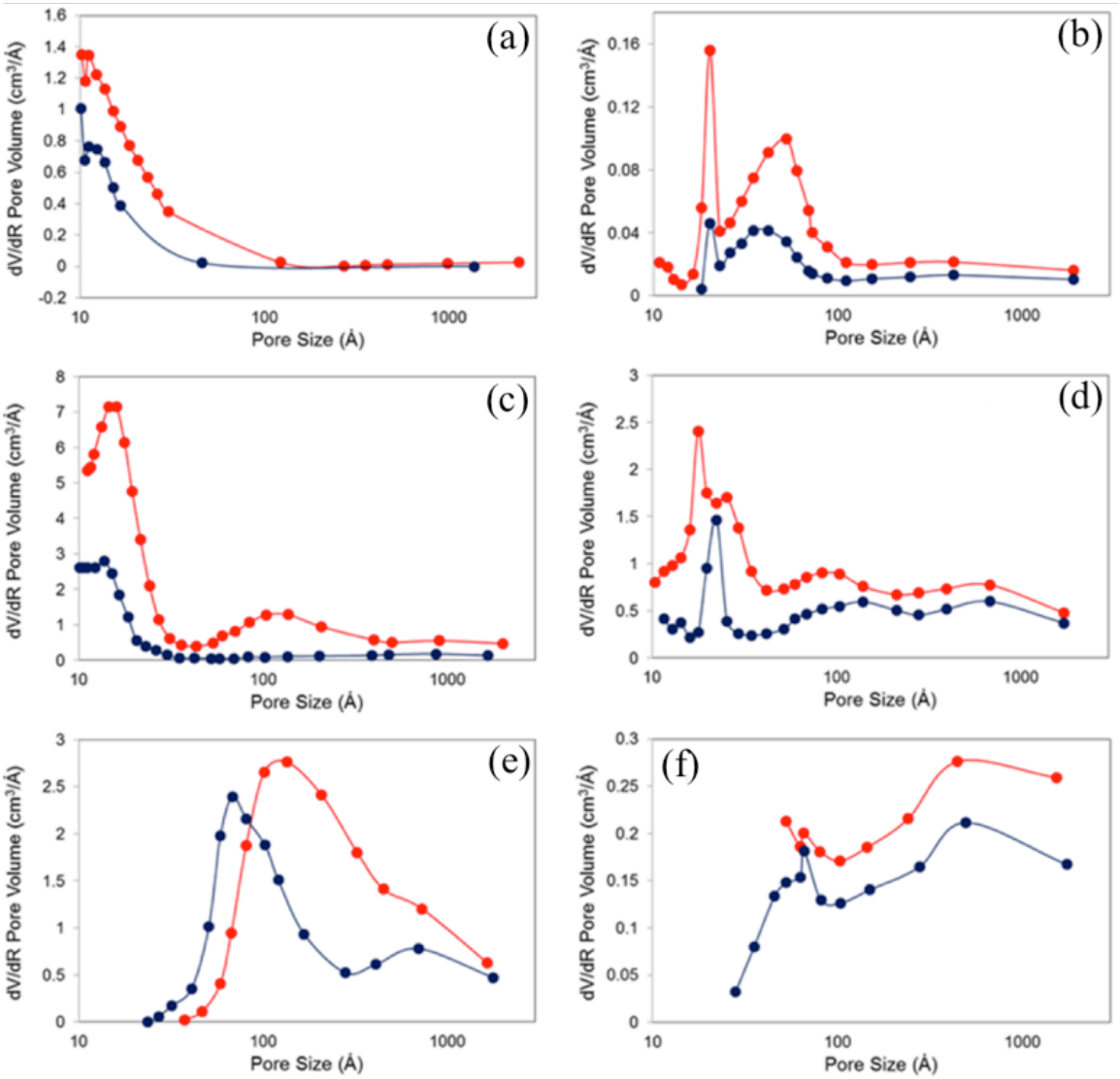

Figure 5.4: Pore size distributions of passivated (blue symbol) and pretreated (red symbol) (a) W_2N, (b) W_2C, (c) Mo_2N, (d) (α+β)-Mo_2C, (e) VN and (f) VC materials.

SEM images of the passivated and pretreated W, Mo, and V carbides and nitrides are shown in Figure 5.5. In general, the surface morphologies varied significantly across samples. Typically, the pretreated materials appeared to be more porous than the passivated materials. In addition, the contrast for the pretreated materials was different from that for the passivated materials. The exception was that micrographs for the passivated and pretreated VN and VC materials were similar; this was not so surprising

given that the surface areas did not change. Overall, these findings are consistent with the results from the surface area and pore size distribution analyses.

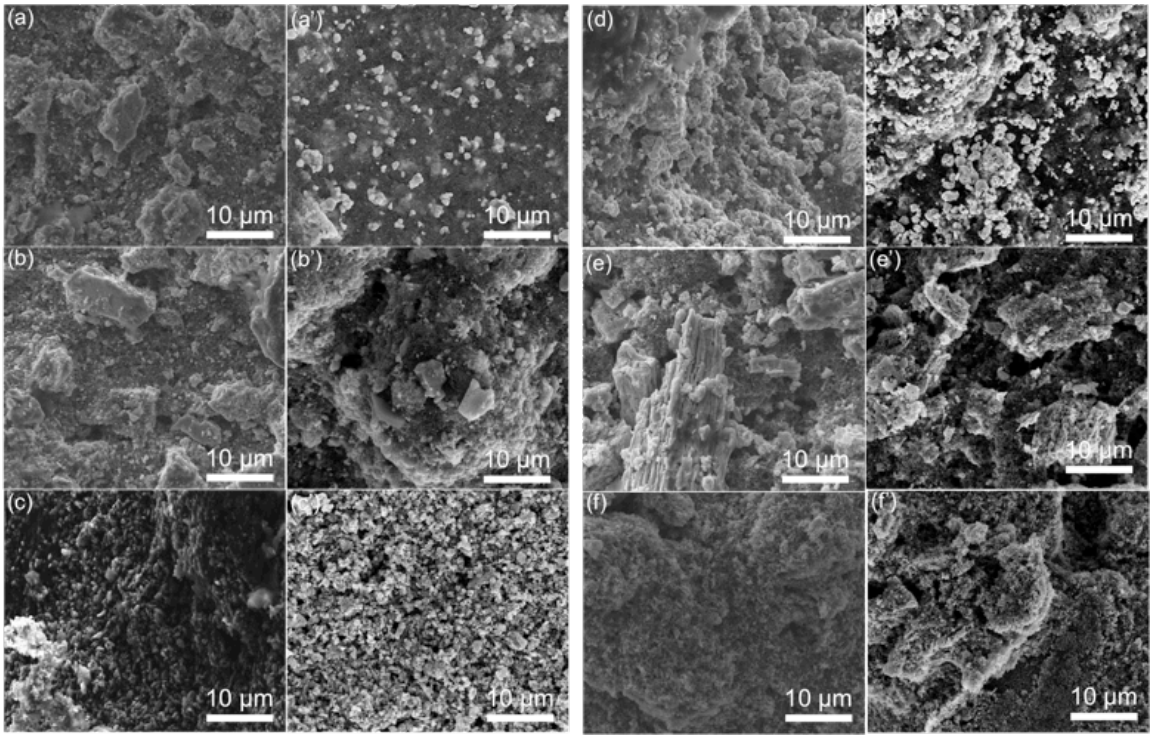

Figure 5.5: Scanning electron micrographs of passivated (a) W_2N, (b) Mo_2N, (c) VN, (e) W_2C, (f) (α+β)-Mo_2C, (g) VC and activated (a') W_2C, (b') Mo_2N, (c') VN, (e') W_2C, (f') (α+β)-Mo_2C, (g') VC materials.

5.3.1.2. Electrochemical Properties

Figure 5.6 shows cyclic voltammograms of the passivated and pretreated materials in 0.1 mol dm^{-3} H_2SO_4 at 50 mVs^{-1}. Due to the relatively high scan rate, voltammograms for the materials that exhibited high surface areas such as Mo and W-based materials show no prominent redox peaks. At high scan rates, diffusion limitations reduce the accessibility of electrolyte active ions to the inner surface of the material, and consequently some pores; in particular, micropores remain inaccessible [9,10]. For the

VN material, redox couples were observed at approximately -0.33/-0.37 V, 0.37/0.32 V and 0.55/0.48 V. The positions and intensities for these redox couples are similar to those previously observed for the material as reported in chapter three. The peak separations approached the theoretical value of 59 mV, suggesting that the redox reactions were highly reversible. The pretreated VC material produced a sharp, reversible redox couple at approximately -0.39/-0.45 V and a broad couple at approximately -0.025/-0.078 V (near the end of the stable voltage window). In agreement with findings from chapter three, the lack of faradaic redox activity on the voltammogram of passivated VC suggests a double-layer charge storage mechanism [9-19].

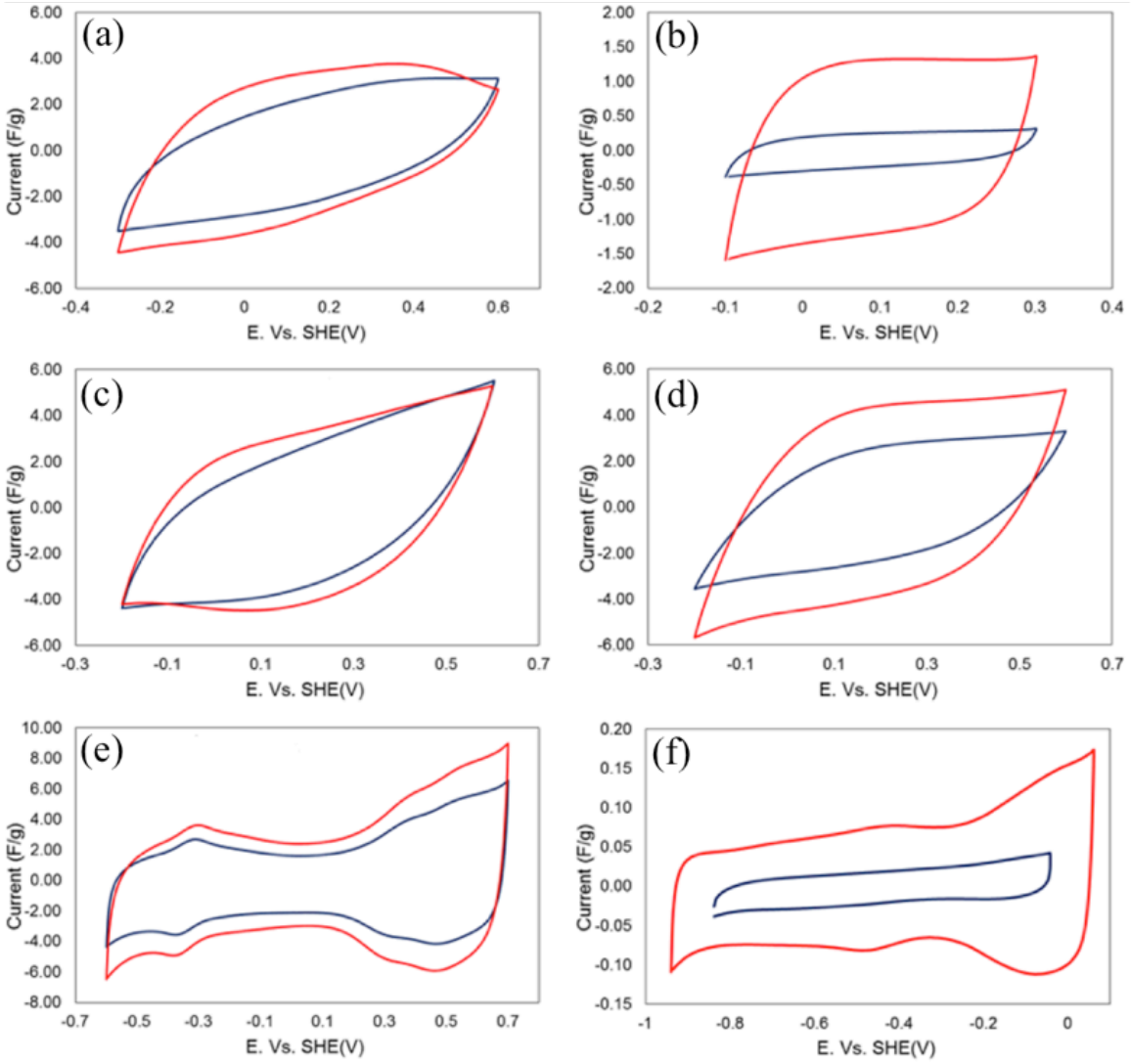

Figure 5.6: Cyclic voltammograms of passivated (blue) and pretreated (red) (a) W_2N, (b) W_2C, (c) Mo_2N, (d) (α+β)-Mo_2C, (e) VN and (f) VC in 0.1 mol dm^{-3} H_2SO_4 at a scan rate of 50 mV s^{-1}. The 1000th scan is shown.

The specific capacitances of the materials were estimated from the cyclic voltammograms, as described in chapter three. The voltammograms were collected at 50 mVs^{-1}. Table 5.2 lists the specific capacitances and normalized areal specific capacitances of the passivated and pretreated materials. Specific capacitances for all of the materials were higher after the pretreatment. The effect ranged from a 43% increase for VN to a 79% increase for (α+β)-Mo_2C. Furthermore, there was a significant increase

in the areal specific capacitances observed for most of the materials after pretreatment. The enhanced capacitances and stabilities, in the case of VC and W_2C, were attributed to the removal of some of the oxygen rich passivation layer, resulting in the exposure of the underlying carbide or nitride. This would result in an increase in the active surface area and allow greater accessibility of electrolyte ions to the pores of the materials. The lower capacitances for the passivated materials suggest that the passivation layer inhibits the pseudocapacitance.

Table 5.2: Specific capacitances and normalized capacitances of passivated and pretreated Mo, V and W carbides and nitrides measured in 0.1 mol dm^{-3} H_2SO_4 at 50 mVs^{-1}.

Material	Specific capacitances (Fg^{-1})		Areal specific capacitances (μFcm^{-2})	
	Passivated	Pretreated	Passivated	Pretreated
Mo_2N	100	148	70	93
$(\gamma+\beta)$-Mo_2C	80	143	96	140
VN	60	100	188	313
VC	Unstable	6	Unstable	150
W_2N	70	120	113	121
W_2C	Unstable	46	Unstable	115

To assess the electrochemical cycle life of Mo, V and W carbides and nitrides, the passivated and pretreated materials were subjected to extended cycling. Figure 5.7 shows the capacitance as a function of cycle number for the Mo_2N, $(\alpha+\beta)$-Mo_2C, VN and W_2N materials in H_2SO_4 electrolyte. Pretreatment resulted in enhanced capacitances, which persisted for more than 2,000 cycles (> 24 hours). For the passivated $(\alpha+\beta)$-Mo_2C, Mo_2N and W_2N materials, the capacitance increased during the first few cycles. This could be due to wettability issues or material instabilities during the first few hours of cycling. Overall, both passivated and pretreated materials demonstrated good cycle life and capacitance retention.

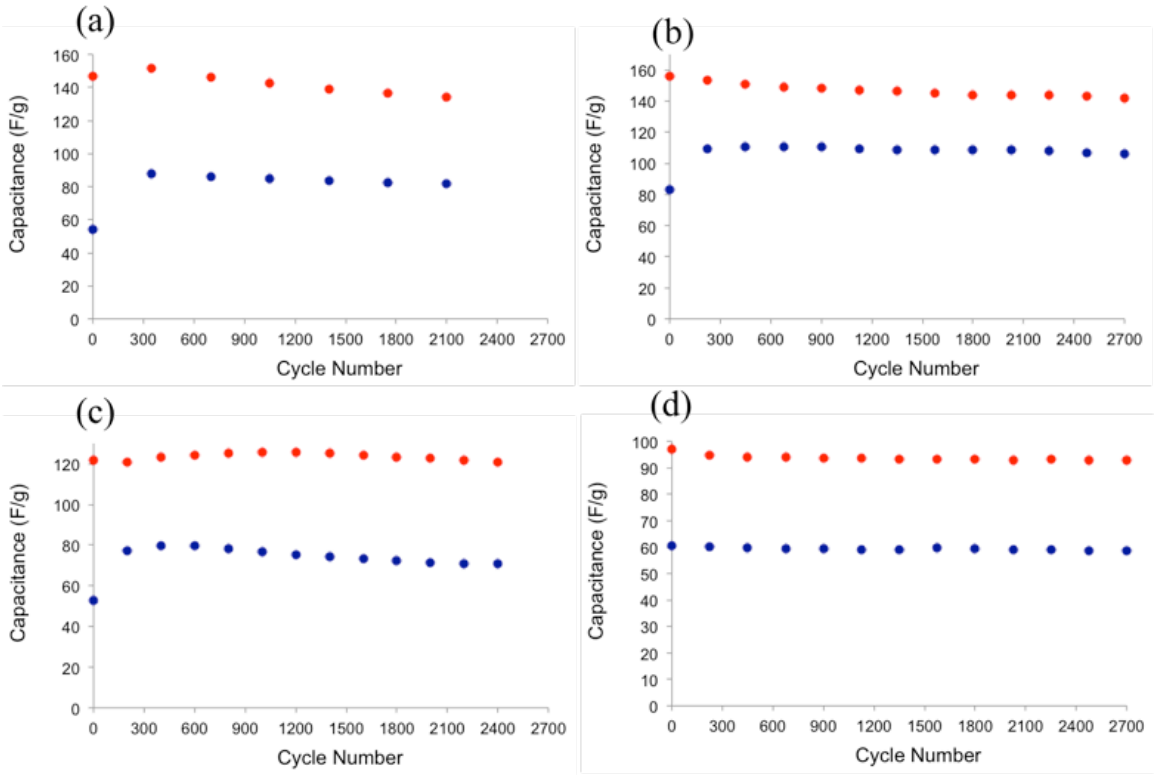

Figure 5.7: Capacitance of passivated (blue) and pretreated (red) (a) (α+β)-Mo_2C, (b) Mo_2N, (c) W_2N and (d) VN in 0.1 mol dm^{-3} H_2SO_4 as a function of cycle number (scan rate = 50 mV s^{-1}).

5.3.1.3. Surface Properties

The H_2-TPR results were used to quantify the amount of deposited oxygen in the passivated and pretreated materials. The area under the H_2O desorption peaks provides a quantitative measure of the amount of oxygen and the temperature is an indication of the strength of the interaction of oxygen with the surface of the material. Figure 5.8 shows H_2O desorption spectra for the Mo, V and W carbides and nitrides. For most of the materials, there was a slight shift in the peak positions towards lower temperatures after the pretreatment process. This could be an indication of a weakening in the oxygen bonding with the surface caused by the pretreatment. The Mo_2N and W_2N materials desorbed comparable amounts of oxygen (as H_2O) at higher temperatures. Table 5.3 lists

the amounts of oxygen on the passivated and pretreated materials. Overall, for all the materials, there was a significant reduction in the surface oxygen content after the pretreatment process. The degree of reduction in the surface oxygen was more significant for the carbides than the nitrides. These observations are in good agreement with the electrochemical results discussed earlier (see Figure three).

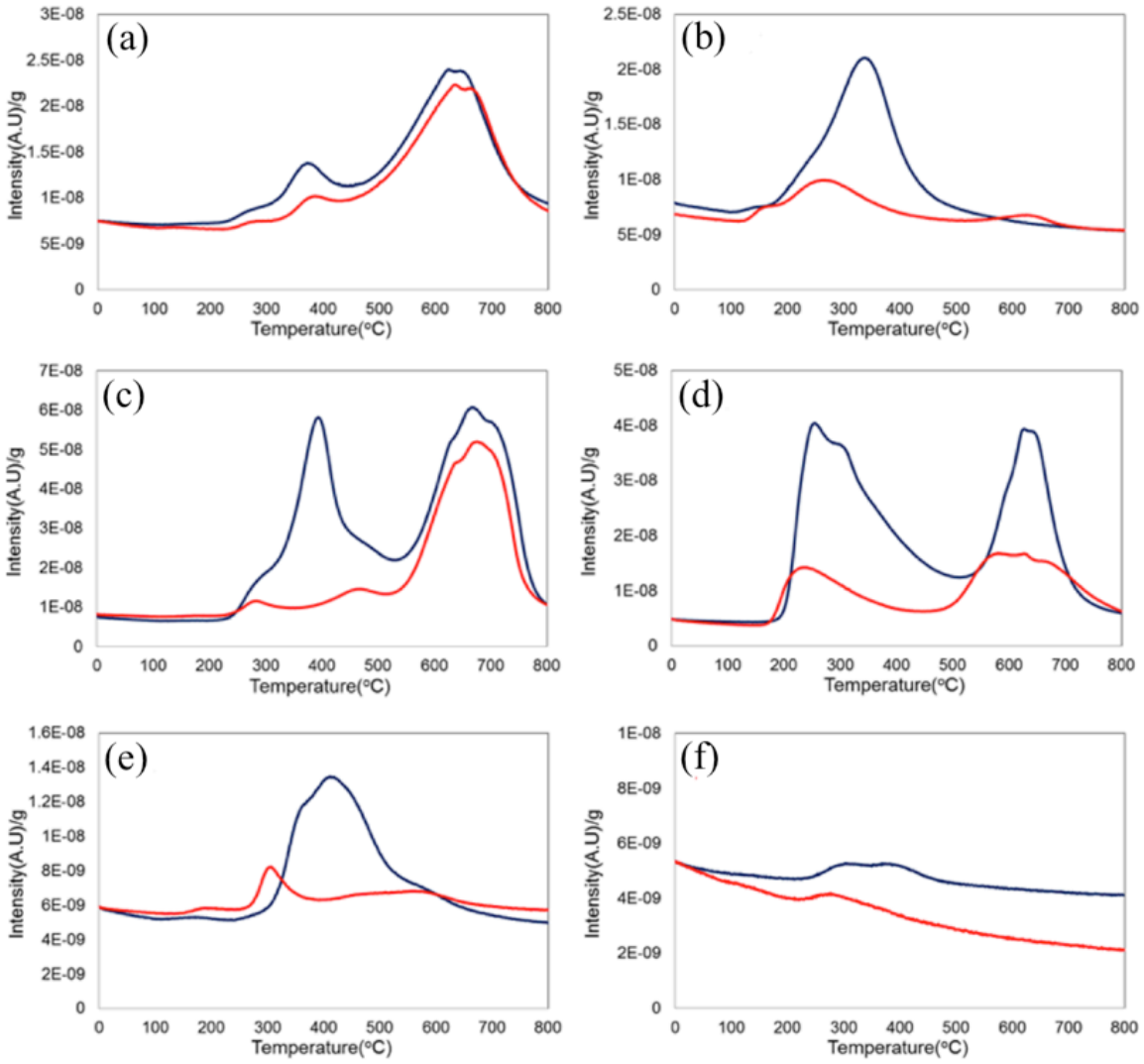

Figure 5.8: Water desorption spectra of passivated (blue) and pretreated (red) (a) W_2N, (b) W_2C, (c) Mo_2N, (d) (α+β)-Mo_2C, (e) VN and (f) VC materials.

Table 5.3: Oxygen contents determined from the TPR measurements of passivated and pretreated Mo, V and W carbides and nitrides.

Material	Oxygen content (μmol g^{-1})		
	Passivated	Pretreated	% Reduction
Mo_2N	203	106	48
(α+β)-Mo_2C	132	39.1	71
VN	23.5	5.87	75
VC	17.1	2.64	85
W_2N	57.3	43.3	25
W_2C	44.2	18.3	59

% Reduction was obtained using this formula 100(passivated-pretreated)/passivated

Although we observed significant improvements in the physical and electrochemical properties of carbides and nitrides after the pretreatment process, a detailed mechanism of the pretreatment is still unclear. Surfaces of the passivated materials were likely covered by the associated metal oxide, oxycarbide or oxynitride [20]. Most transition-metal oxides dissolve in alkaline solutions, as indicated in the Pourbaix diagrams [21]. It is plausible that oxycarbides and oxynitrides would also dissolve in solutions of NaOH, a strong base. The acetone and ethanol treatment would help remove any organic contaminants from the surface, and treatment with ultra-pure water would remove any residual acetone and ethanol from the surface. The resulting surface would be expected to be relatively free of oxides and carbonaceous contaminants. Further experiments using x-ray photoelectron spectroscopy and inductivity coupled plasma (ICP) are needed to better understand the pretreatment process.

5.3.2. Correlation Between Passivated and Non-Passivated Carbides and Nitrides

The pretreatment process removed some, but not all, of the surface oxygen as shown in Table 5.3. Given that this removal of surface oxygen layer resulted in

improvements in the physical and electrochemical properties, we hypothesized that non-passivated carbides or nitrides would exhibit enhanced physical and electrochemical properties as compared to the passivated counterparts. To test this hypothesis, we compared and contrasted the physical and electrochemical properties of passivated and non-passivated Ti, V, Nb, Mo and W carbides and nitrides.

5.3.2.1. Physical Properties

Results from the XRD analysis indicated that all the synthesized materials were phase pure. There were no oxide peaks present in neither of the passivated and non-passivated samples, as expected. The peak intensities for the passivated and non-passivated materials were essentially the same and there were no peak shifts.

The pore sizes distributions of passivated and non-passivated materials are shown in Figures 5.9 to 5.12. Micropore analysis was performed on low-surface area passivated and non-passivated materials such us Ti and V-based carbides and nitrides to gain detailed insights into the differences in their physical properties. For all the materials, the pore size distributions for passivated and non-passivated samples were very similar. Unlike in the pretreatment study, there was no evidence of pore size range shifts in the pore size distributions. We noted that the pore size distribution for the non-passivated NbC showed two distinct maxima as compared to passivated counterpart, which showed one peak (see Figure 5.10b). This difference in the pore size distributions can be attributed to the presence of oxygen on the surface of the passivated material [22,23]. There was an increase in the pore volume for all the non-passivated samples as indicated in the pore size distributions. Table 5.4 lists the surface areas for all the passivated and non-passivated carbides and nitrides. Consistent with the pore size distributions results,

surface areas for non-passivated materials were significantly higher than those for passivated materials. This is attributed to the increase in the pore volume (see Figures 5.9 to 5.12). Consistent with the pretreatment results, the V-based materials did not show any improvement in the surface areas. The surface areas for passivated and non-passivated W_2N were similar. Overall, carbides showed greater effects as compared to nitrides. These findings are in good agreement with those reported in the pretreatment study.

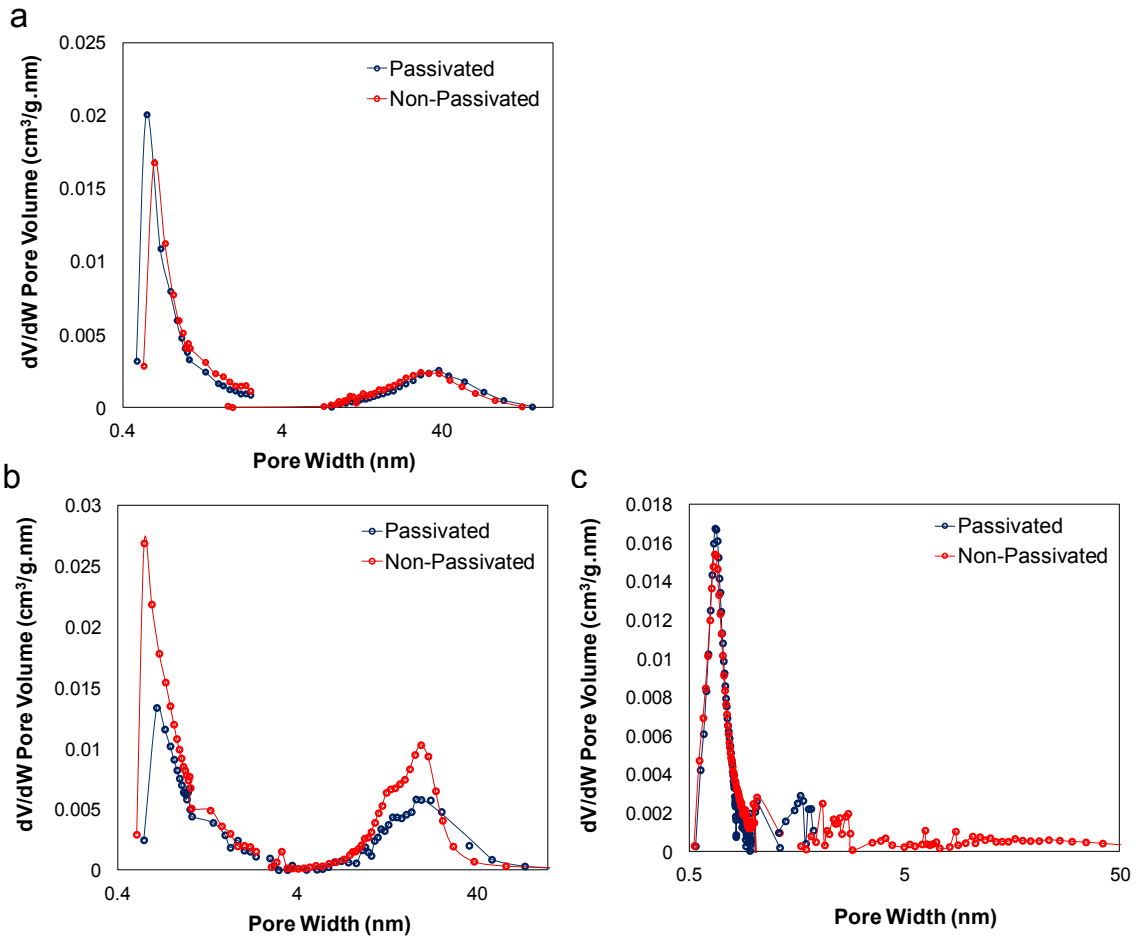

Figure 5.9: Pore size distributions of passivated (blue) and non-passivated (red) (a) TiN, (b) VN, and (c) VC materials.

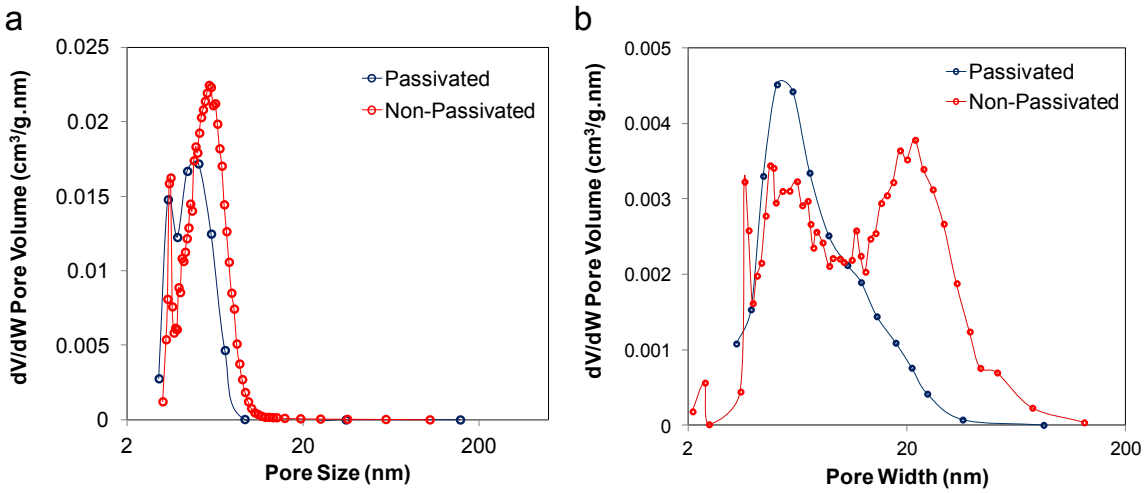

Figure 5.10: Pore size distributions of passivated (blue) and non-passivated (red) (a) NbN, and (b) NbC materials.

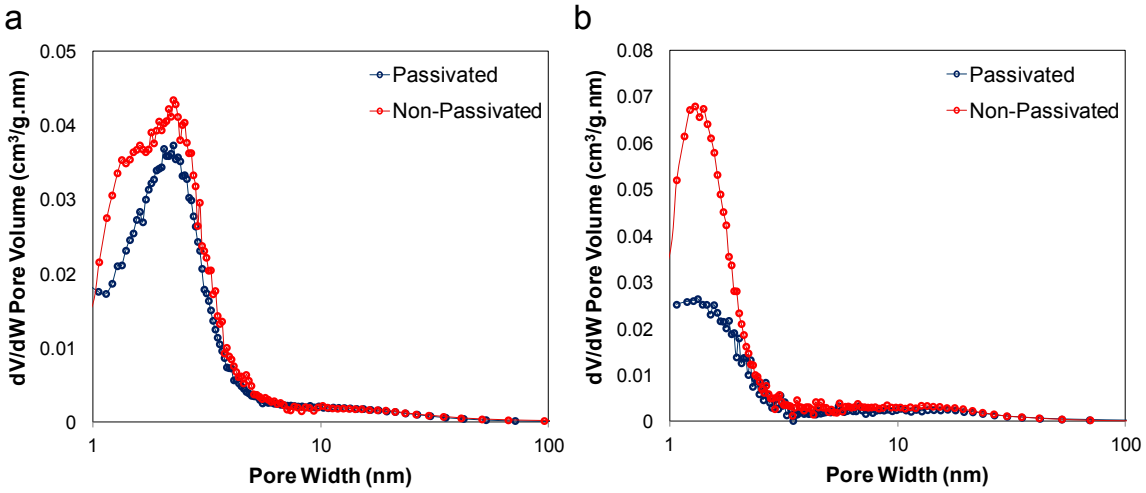

Figure 5.11: Pore size distributions of passivated (blue) and non-passivated (red) (a) (a) Mo_2N, and (b) (α+β)-Mo_2C.

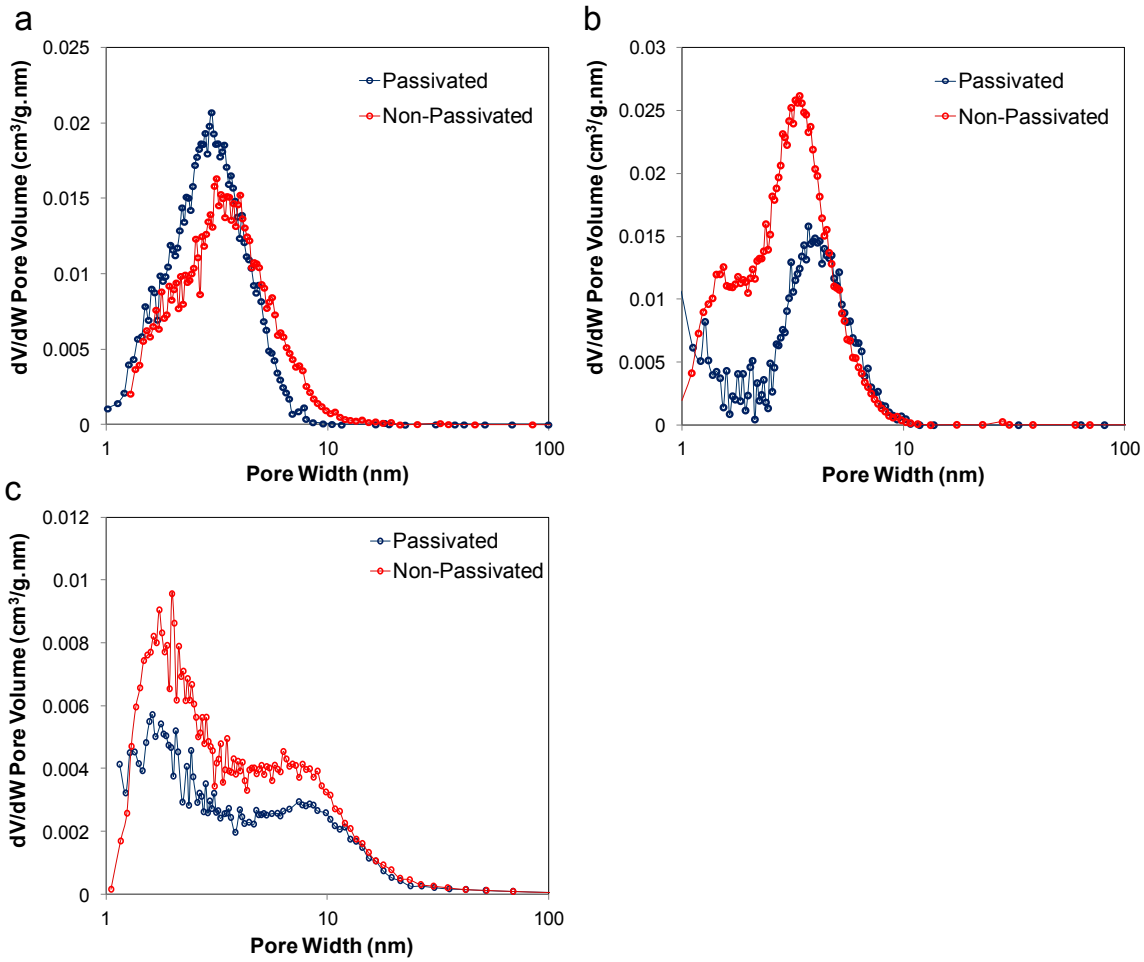

Figure 5.12: Pore size distributions of passivated (blue symbol) and non-passivated (red) (a) W_2N, (b) WC_{1-x}, and (c) W_2C.

Table 5.4: Surface areas of passivated and non-passivated Ti, V, Nb, Mo, and W carbides and nitrides

Material	Specific surface areas (m^2g^{-1})	
	Passivated	Non-Passivated
VN	34	33
VC	9	10
Mo_2N	136	169
$(\alpha+\beta)$-Mo_2C	77	147
W_2N	68	67
W_2C	30	45
WC_{1-x}	55	95
TiN	18	20
NbN	26	44
NbC	16	33

5.3.2.1. Electrochemical Properties

The electrochemical properties for all the materials in aqueous H_2SO_4 and KOH electrolytes were assessed using cyclic voltammetry analysis. The voltammograms and areal specific capacitances recorded at different scan rates for passivated and non-passivated Ti, V, Nb, Mo, and W carbides and nitrides are shown in Figures 5.13 to 5.22. Additionally, the specific capacitances for those materials that exhibited enhancements in the surface areas are shown. The voltammograms shown here were collected at 2 mVs^{-1}, unlike in the pretreatment study during which we used a higher scan rate (50 mVs^{-1}) to avoid re-passivation of the materials during the electrochemical characterization. The electrochemical cell (see Figure 5.1) used in the pretreatment study was not suitable for air-sensitive experiments. Hence, we used the one shown in chapter three (Figure 3.1).

The location of the faradaic redox peaks on the voltammograms for the various carbides and nitrides are consistent with those reported in chapter three. The redox features in the voltammograms for passivated and non-passivated materials are similar, suggesting similar charge storage mechanisms. Interestingly, the redox peaks in the voltammograms for non-passivated materials are more pronounced than those of the passivated materials. This is attributed to the absence of the oxide passivation layer on the non-passivated materials. It is likely that the presence of an oxide passivation layer inhibits the adsorption of electrolytes ions into the pores [22-24].

As expected, the increase in the surface areas led to an improvement in the specific capacitances (see Figures 5.13 to 5.22). Both passivated and non-passivated materials showed similar capacitance behaviors with scan rate. The areal specific capacitances for the passivated and non-passivated Mo- and W-based materials were comparable. Interestingly, the non-passivated T, V, and Nb carbides and nitrides showed improvement in the areal specific capacitances, particularly at lower scan rate (~2 mVs^{-1}). Perhaps the number of active site per surface area in the non-passivated T, V, and Nb materials is higher than that in the passivated counterparts. It is possible that the oxygen passivation layer masks some of the electrochemically active sites. Although we observed significantly higher enhancement in the capacitance of non-passivated NbN as compared to its passivated counterpart, the capacitance dropped significantly when we repeatedly cycled the material at 50 mVs^{-1} (see Figures 5.16c and e), suggesting instability of NbN in aqueous H_2SO_4 electrolyte. Perhaps the lower capacitance observed for the passivated NbN is due to loss of capacitance after the initial cycles. The areal specific capacitances for the VC and NbC in H_2SO_4 electrolyte are comparable to the expected double-layer

capacitance for porous materials (40 μF cm^{-2}) [9-12], indicating that these materials store charge via a double-layer charge storage mechanism, consistent with the electrochemical results from chapter three.

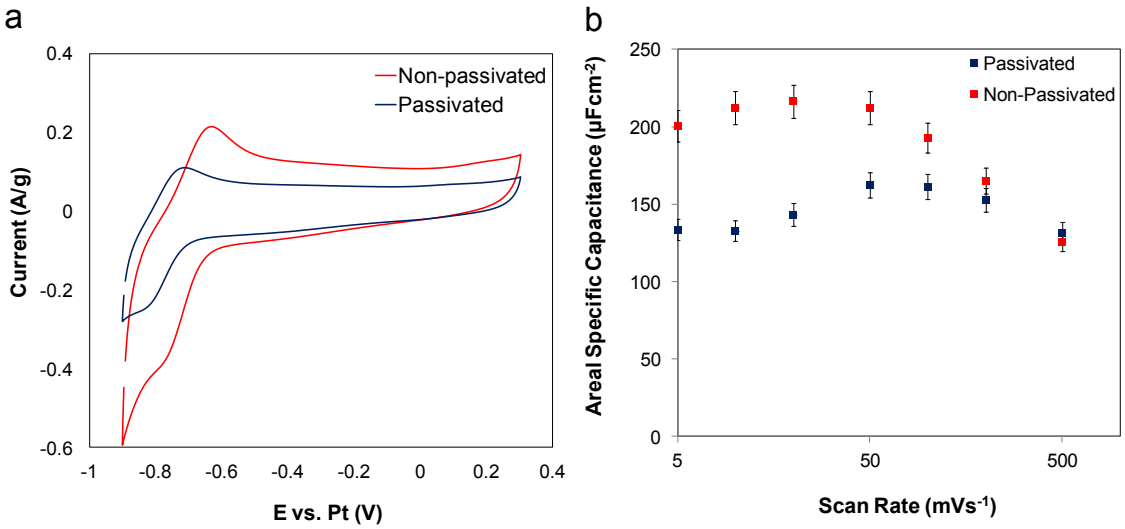

Figure 5.13: (a) Cyclic voltammograms (scan rate = 2 mV s^{-1}) and (b) areal specific capacitances of passivated (blue) and non-passivated (red) TiN in 0.1 mol dm^{-3} H_2SO_4. The 2nd scan is shown here.

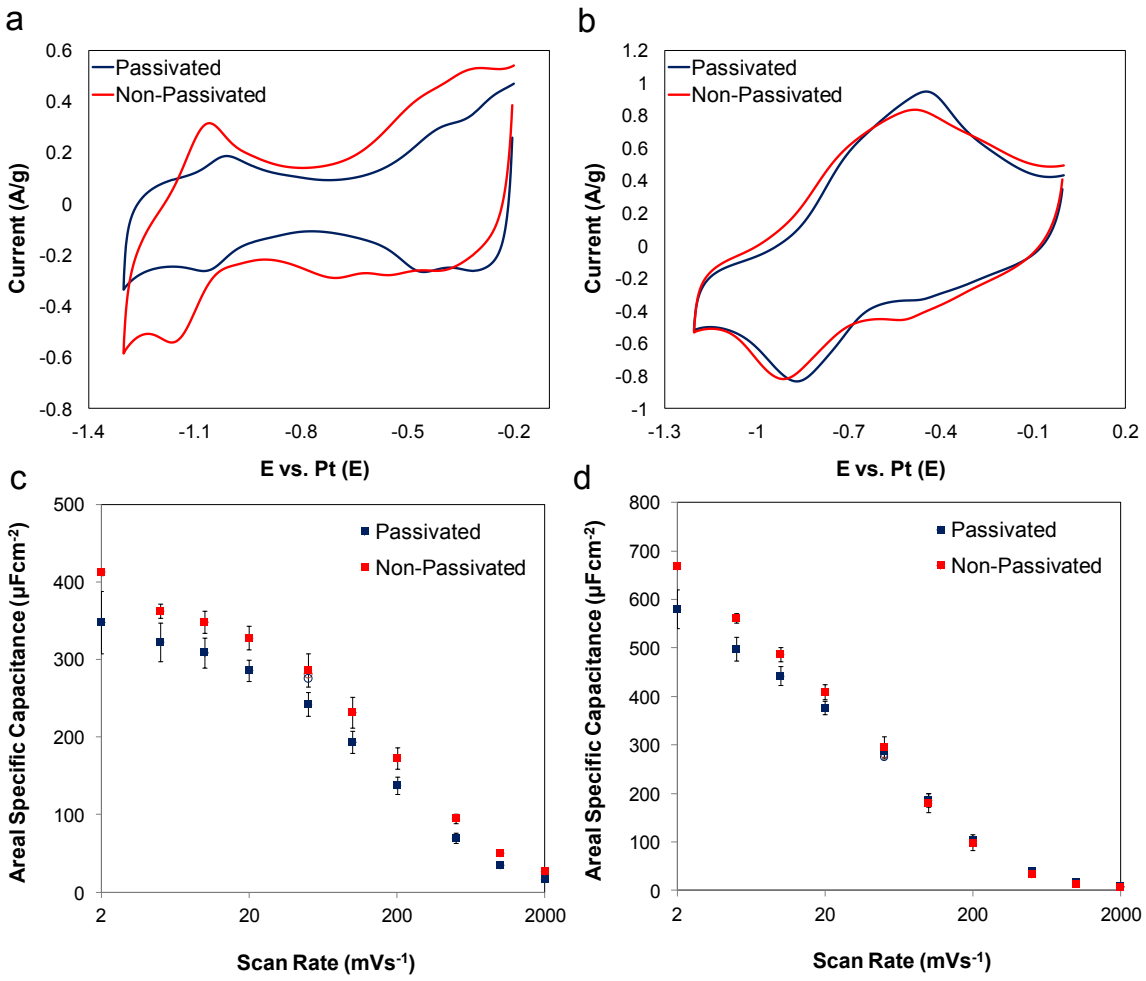

Figure 5.14: (a), (b) Cyclic voltammograms (scan rate = 2 mV s^{-1}) and (c), (d) areal specific capacitances of passivated (blue) and non-passivated (red) VN in 0.1 mol dm^{-3} H_2SO_4 (left) and in 0.1 mol dm^{-3} KOH (right). The 2nd is shown here.

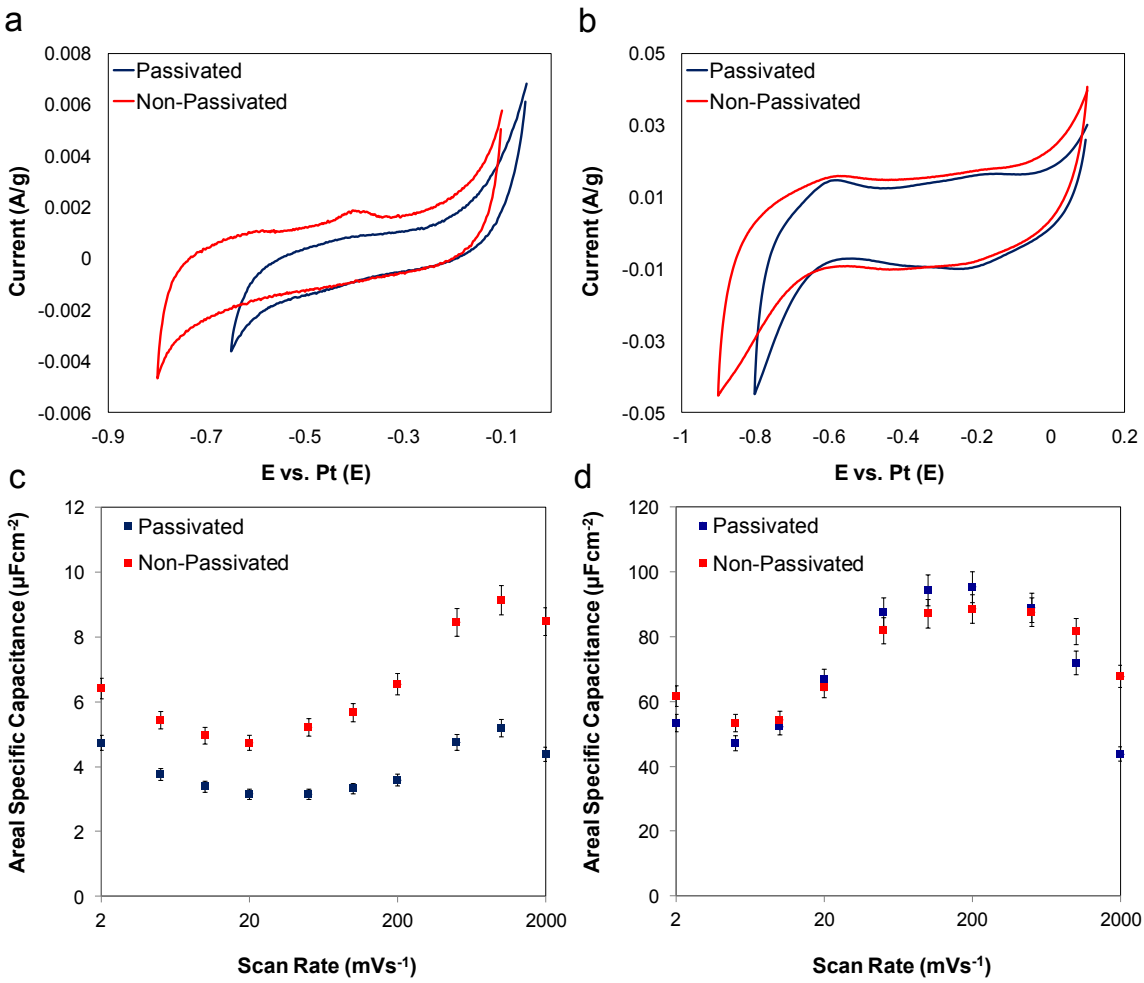

Figure 5.15: (a), (b) Cyclic voltammograms (scan rate = 2 mV s^{-1}) and (c), (b) areal specific capacitances of passivated (blue) and non-passivated (red) VC in 0.1 mol dm^{-3} H_2SO_4 (left) and in 0.1 mol dm^{-3} KOH (right). The 2nd is shown here.

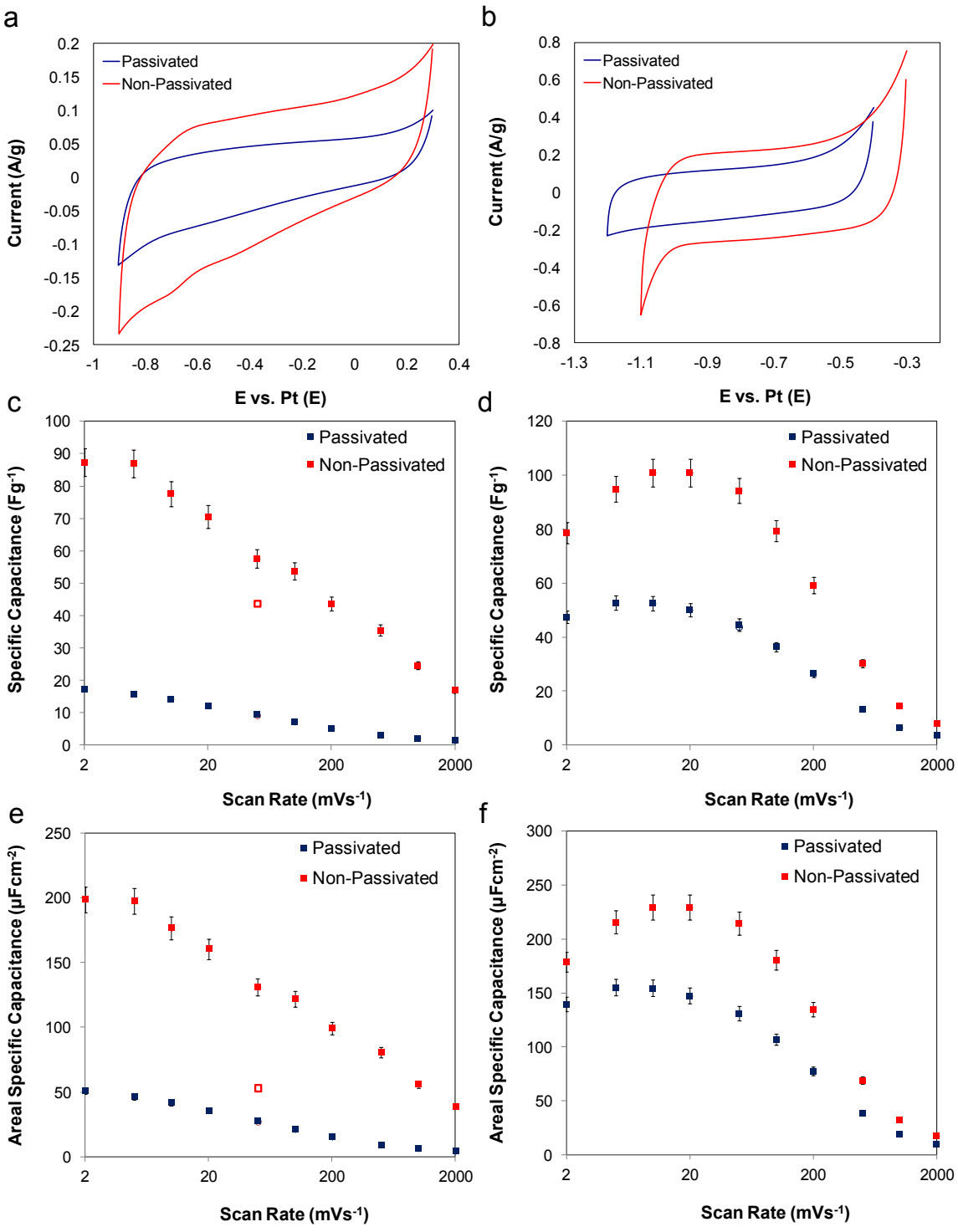

Figure 5.16: (a), (b) Cyclic voltammograms (scan rate = 2 mV s^{-1}) and (c), (d) specific capacitances, and (e), (f) areal specific capacitances of passivated (blue) and non-passivated (red) NbN in 0.1 mol dm^{-3} H_2SO_4 (left) and in 0.1 mol dm^{-3} KOH (right). The 2^{nd} scan is shown here.

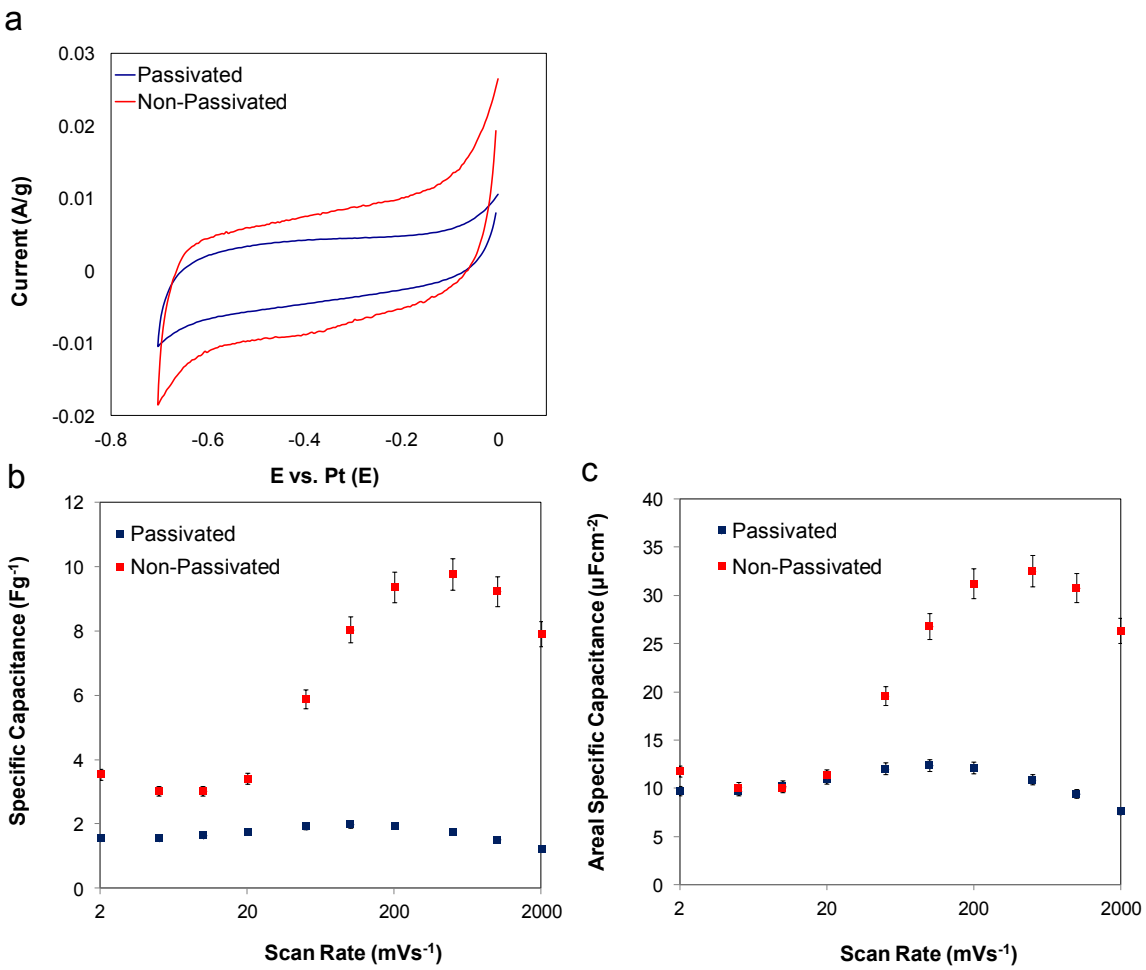

Figure 5.17: (a) Cyclic voltammograms (scan rate = 2 mV s^{-1}) and (b) specific capacitances, and (c) areal specific capacitances of passivated (blue) and non-passivated (red) NbC in 0.1 mol dm^{-3} H_2SO_4. The 2nd scan is shown here.

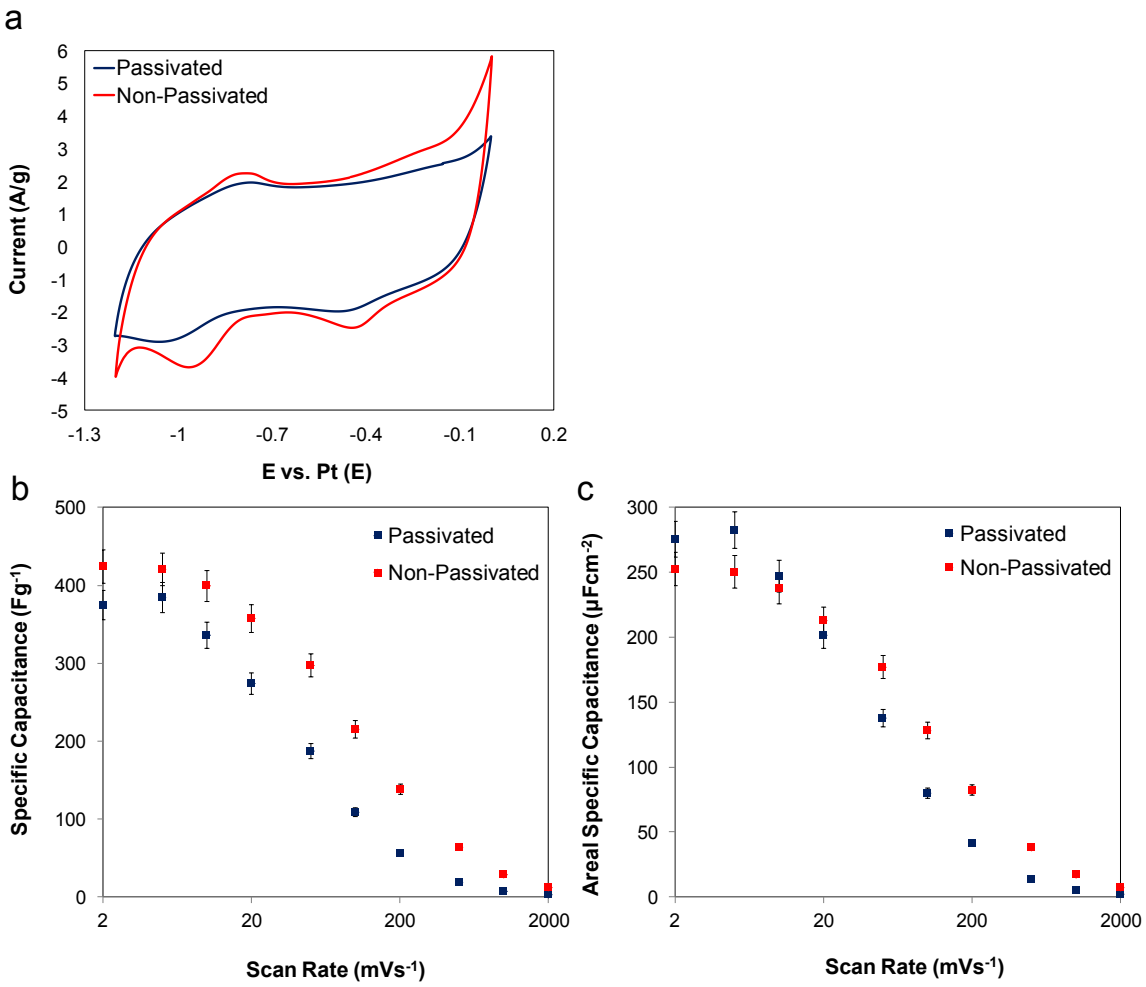

Figure 5.18: (a) Cyclic voltammograms (scan rate = 2 mV s^{-1}), and (b) specific capacitances, and (c) areal specific capacitances of passivated (blue) and non-passivated (red) Mo_2N in 0.1 mol dm^{-3} H_2SO_4. The 2nd scan is shown here.

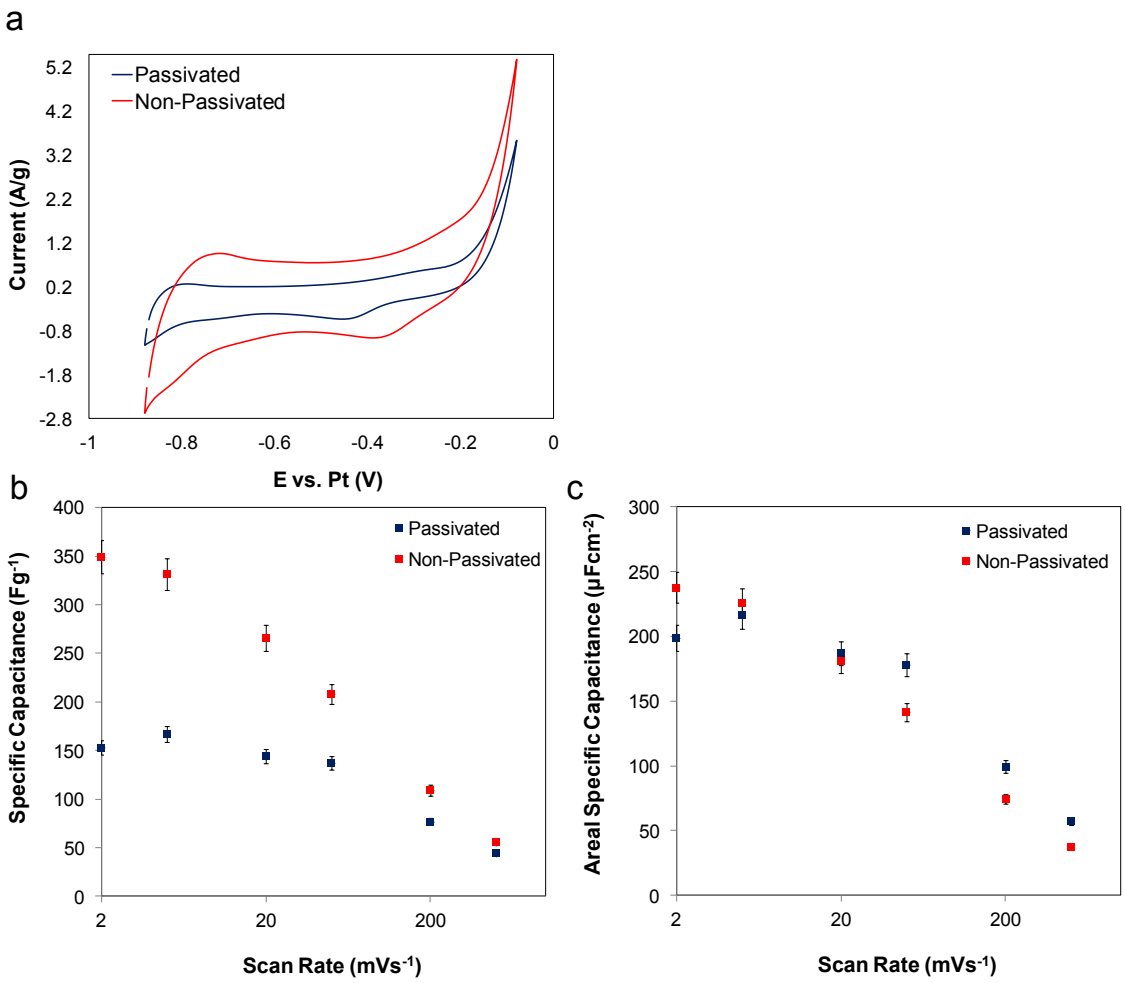

Figure 5.19: (a) Cyclic voltammograms (scan rate = 2 mV s^{-1}), and (b) specific capacitances, and (c) areal specific capacitances of passivated (blue) and non-passivated (red) (α+β)-Mo_2C in 0.1 mol dm^{-3} H_2SO_4. The 2nd scan is shown here.

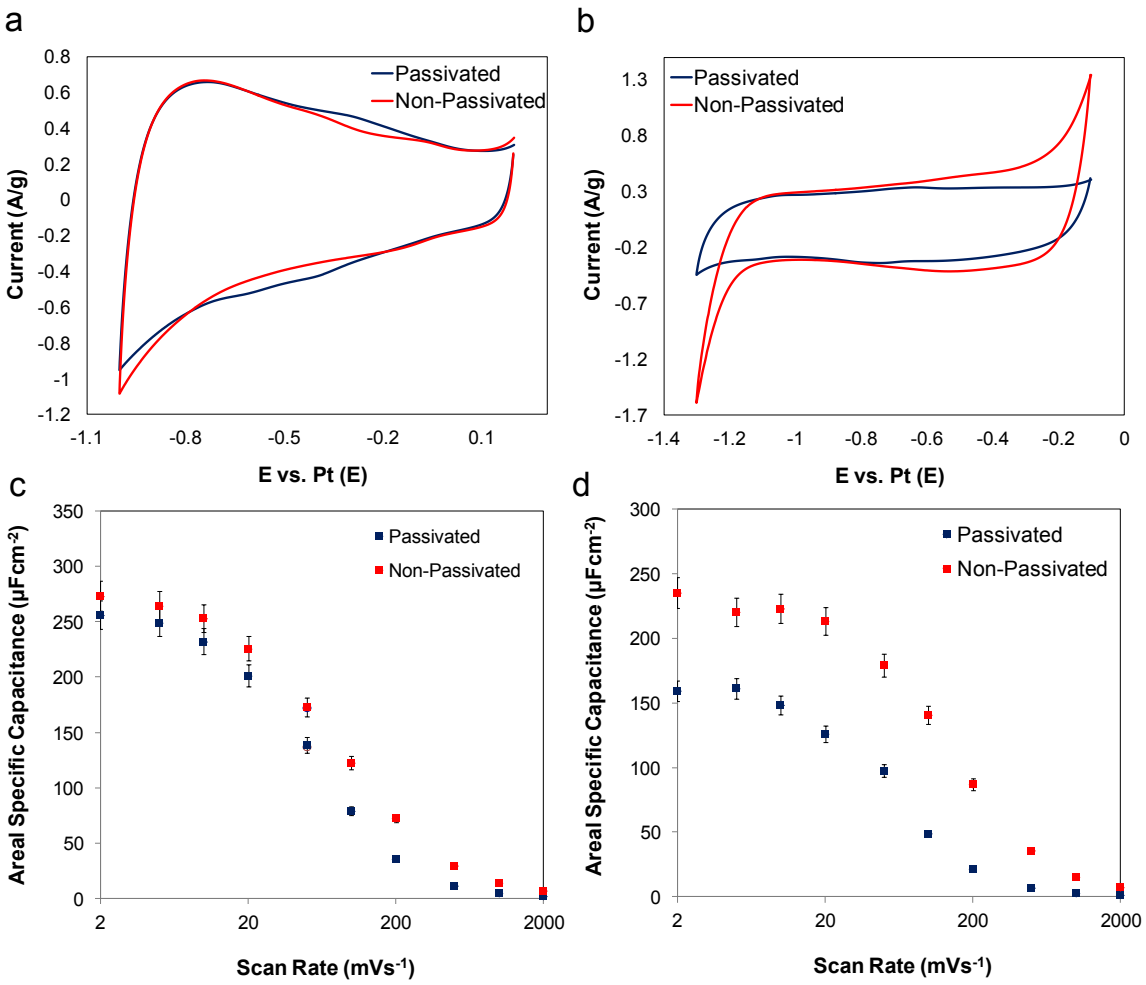

Figure 5.20: (a), (b) Cyclic voltammograms (scan rate = 2 mV s^{-1}), and (c), (d) areal specific capacitances of passivated (blue) and non-passivated (red) W_2N in 0.1 mol dm^{-3} H_2SO_4 (left) and in 0.1 mol dm^{-3} KOH (right). The 2nd scan is shown here.

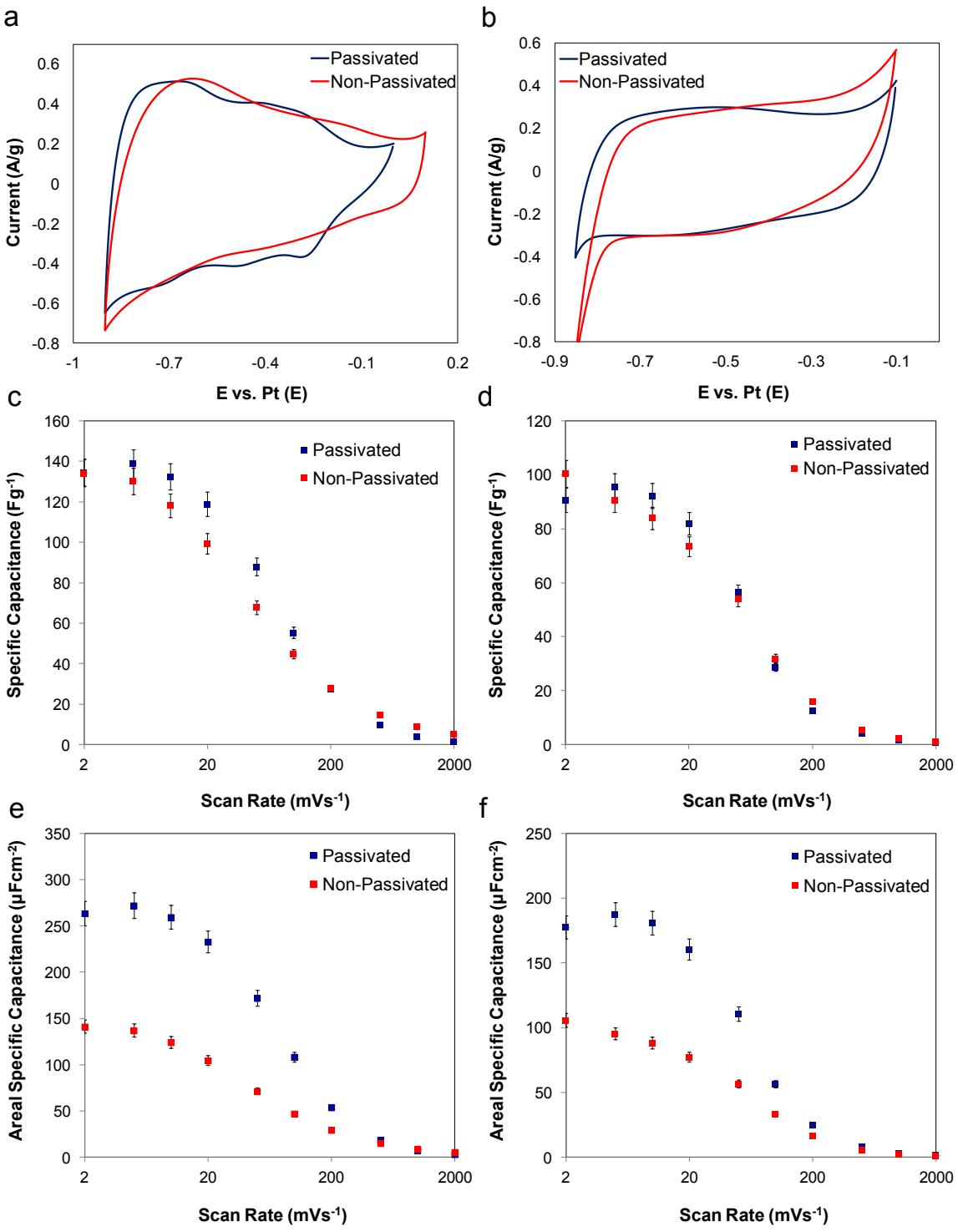

Figure 5.21: (a), (b) Cyclic voltammograms (scan rate = 2 mV s^{-1}), and (c), (b) specific capacitances, and (e), (d) areal specific capacitances of passivated (blue) and non-passivated (red) WC_{1-x} in 0.1 mol dm^{-3} H_2SO_4 (left) and in 0.1 mol dm^{-3} KOH (right). The 2nd scan is shown here.

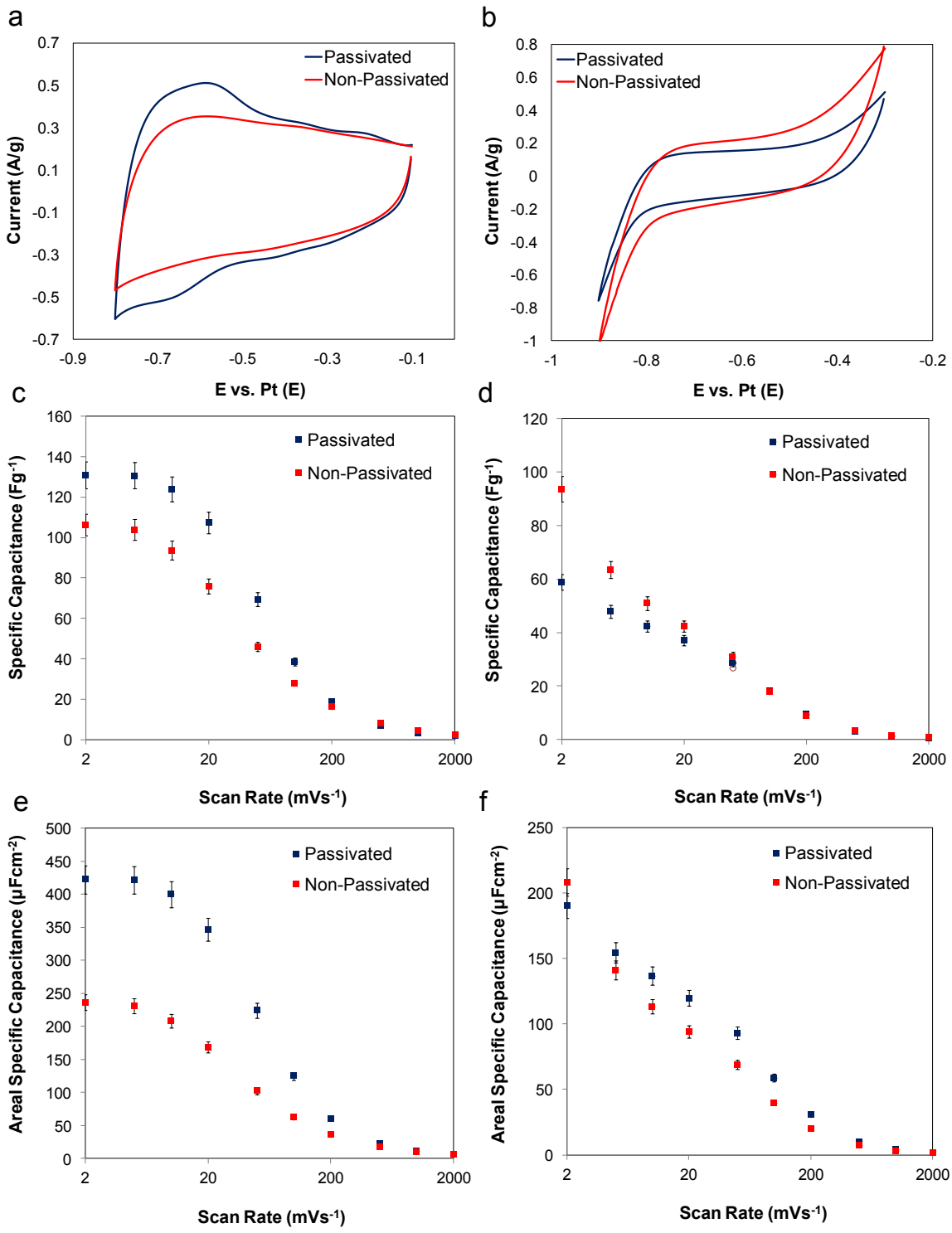

Figure 5.22: (a), (b) Cyclic voltammograms (scan rate = 2 mV s^{-1}), and (c), (d) specific capacitances, and (e), (f) areal specific capacitances of passivated (blue) and non-passivated (red) W_2C in 0.1 mol dm^{-3} H_2SO_4 (left) and in 0.1 mol dm^{-3} KOH (right). The 2^{nd} scan is shown here.

5.4. Conclusions

The presence of a thin oxide passivation layer had a profound effect on the surface areas, electrochemical stabilities and pseudocapacitive charge storage capacities of high-surface area Ti, V, Nb, Mo W-based carbide and nitride materials. For many of the materials, the physical and electrochemical properties were significantly improved. These enhancements were the result of the removal of oxides from surfaces of the materials, allowing greater access of the electrolyte ions into the pores of the materials. The increased surface area resulted in increased capacitance. Since the energy density of a supercapacitor material is a function of the voltage window and capacitance, findings from this work can be used in the design of carbide and nitride-based supercapacitor electrode materials that exhibit superior energy densities.

5.5. References

1. P. Pande, Investigation of Charge-Storage Mechanisms of Early-Transition-Metal Nitrides and Carbides as Electrodes for Electrochemical Capacitors, PhD Thesis, University of Michigan, (2013).
2. A. Trunschke, Modern Methods in Heterogeneous Catalysis Research: Surface Area and Pore Size Determination, Max Planck Society, (2013).
3. R. Brdička, Grundlagen der physikalischen Chemie, Deutscher Verlag der Wissenschaften, Berlin (1982).
4. P. W. Atkins, J. de Paula, Physikalische Chemie, Wiley-VCH, Weinheim, (2013).
5. G. Wedler, H. J. Freund, Lehrbuch der Physikalischen Chemie, Wiley-VCH, (2012).
6. S. Lowell, J. E. Shields, M. A. Thomas, M. Thommes, Characterization of Porous Solids and Powders: Surface Area, Pore Size and Density, Kluwer Academic Publisher, Dordrecht, (2004), Springer, (2006).
7. G. Ertl, H. Knözinger, J. Weitkamp (Eds.), Handbook of Heterogeneous Catalysis, VCH, Weinheim, 5 (1997).
8. F. Schüth, K. S. W. Sing, J. Weitkamp (Eds.), Handbook of Porous Solids, Wiley VCH, Weinheim, 1 (2002).
9. B. E. Conway, J. Electrochem. Soc., 6 (1991) 138.
10. J. P. Xheng and T. R. Jow, J. Electrochem. Soc., 1 (1995) 142.
11. P. Simon, Y. Gogotsi, Nature Materials, 7 (2008) 845.
12. B. E. Conway, Electrochemical Supercapacitors, Kluwer Academic/ Plenum Publishers, (1999).

13. D. W. Choi, G. E. Blomgren, P. N. Kumta, Adv. Mater., 18 (2006) 1178.

14. P. Pande, P. Rasmussen, L. Thompson, J. Power Sources, 207 (2012) 212-215.

15. D. Choi, P. N. Kumta, J. Am. Ceram. Soc., 94, 8 (2011) 2371.

16. T. C. Liu, W. G. Pell, B. E. Conway, J. Electrochem. Soc., 145 (6) (1998) 1882.

17. M. R. Wixom, D. J. Tarnowski, J. M. Parker, J. Q. Lee, P. L. Chen, I. Song, L. T. Thompson, Mat. Res. Soc. Symp. Proc., 496 (1998) 643.

18. M. Toupin, T. Brousse, D. Bélanger, Chem. Mater., 16 (16) (2004) 3184.

19. R. L. Porto, R. Frappier, J.B. Ducros, C. Aucher, H. Mosqueda, S. Chenu, B. Chavillon, F. Tessier, F. Cheviré, T. Brousse, Electrochimica Acta 82 (2012) 257-262.

20. M. C. Weidman, D. V. Elposito, I. J. Hsu, J. G. Chen, J. Electrochem Soc., 12 (2010) 157-179.

21. M. Pourbaix, Atlas of Electrochemical Equilibria in Aqueous Solutions, National Association of Corrosion Engineers, Houston, TX, (1974).

22. A. Djire, O. Ajenifujah, A. Sleightholme, P. Rasmussen, L. T. Thompson, J. Power Sources, 207 (2015) 212-215.

23. O. Kartachova, Y. Chen, R. Jones, Y. Chen, H. Zhang, A. M. Glushenkov, J. Mater. Chem. A., 2 (2014) 12940-12951.

24. A. M. Glushenkov, D. Hulicova, D. Llewellyn, G. Q. Liu, Y. Chen, Chem. Mater., 22 (2010) 914.

Chapter 6

Effect of Electrolyte

6.1. Introduction

Given findings regarding the storage mechanism, we hypothesized that protic, non-aqueous electrolytes would enable increased energy densities, given the higher operating voltages afforded by non-aqueous electrolytes. This chapter describes the behavior of carbides and nitrides in protic ionic liquid (PIL) electrolytes. Results in PIL electrolytes are compared to those for aqueous electrolytes. Cyclic voltammetry (CV) was used to determine the stable cell voltage as well as the specific capacitance in each electrolyte. The equivalent series resistance (ESR) of each system was determined using electrochemical impedance spectroscopy (EIS). Energy and power densities were calculated for the materials based on the combined results from CV and EIS.

The characteristic shapes of the voltammograms of the materials in protic electrolytes were similar to those obtained in aqueous electrolytes, showing redox peaks associated with pseudocapacitance. Vanadium and titanium nitrides were the most promising materials. In protic ionic liquid electrolytes the VN and TiN materials yielded large pseudocapacitances across 1.7 V and ~2.0 V windows, respectively. The increase in the voltage window afforded by PIL electrolytes resulted in a three- to four-fold increase in the energy density while maintaining a power density similar to that of aqueous systems. These findings are of interest for the development of carbide and nitride-based

electrochemical capacitors with increased energy densities compared to those using aqueous electrolytes.

6.2. Experimental Methods

6.2.1. Electrolytes

The electrolytic medium for the aqueous system was 0.1 mol dm^{-3} H_2SO_4. These solutions were prepared using ultrapure water (18 MΩ cm, Millipore Milli-Q Advantage A10). The electrolytic medium for the protic ionic liquid was a mixture of 2-picoline, a base, and trifluoroacetic acid (99.99% Sigma Aldrich). A base:acid molar composition of 1:2 was chosen because it has good ionic conductivity (9.07 $mS.cm^{-1}$ at 27.0 °C) compared to 1:1 molar composition (4.73 $mS.cm^{-1}$ at 27.0 °C) [1]. The preparation of the PIL electrolytes involved the slow addition of trifluoroacetic acid into 2-picoline in order to reach the desired molar composition at room temperature, with stirring. In order to eliminate traces of water either from the starting materials or from atmosphere, the resulting mixture was heated at 85 °C for 48 h under vacuum [1]. The ionic liquid samples were kept sealed in vials and transferred to the glove box for electrochemical measurements.

6.2.2. Materials

Carbides and nitrides of Ti, V, Nb, Mo and W metals were synthesized via the temperature-programmed reaction method as discussed in chapter two. Details regarding the synthesis of these materials are reported in chapter two. After synthesis, the materials were quenched to room temperature in the reactant gas and then passivated using a flowing mixture of 1% O_2 and He (99.999%, Cryogenic Gases).

6.2.3. Electrode Preparation

Disc electrodes were prepared by coating a slurry containing 92% of the active material, 5% carbon black (Super P Li) and 3% polyvinylidene fluoride (Kynar, Arkema) in N-methyl-2-pyrrolidone (99.95%, Alfa Aesar) solvent onto a titanium foil (99.7%, Aldrich). The electrodes were dried under vacuum at 80 °C for 8 hours. The mass of the active material was determined by subtracting the mass of the Ti substrate from the mass of the coated electrode (Ti and active material). Approximately 3 mg of active material was coated onto the substrate.

6.2.4. Characterization

6.2.4.1. Physical Characterization

Physical surface areas were measured by N_2 physisorption using the Brunauer-Emmett-Teller isotherm. Pore size distributions analysis was determined using the Barrett-Joyner-Helenda (BJH) and Horvath-Kawazoe (HK) methods. All measurements were performed using a Micromeritics ASAP 2020 analyzer. X-ray diffraction (XRD) patterns were collected using a Rigaku Miniflex diffractometer with a Cu Ka ($\lambda = 0.15404$ nm) source and filter. Crystalline phases were identified using JADE 10.0 software. Additional details regarding the physical characterization experiments are reported in chapter two.

6.2.4.2. Electrochemical Characterization

Electrochemical characterization was carried out in a three-electrode electrochemical cell (ECC-Aqu, EL-Cell FmbH, Germany). A schematic of the cell is shown in chapter three (Figure 3.1). The cell was assembled with an 18 mm diameter glass fiber separator with a thickness of 1.55 mm. An 18 mm diameter counter electrode

(Kynol activated carbon fabric ACC-507-15, sp. S. A. 1500 m^2g^{-1}, thickness 0.54 mm) was used, as in chapter three. The working electrode diameter was 16 mm, to ensure better current flow between counter and working electrodes. A Pt wire (1 mm diameter) was used as the quasi-reference electrode. To ensure that the electrodes were fully wetted, the counter electrode and separator were soaked in electrolyte overnight. Aqueous electrolytes were deaerated with nitrogen for at least 30 min before assembling the cell. All PIL experiments were performed in an argon-containing glove box. The electrochemical measurements were performed using an Autolab PGSTAT302N potentiostat.

CV was used to determine the voltage window, the total capacitance of the material, and the dependence of capacitance on the scan rate. Details regarding capacitance measurements are reported in chapter three.

EIS analysis was used to measure the equivalent series resistance. EIS measurements were performed at the open circuit voltage (OCV) for each system. A low amplitude modulation of 10 mV and a wide frequency range from 10 mHz to 100 kHz was used.

6.3. Results and Discussion

Results from XRD showed that the materials were phase-pure Ti, V, Nb, Mo and W carbides and nitrides. Physical properties including crystal structure, crystallite size, pore size and pore size distributions, and surface areas are reported in chapter two.

Figures 6.1 to 6.7 show cyclic voltammograms collected at 2 mV s^{-1} and areal specific capacitances as a function of scan rate for the carbides and nitrides in aqueous H_2SO_4 and PIL electrolytes. Typically, faradaic redox features in the voltammograms in

aqueous electrolytes are more pronounced than those in PIL electrolytes. Voltammograms for VN and TiN in the aqueous and PIL-based electrolytes show similar features (Figure 6.1 and 6.2). In both electrolytes, faradaic redox couples are observed and are attributable to successive changes in the oxidation states of vanadium and titanium by adsorption of H^+ on the VN and TiN surfaces during electrochemical cycling [2-6]. For most of these materials, wider potential windows are observed for the PIL electrolyte as compared to aqueous-based electrolyte (i.e. from 1.1 V to 2.0 V for TiN). An increase in the potential window for the PIL electrolyte suggests a suppression of the hydrogen-evolution reaction, which shows a potential shift of approximately -200 mV and -550 mV for VN and TiN materials, respectively. Additionally, the increase in the voltage windows to more positive voltages indicates the suppression of the oxygen-evolution reaction [7].

The areal specific capacitances for the carbides and nitrides decreased logarithmically with increasing scan rate in both electrolytes, consistent with pseudocapacitive charge storage mechanisms [8]. In both electrolytes, the smallest capacitance was observed at the highest scan rate (i.e. 2000 mV s^{-1}). At high scan rates, diffusion limitations reduce the accessibility of H^+ to the inner surface of the material, and consequently some pores, particularly micropores, are inaccessible [9,10]. Slightly higher capacitances were observed for the materials in aqueous-based electrolyte at high scan rates (i.e. 100 mVs^{-1}) as compared to the PIL electrolytes, owing to the higher ionic conductivity (46 mS cm^{-1} at room temperature) and lower viscosity (0.83 cp) of the aqueous electrolyte as compared to 9.07 mS cm^{-1} and 13 cp of the PIL-based electrolyte [1]. The higher ionic conductivity and lower viscosity of aqueous-based electrolyte

facilitates the mobility of H^+ into and out of the pores. Materials that have a high density of micropores, such as W- and Mo-based carbides and nitrides, experienced more difficulty in terms of ion transport in PIL electrolyte. VN and TiN exhibited similar areal specific capacitances in both electrolytes. The areal specific capacitance for VN and TiN in both electrolytes plateaued at the lowest scan rates (i.e. 2 mVs^{-1}). In general, slightly higher values were observed in PIL-based electrolytes at low scan rates for these two materials, most likely due to the higher concentration of H^+ in the PIL electrolyte (5.5 mol dm^{-3}) as compared to the aqueous electrolyte (0.2 mol dm^{-3}). Due to the superior performance in both electrolytes, VN and TiN were selected for further characterization.

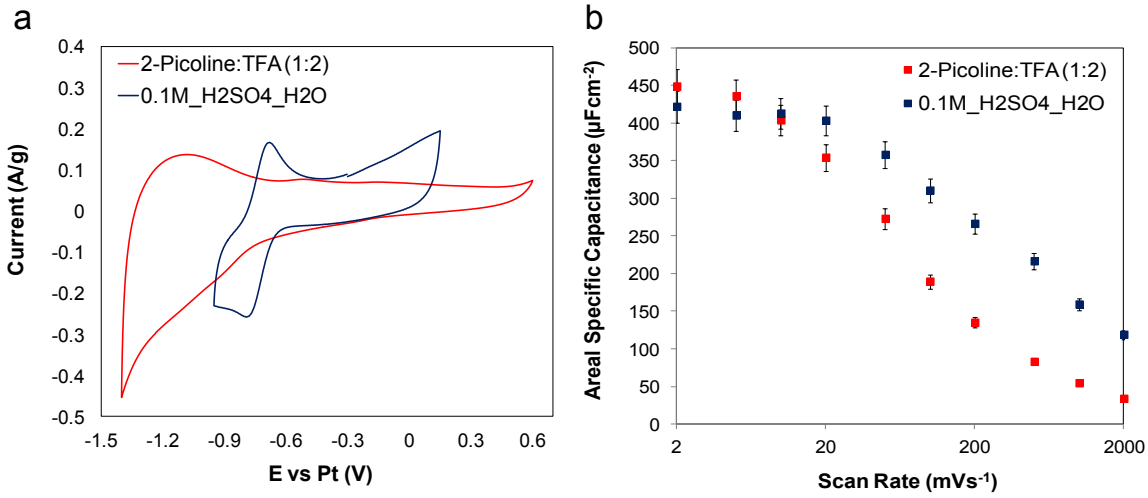

Figure 6.1: (a) Cyclic voltammograms (scan rate = 2 mV s^{-1}) and (b) areal specific capacitances of TiN in 0.1 mol dm^{-3} H_2SO_4 (blue) and in protic ionic liquid (red) electrolytes. The 2nd scan is shown here.

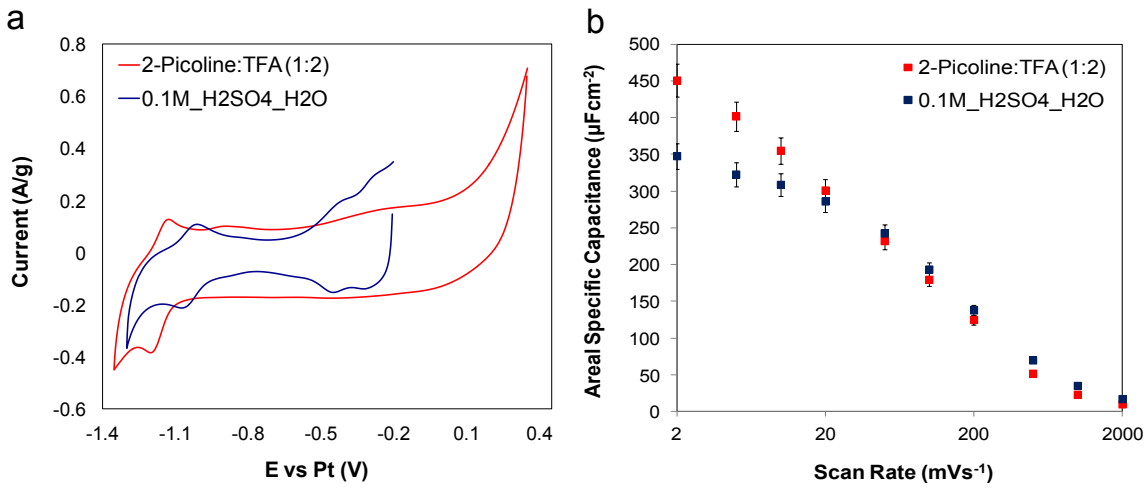

Figure 6.2: (a) Cyclic voltammograms (scan rate = 2 mV s^{-1}) and (b) areal specific capacitances of VN in 0.1 mol dm^{-3} H_2SO_4 (blue) and in protic ionic liquid (red) electrolytes. The 2nd scan is shown here.

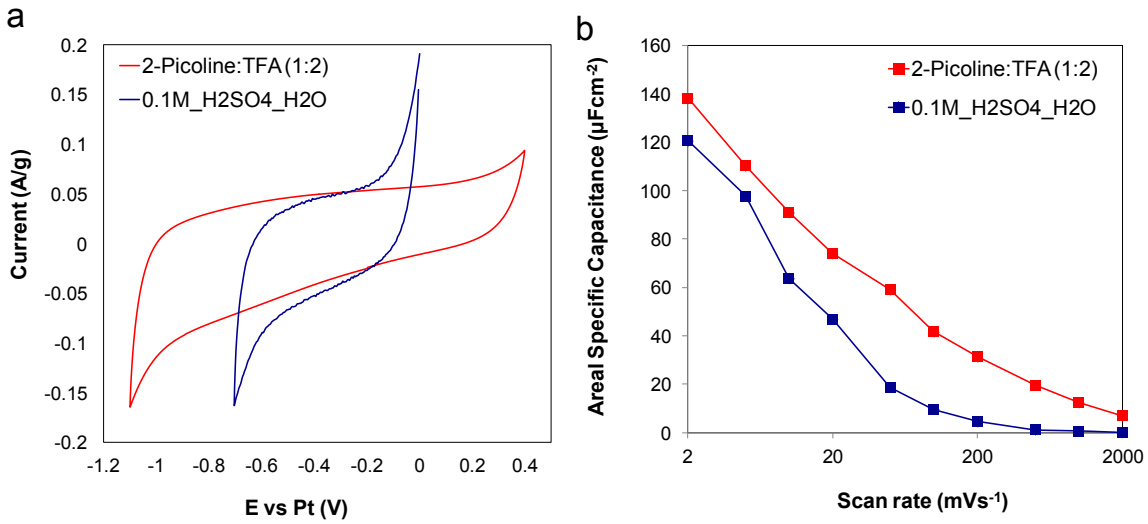

Figure 6.3: (a) Cyclic voltammograms (scan rate = 2 mV s^{-1}) and (b) areal specific capacitances of NbN in 0.1 mol dm^{-3} H_2SO_4 (blue) and in protic ionic liquid (red) electrolytes. The 2nd scan is shown here.

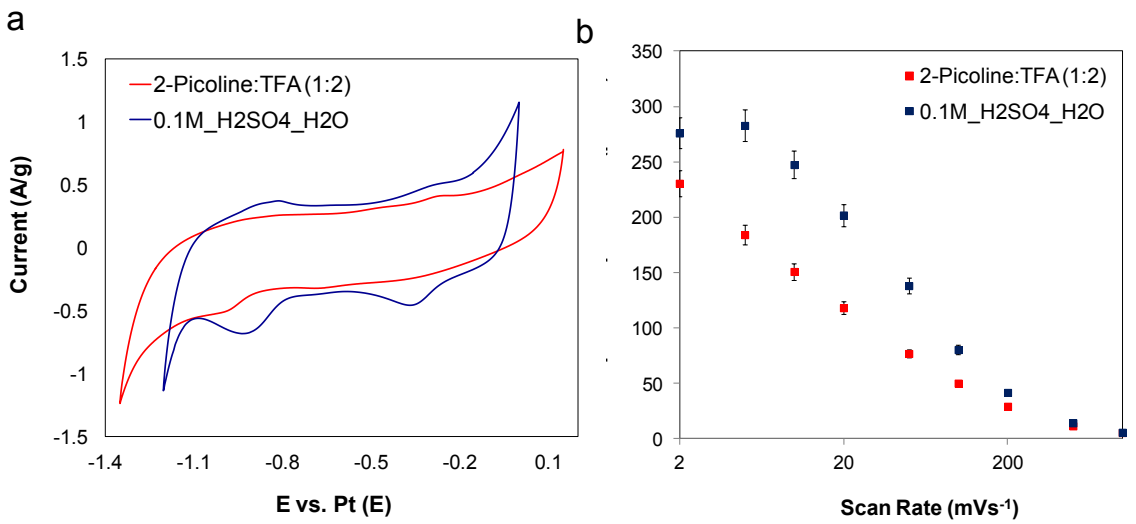

Figure 6.4: (a) Cyclic voltammograms (scan rate = 2 mV s^{-1}) and (b) areal specific capacitances of Mo_2N in 0.1 mol dm^{-3} H_2SO_4 (blue) and in protic ionic liquid (red) electrolytes. The 2nd scan is shown here.

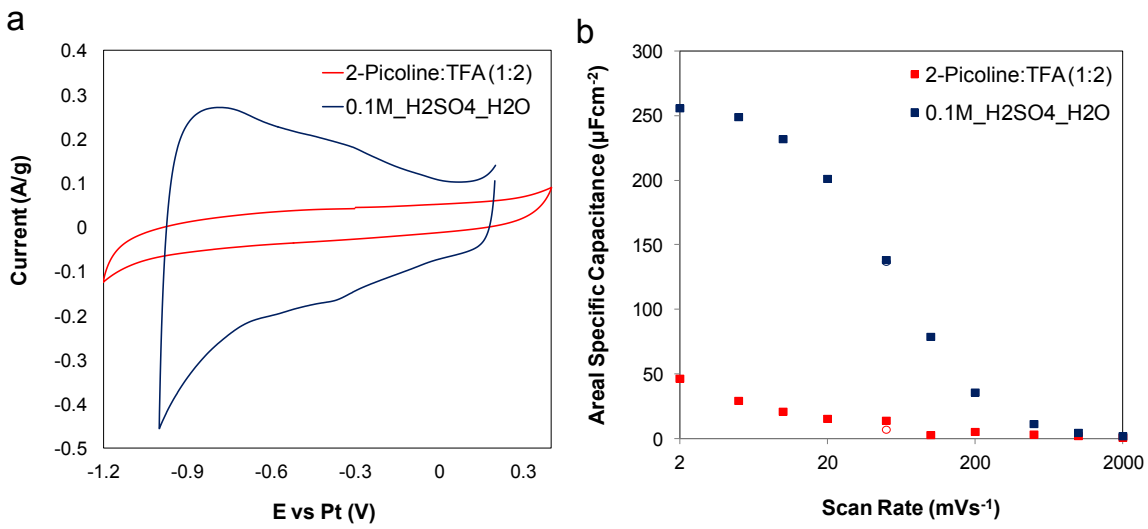

Figure 6.5: (a) Cyclic voltammograms (scan rate = 2 mV s^{-1}) and (b) areal specific capacitances of W_2N in 0.1 mol dm^{-3} H_2SO_4 (blue) and in protic ionic liquid (red) electrolytes. The 2nd scan is shown here.

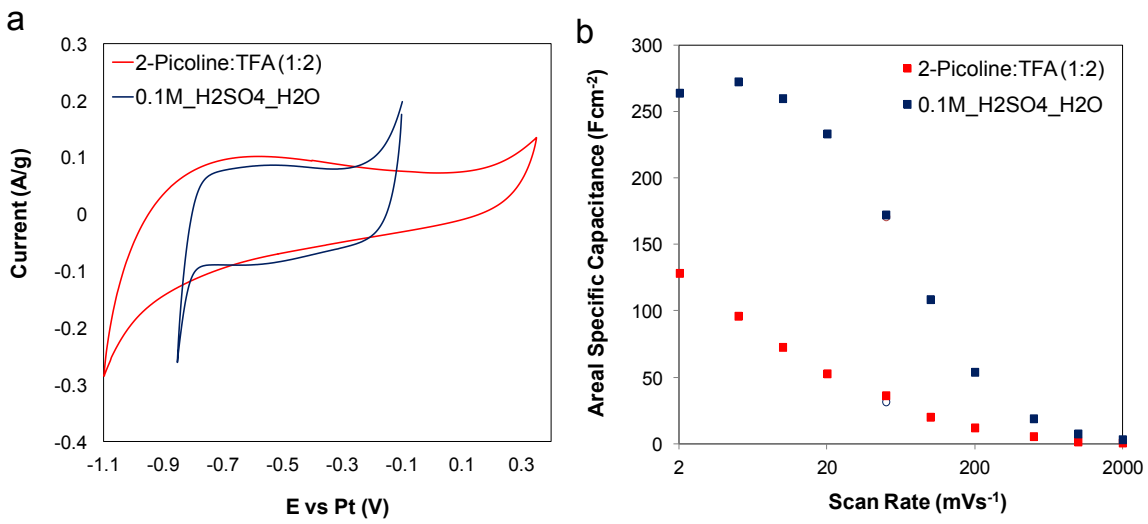

Figure 6.6: (a) Cyclic voltammograms (scan rate = 2 mV s^{-1}) and (b) areal specific capacitances of WC_{1-x} in 0.1 mol dm^{-3} H_2SO_4 (blue) and in protic ionic liquid (red) electrolytes. The 2nd scan is shown here.

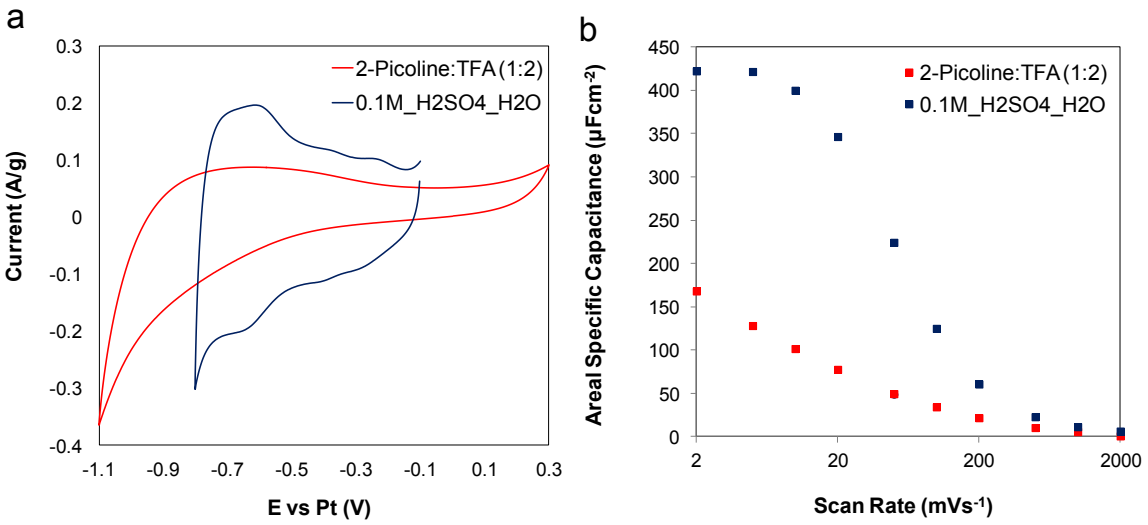

Figure 6.7: (a) Cyclic voltammograms (scan rate = 2 mV s^{-1}) and (b) areal specific capacitances of W_2C in 0.1 mol dm^{-3} H_2SO_4 (blue) and in protic ionic liquid (red) electrolytes. The 2nd scan is shown here.

The electrochemical stability of VN and TiN were assessed using CV. Figures 6.8a and 6.8b illustrate typical cyclic voltammograms for VN and TiN electrodes cycled in aqueous and PIL-based electrolytes at a scan rate of 50 mV s^{-1} for over 100 cycles. The

cyclic voltammograms overlapped, indicating materials stability in aqueous and non-aqueous PIL electrolytes.

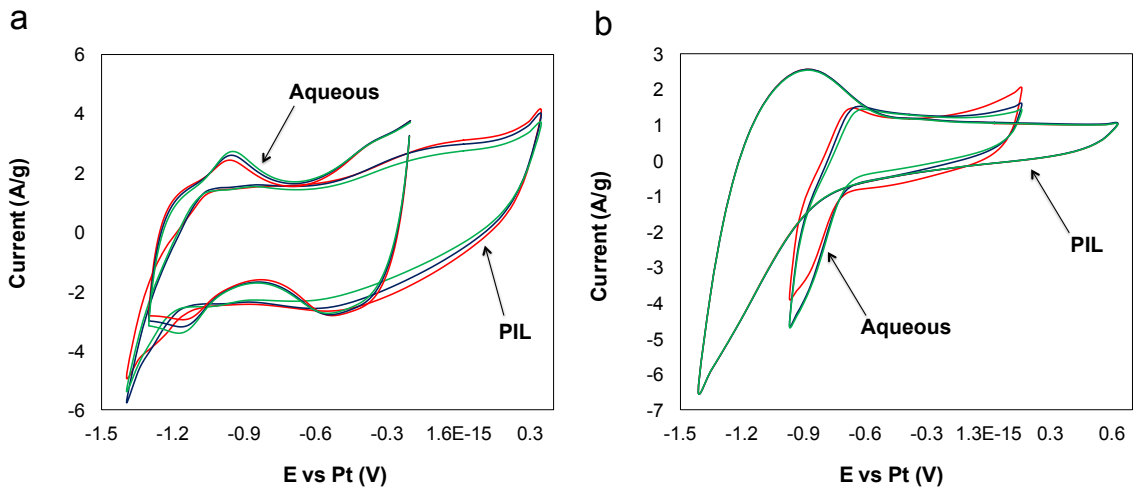

Figure 6.8: Cyclic voltammograms for (a) VN and (b) TiN in aqueous 0.1 mol dm^{-3} H_2SO_4 electrolyte and non-aqueous protic ionic liquid electrolyte, showing cycles 10^{th} (red), 50^{th} (blue), and 100^{th} (green), scan rate of 50 mVs^{-1}.

Typical impedance spectra for VN and TiN are represented in Figures 6.9a and 6.9b in the form of Nyquist plots. General features include a semi-circle (at high frequency) and a somewhat linear increase in the imaginary impedance with decreasing frequency, suggesting capacitive behavior in both aqueous and PIL-based electrolytes according to [11,12]:

$$C = \frac{-1}{2\pi f Z''} \quad (1)$$

where C is the capacitance, f is the frequency and Z'' is the imaginary impedance. The semi-circle at the high frequency was fitted to an equivalent electrochemical circuit to determine the equivalent series resistance (ESR). Table 6.1 lists the total specific capacitances, voltage windows, ESRs, and specific energy and power densities for the

VN and TiN materials in each of the electrolytes. As expected, the ESR in aqueous-based electrolytes was lower than that in PIL electrolytes for both materials.

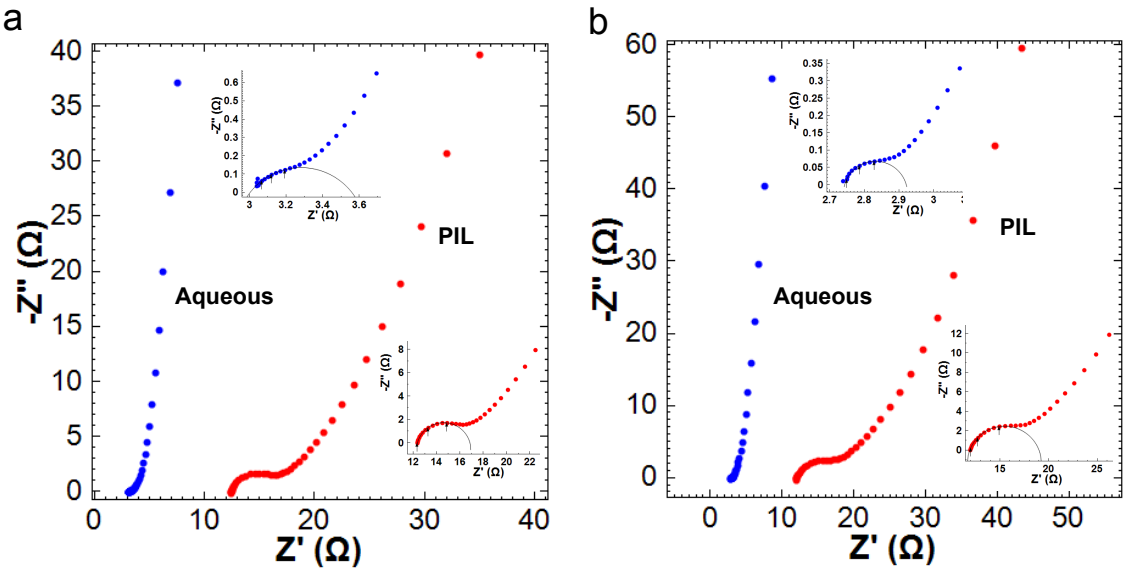

Figure 6.9: Nyquist plot for (a) VN and (b) TiN in aqueous 0.1 mol dm^{-3} H_2SO_4 electrolyte (blue) and non-aqueous protic ionic liquid electrolyte (red), electrochemical circuit fit for each system is shown in the inset.

The energy density (E) and power density (P) are key figures of merit for electrochemical capacitors and are estimated by [13,14]:

$$E = \frac{1}{2}CV^2 \quad and \quad P = \frac{1}{4 * (ESR)}V^2 \quad (2)$$

Taking into account the capacitance, resistance, and the increase in the voltage window in the PIL electrolyte compared to that in the aqueous electrolyte, a three- to four-fold increase in the energy density was observed for the nitrides (see Table 1). A slightly lower power density was observed for the VN in PIL compared to that in aqueous electrolyte. Although charge/discharge measurements were not performed on a full device, findings in this chapter show that the energy density for nitrides can be greatly

increased by using non-aqueous PIL electrolytes without a significant loss in the power density.

Table 6.1: Total capacitance, stable voltage window, and estimated energy and power densities for TiN and VN in aqueous and protic ionic liquid electrolytes.

Material	Capacitance ($F\ g^{-1}$)	Voltage Window (V)	ESR (ohm)	Energy ($Wh\ kg^{-1}$)	Power ($kW\ kg^{-1}$)
TiN (Aqueous)	76	1.1	2.8	13	85
TiN (PIL)	81	2.0	11.9	45	84
VN (Aqueous)	119	1.1	3.0	20	110
VN (PIL)	153	1.7	12.3	62	79

*Calculated energy and power densities are normalized to the mass of the active material

6.4. Conclusions

Carbides and nitrides of Ti, V, Nb, Mo and W metals were prepared and electrochemically characterized in aqueous and protic ionic liquid electrolytes. Vanadium and titanium nitrides systems were the most promising. The total specific capacitances for these materials were slightly higher in the protic ionic liquid electrolyte as compared to the aqueous electrolyte, with values ranging from 119 to 153 F g^{-1} for VN, and 76 to 81 F g^{-1} for TiN. Voltage windows of ~1.7 V and 2.0 V were observed for the VN and TiN materials respectively in the PIL electrolyte. For these materials, a three- to four-fold increase in energy densities was observed while maintaining similar power densities.

6.5. References

1. L. Mayrand-Provencher, D. Rochefort, J. Phys. Chem. C, 113 (2009) 1632-1639.
2. D. Choi, G.E. Blomgren, P.N. Kumta, Adv. Mater., 18 (2006) 1178-1182.
3. P. Pande, P.G. Rasmussen, L.T. Thompson, J. Power Sources, 207 (2012) 212-215.
4. A. Djire, O. Ajenifujah, A. S. Sleightholme, P. Rasmussen, L. T. Thompson, J. Power Sources, 207 (2015) 212-215.
5. P. Simon, Y. Gogotsi, Nat. Mater., 7 (2008) 845-854.
6. A. M. Glushenkov, D. Hulicova-Jurcakova, D. Llewellyn, G.Q. Lu, Y. Chen, Chem. Mater., 22 (2010) 914-921.
7. Y. Tomita, S. Teruya, O. Koga, Y. Hori, J. Electrochem. Soc., 147 (2000) 4164-4167.
8. B. E. Conway, J. Electrochem. Soc., 6 (1991) 138.
9. R. L. Porto, R. Frappier, J.B. Ducros, C. Aucher, H. Mosqueda, S. Chenu, B. Chavillon, F. Tessier, F. Cheviré, T. Brousse, Electrochimica Acta, 82 (2012) 257-262.
10. M. Toupin, T. Brousse, D. Belanger, Chem. Mater., 14 (2002) 3946-3952.
11. L. Andrzej, Electrochemical Impedance Spectroscopy and its Application, Kluwer Academic/Plenum Publisher, NY, (1999).
12. M. E. Orazem, Electrochemical Impedance Spectroscopy, Wiley Publisher, NY, (2008).
13. B. E. Conway, Electrochemical Supercapacitors, Plenum, New York, (1999).
14. G. Wang, L. Zhang, J. Zhang, Chem. Soc. Rev., 41 (2012) 797-828.

Chapter 7

Summary, Limitations and Future Work

7.1. Summary and Conclusions

The goal of the research described in this dissertation was to understand the charge storage mechanisms of high-surface-area early transition metal carbides and nitrides in aqueous electrolytes using a combination of various *ex-situ* and *in-situ* experimental techniques. The approach was to combine physical and electrochemical properties with surface and bulk properties in efforts to establish simple and detailed electrochemical mechanisms for the carbides and nitrides of Ti, V, Nb, Mo and W metals, that were synthesized by temperature-programmed reaction of their corresponding inexpensive oxides.

Physical properties including the phase purity, crystal structure, and crystallite size were determined using x-ray diffraction analysis. Measured surface areas range from 6 m^2g^{-1} to 144 m^2g^{-1} for VC and Mo_2N, respectively. Pore size distributions indicated the presence of primarily mesopores and micropores for most materials. The micrographs, collected using scanning electron microscopy (SEM), indicated that the materials were highly porous, consistent with the measured surface areas. In general, nitrides exhibited higher surface areas and larger micro-pore volumes when compared to the carbides. Surface analysis revealed the presence of undesirable excess carbon on the carbides,

particularly, on VC. Further improvement in the physical and surface properties of carbides will benefit from ameliorating their synthesis procedures.

Cyclic voltammetry (CV) and electrochemical impedance spectroscopy (EIS) were used to determine the operating voltage window, the total capacitance and the extent of pseudocapacitance in all the stable carbides and nitrides in aqueous electrolytes. Most materials had voltage windows above 1 V. The largest operating voltage window was observed for the VN and Mo_2N materials (~1.2 V). The total capacitance for all materials except for NbC and VC in acidic electrolyte exceeded the double layer charging, varied logarithmically with scan rate and reached a maximum value at a lower scan rate (~2 mVs^{-1}). These indicate that a significant portion of the charge storage is from a pseudocapacitive storage mechanism. The pseudocapacitance contribution in all carbides and nitrides was much higher than the double-layer capacitance. The extent of pseudocapacitance ranges from 63% for TiN to 87% for VN in acidic electrolyte. In general, the nitrides possessed higher areal specific capacitance than the carbides, in particular, VN (in KOH electrolyte) and Mo_2N (in H_2SO_4 electrolyte). The relatively lower performance observed for the carbides is due to the presence of excess carbon on their surfaces, which inhibits pseudocapacitive charge storage.

The VN and Mo_2N were further characterized in aqueous KOH and H_2SO_4 electrolytes, respectively, using *in-situ* small angle neutron scattering (SANS) and *in-situ* x-ray absorption spectroscopy (XAS). The average oxidation state of the metals (V and Mo) and changes in the bulk structure were determined while the materials were electrochemically cycled within their stable operating potential windows (~1.2 V for both). An average oxidation state change of $1e^-$ per metal (i.e. $V^{3.2+} \rightarrow V^{2.2+}$, $Mo^{3/2+} \rightarrow$

$Mo^{1/2+}$) was observed. The amount of inserted hydroxide ions (in VN) and hydrogen ions (in Mo_2N) per mole of electron transferred during charge storage was determined. For VN, there was adsorption of one OH^- per e^- during charge storage. For Mo_2N, there was consumption of two e^- per every H^+ adsorbed. A higher interaction of adsorbed OH^- with VN and H^+ with Mo_2N was observed in micropores as compared to mesopores. Charge storage mechanisms for the materials in aqueous electrolytes were established by combining results from SANS and XAS (Equations 1 and 2).

$$V^{3+}N^{3-} + OH^- \leftrightarrow V^{2+}N^{3-}(\mathrm{OH}) \quad (1)$$

$$[Mo_2^{\delta}N] + 2H^+ + 4e^- \leftrightarrow [Mo_2^{\delta}N(H)_2]^{2-} \quad (2)$$

Full utilization of the materials yields charge storage capacity in excess of 1300 Fg^{-1} (for VN) and 1500 Fg^{-1} (for Mo_2N), in 1.2 V operating voltage windows. These values exceeded those reported in the literature for any metal oxides, carbides and nitrides in aqueous media.

The oxide passivation layer from the synthesis had a profound effect on the surface areas, electrochemical stabilities and pseudocapacitive charge storage capacities of high-surface area Ti, V, Nb, Mo and W-based carbide and nitride materials. For many of the materials, the physical and electrochemical properties were significantly improved after the oxide layer was removed. The removal of the surface oxide layer increased the surface area and allowed greater accessibility of the electrolyte ions into the pores of the materials during electrochemical charge storage. This led to a significant increase in the capacitance for the carbide and nitride materials.

Given findings regarding the storage mechanism, we hypothesized that protic, non-aqueous electrolytes would enable increased energy densities, given the higher

operating voltages afforded by non-aqueous electrolytes. We were able to expand the operating voltage windows for Ti, V, Nb, Mo and W carbides and nitrides using protic ionic liquid electrolytes instead of aqueous electrolytes. Vanadium and titanium nitrides systems were the most promising. Voltage windows of ~1.7 V (for VN) and 2.0 V (for TiN) were achieved in the PIL electrolytes as compared to ~1.1 V (for both materials) in aqueous electrolytes. The total specific capacitances for these materials were slightly higher in the protic ionic liquid electrolyte as compared to the aqueous electrolyte, with values ranging from 119 to 153 Fg^{-1} for VN, and 76 to 81 Fg^{-1} for TiN. For these materials, a three- to four-fold increase in energy densities was observed (20-62 Wh kg^{-1} for VN, and 13 to 45 Wh kg^{-1} for TiN) while maintaining similar power densities.

7.2. Limitations of Current Research

The research presented in this dissertation provides a detailing understanding of the charge storage mechanisms of high-surface-area carbides and nitrides. The conclusions reached in this dissertation were based on the results from the various *ex-situ* and *in-situ* experimental techniques that we used. However, there were certain limitations associated with these techniques.

As discussed in chapter four, the XAS experiment was performed in the transmission mode. As such, only average changes in the oxidation state and the local structure of the material were detected. The discrete contributions of the surface layer versus the bulk material could not be identified. One possible approach to achieve this is to perform the XAS measurements on thin-film carbide and nitride electrodes. This would eliminate the contribution from the bulk, thus providing insights regarding the

absolute oxidation state of the metal on the electrode surface. Additionally, recent studies have shown that applying a dynamic electrochemical technique (such as CV) instead of a steady-state potential technique, in conjunction with XAS, can accurately and continuously track the oxidation state of the metal as function of charge state [1]. In principle, this method can be used with both XAS and SANS measurements to investigate the charge storage mechanism in real-time. This could eliminate ambiguous interpretations and provide more insights into the pseudocapacitive charge storage and the double layer charge storage.

Although we observed significant improvement in the physical and electrochemical properties of carbides and nitrides after the pretreatment process (as discussed in chapter five), the detailed mechanism of the pretreatment is still unclear. Information such as the surface composition, the oxide structure, and the amount of dissolved oxides are not well understood. Further experiments using x-ray photoelectron spectroscopy and inductively coupled plasma (ICP) are needed to better understand the pretreatment mechanism.

Results from chapter five indicated that native (without the oxide passivation layer) carbides and nitrides have slightly higher capacitances and wider voltage windows than passivated (with oxide passivation layer) counterparts. However, the performance was not as high as it should have been based on the results from the pretreatment study. It is possible that the native electrodes were slowly passivated over time. With careful precaution and planning, one could further investigate the physical and electrochemical properties of native carbides and nitrides and compare the results to those obtained for the pretreated and passivated counterparts.

Our results indicated that there is greater interaction of adsorbed electrolyte ions with the nitrides in micropores. The micrographs resolution (from SEM) was inadequate to visualize the pore structure. A visual observation can be helpful in better understanding the pore structures. Unfortunately most microscopic techniques provide limited information regarding the internal morphology of the pore structures. Recently, transmission electron microscopy (TEM) tomography was used to create detailed 3D visualizations of the internal nanostructure of a porous polyamide film [2]. Perhaps, a similar approach can be applied to carbides and nitrides to understand the internal pore structure, shape (i.e. slit, cylindrical, spherical) and tortuosity.

7.3. Extension of Current Research and Future Work

7.3.1. Extend Current Findings to Promising Carbides and Nitrides

In addition to VN in KOH and Mo_2N in H_2SO_4, many other systems showed promising results. For the nitrides, VN and W_2N in H_2SO_4 and TiN in both KOH and H_2SO_4 were also promising systems based on their high areal specific capacitances and wide operating voltage windows. The areal specific capacitance of VN in H_2SO_4 was ~350 μF cm^{-2} in a 1.2 V voltage window and ~260 μF cm^{-2} for W_2N in a ~1.0 V window. The areal specific capacitance of TiN in both electrolytes was above 200 μF cm^{-2} in 1.1 V (H_2SO_4) and 1.4 V (KOH) voltage windows. For the carbides, Mo and W-based were the most promising with areal specific capacitance close to ~200 μF cm^{-2} and reasonable voltage windows (~0.8 V) in both electrolytes. The voltammograms for all these materials had several redox features. These features are consistent with faradaic or pseudocapacitive charge storage processes involving fast, near-surface redox reactions of

the electrolyte ions with the electrode material [3-9]. The *in-situ* experimental techniques (i.e. XAS, SANS) and approaches discussed in this dissertation could be applied to understand the charge storage mechanism of these materials. Additionally, the *in-situ* experimental techniques can be coupled with a dynamic electrochemical measurement (i.e. CV) to continuously track the charge storage process in real-time during electrochemical charge storage.

Other carbides and nitrides that could be interesting to look at are Zr, Hf, Ta and Cr carbides and nitrides. These materials have not yet been tested for supercapacitor applications. Taking into account their high oxidation state (i.e. Cr^{+6}, Ta^{+5}), one would expect them to be electro-active for faradaic redox reactions.

7.3.2. Further Investigate Carbides and Nitrides in PIL Electrolytes

Exciting results were obtained for VN and TiN materials using pure PIL electrolyte. A two-fold increase in the voltage window was observed for the materials. Although the ionic conductivity of PIL was lower than that of aqueous electrolytes, similar capacitances were achieved in both aqueous and PIL electrolytes. A wide voltage window (~3.2 V) is expected from the PIL electrolyte [10]. However, when the voltage window was expanded beyond ~2.2 V, the PIL electrolyte showed evidence of instability (see Figure 7.1). A stable voltage window of 2.2 V was observed for the electrolyte based on repeated voltammograms (more than 100 cycles) obtained from the electrolyte using carbon black (Super PLi, from TIMCAL) as the electrode (Figure 7.2). Interestingly, we accessed more redox chemistries when we expanded the voltage window of VN beyond 2.2 V, which led to a three-fold increase in the capacitance (see Figures 7.3a and 7.3b). This corresponds to an approximately sixteen times increase in the energy density (E_{PIL} =

16*$E_{aqueous}$). However, as mentioned, the PIL electrolyte used in this dissertation was unstable beyond 2.2 V. Because of this, the high capacitance observed for the VN in 2.6 V faded after less than 100 cycles. Further development in the electrochemical performance of carbides and nitrides in protic non-aqueous electrolytes would benefit from expanding the voltage window up to the theoretical value (~3.2 V), while maintaining stability. Also, high-surface-area materials that have a significant amount of micropores (i.e. Mo- and W-based materials) exhibited low capacitances and a lack of redox chemistry when tested in PIL electrolyte (chapter six, Figures 6.4 to 6.7). As discussed in chapter six, these materials experienced more difficulty in terms of ion transport in PIL electrolyte due to the lower ionic conductivity and higher viscosity as compared to aqueous electrolytes [10]. The smaller operating voltage window observed for the PIL electrolyte used in this dissertation could be due to impurities (i.e. water) in the electrolyte. One research approach that offers ways to increase the ionic conductivity and lower the viscosity of PIL, thereby achieving high capacitance and better stability (close to the 3.2 V), involves the use of a solvent (i.e. acetonitrile, propylene carbonate). When tested in aprotic ionic liquid electrolytes with solvent, carbon electrodes exhibited high capacitances and wide stable voltage windows (~2.7 V) [11,12]. Similar approach can be applied to carbides and nitrides. Also, the preparation of the PIL electrolyte should be handled carefully to minimize impurity. Additionally, it would be interesting to study the effect of electrolyte concentration on the charge storage for the carbides and nitrides for a variety of PIL electrolytes in different solvents. This could help identify the optimum electrolyte concentration to achieve high energy and power densities.

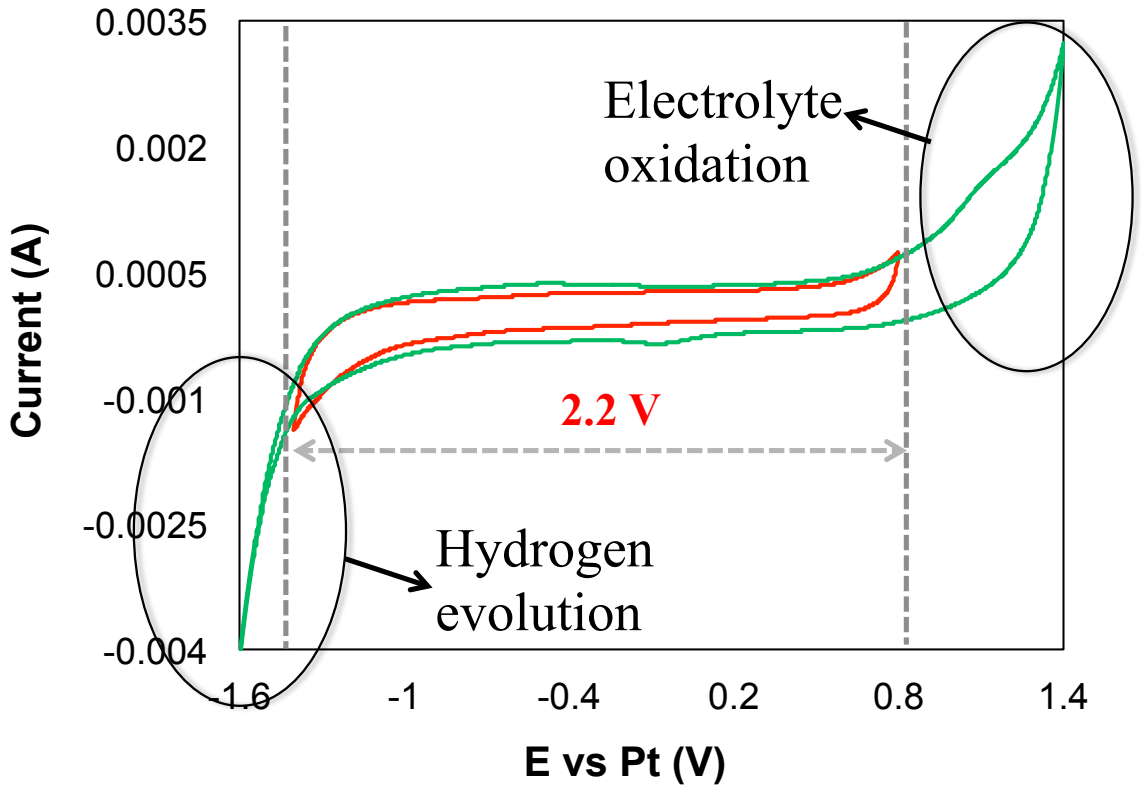

Figure 7.1: Cyclic voltammograms (Scan rate = 2 mVs^{-1}) for carbon Super PLi in 2-picoline:trifluoroacetic acid (2:1), showing stable voltage window of 2.2V for the electrolyte.

In principle, one could apply the same techniques and approaches used in the aqueous electrolytes to investigate the charge storage mechanisms of carbides and nitrides in PIL electrolytes that are rich of H^+ and OH^- ions. It is possible that key aspects involved in the charge storage mechanisms such as the extent of pseudocapacitance, the electronic structure and local environment of the metal, the relative ratio of the quantity of adsorbed active ions to electron transfer, and the location and depth of adsorption of the adsorbed ions in PIL electrolytes are different than those in aqueous electrolytes. Moreover, one could investigate native carbides and nitrides in PIL electrolytes.

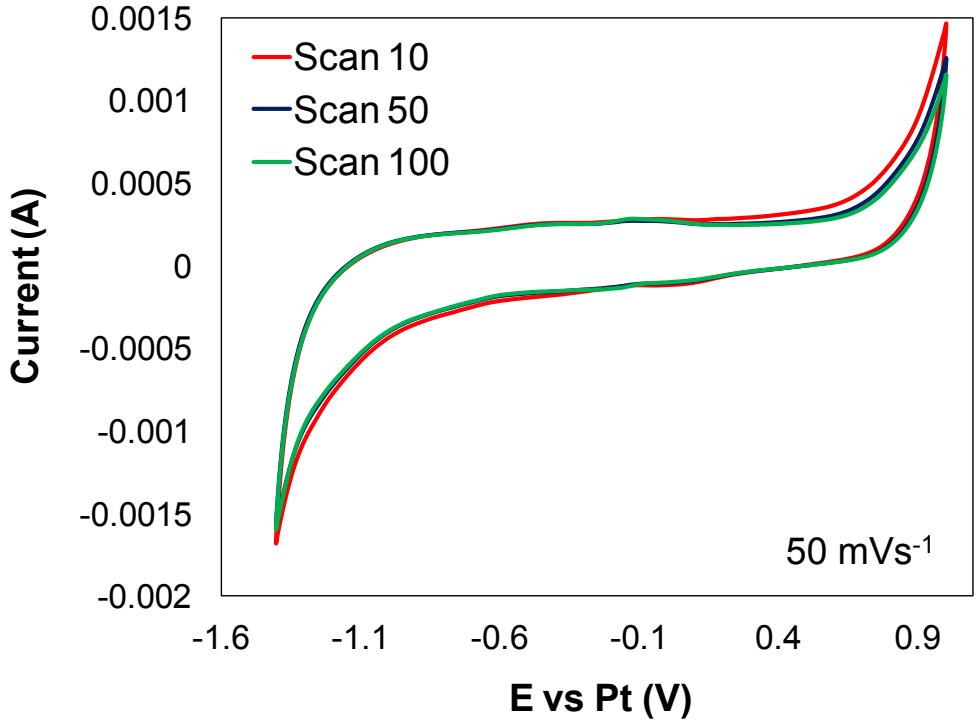

Figure 7.2 Cyclic voltammograms (Scan rate = 50 mVs^{-1}) for carbon Super PLi in 2-picoline:trifluoroacetic acid (2:1). Cycles 10^{th}, 50^{th}, and 100^{th} are shown to indicate stability of the electrolyte.

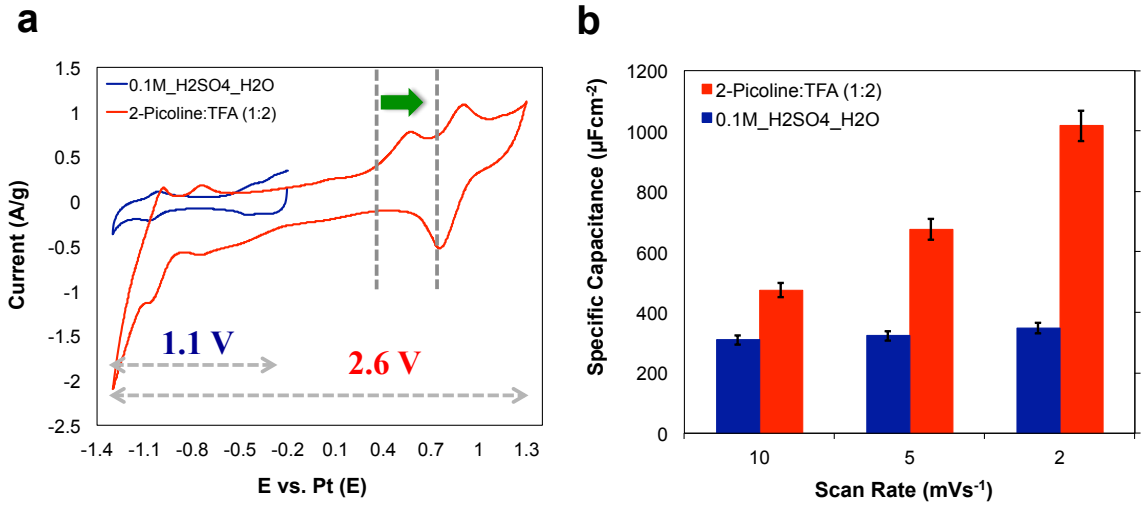

Figure 7.3: (a) Cyclic voltammograms (scan rate = 2 mVs^{-1}) and (b) capacitance for VN in aqueous and PIL electrolytes. Higher capacitance and wider voltage window are obtained in PIL medium.

7.3.3. Further Investigate the Effects of Pretreatment

Although we observed significant improvement in the physical and electrochemical properties of carbides and nitrides after the pretreatment process (as discussed in chapter five), the detailed mechanism of the pretreatment is still unclear. Information such as the surface composition, the oxide structure, and the amount of dissolved oxides are not well understood. Further experiments using Auger electron spectroscopy (AES) and inductively coupled plasma spectroscopy (ICP) are needed to further understand the pretreatment mechanism. AES with a scanning Auger nanoprobe is a surface analysis tool that can provide information representative of both x-ray photoelectron spectroscopy (XPS) and scanning electron microscopy (SEM) combined. These include the chemical composition of the material surface, the elemental mapping, and the depth profile (with ion sputtering assistance) [13]. Combined results from AES and ICP might shed light onto the nature of the electrode surface after the pretreatment, and further strengthen our understanding of the charge storage mechanisms of carbides and nitrides materials.

7.3.4. Electrode-Electrolyte Relationship

Understanding the nature of the electrochemistry at the electrode-electrolyte interface is key in moving forward with the design of supercapacitors based on carbides and nitrides with high energy and power densities. Efforts to achieve this would benefit from the following research projects.

7.3.4.1. Investigate Electrode-Electrolyte Interface

For bulk powder electrodes, it is difficult to make direct correlations between the physical properties and the electrochemical properties due to particle agglomeration [7].

Efforts to understand the relationship between the carbide/nitride and the electrolyte would benefit from results from scanning electrochemical microscopy (SECM). An SECM technique can be used to measure the local electrochemical behavior of electrode-electrolyte interfaces using an ultra-micro-electrode (UME) [15-19]. Spatially resolved electrochemical signals can be acquired by measuring the current at the UME tip as a function of precise tip position over a substrate region of interest. The two-dimensional raster scans can be compiled to generate information regarding the surface reactivity and chemical kinetics [20]. Knowledge from this study can be used to optimize the interaction of the carbide/nitride with the electrolyte to achieve high performance.

7.3.4.2. Investigate Ion-Pore Wall Interactions

While our results indicated that there is greater interaction of adsorbed electrolyte ions with the nitrides in micropores, the nature of the interaction is unclear. A detailed analysis of this interaction could strengthen our understanding of the electrode-electrolyte relationship. Efforts to understand the interaction of pore walls with the electrolyte ions for carbon materials include the work of Meunier and co-workers, who reported using density functional theory (DFT) calculations on the formation of an electric double-cylinder capacitor (EDCC) in mesopores, an electric wire-in-cylinder capacitor (EWCC) in micropores, and the formation of an electric double-layer capacitor (EDLC) in macropores [21]. These models account for the effects of the pore curvature on the interaction of the ions with the pore walls and allow correlation of the capacitance with the pore size, surface area, Debye length, electrolyte concentration and dielectric constant, and ion size [21]. Similar approaches can be applied to the carbides and nitrides

systems. These theoretical results may lend support for the systematic optimization of the properties of carbide and nitride supercapacitors through experimentation.

7.3.4.3. Investigate Ion-Bulk (Metal and Non-Metal) Interactions

Findings from chapter three suggested that nitrides have higher capacitances, wider voltage windows, and are more electrochemically stable than the carbides. Although the lower performance observed for the carbides were attributed to the excess of carbon on their surfaces, there is still need for more investigation to understand the nature and the exact cause of the differences between the nitrides and the carbides. Perhaps the non-metal is not innocent. The theoretical calculations (i.e. DFT) previously mentioned can be used to understand the nature of the interactions of the ions with the metal and the non-metal. In principle, one could also use these theoretical calculations to investigate and/or predict the insertion of cations (H^+, Li^+, Na^+, Mg^{2+}) and anions (i.e. OH^-, Cl^-, SO_4^{2-}) in the interstitial sites. These efforts could help us understand the electrochemistry at the electrode-electrolyte interface and elucidate the participation of the non-metal in the interstices to the charge storage mechanisms, thereby improving our knowledge in the design of carbide and nitride supercapacitors.

The findings presented in this dissertation enhance our understanding of the charge storage mechanism of high-surface-area early transition metal carbides and nitrides. The results and the recommendations for future research directions provided here contribute to the development of novel chemistries and provide a scientific basis for the design of high-energy density supercapacitors based on carbides and nitrides.

7.4. References

1. S. Kim, Z. Zhang, S. Wang, L. Yang, E. J. Cairns, J. E. Penner-Hahn, A. Deb, J. Phys. Chem. C, 120 (2016) 7005-7012.
2. F. Pacheco, R. Sougrat, M. Reinhard, J. O. Leckie, I. Pinnau, J. Membrane Science, 501 (2016) 33-44.
3. B. E. Conway, Electrochemical Supercapacitors, Kluwer Academic/ Plenum Publishers, (1999).
4. B. E. Conway, J. Electrochem. Soc., 6 (1991) 138.
5. M. Toupin, T. Brousse, D. Belanger, Chem. Mater., 14 (2002) 3946-3952.
6. P. Pande, P. Rasmussen, L. T. Thompson, J. Power Sources, 207 (2012) 212-215.
7. D. W. Choi, G. E. Blomgren, P. N. Kumta, Adv. Mater., 18 (2006) 1178.
8. A. Djire, O. Ajenifujah, A. Sleightholme, P. Rasmussen, L. T. Thompson, J. Power Sources, 207 (2015) 212-215.
9. P. Pande, A. Deb, A. S. Sleightholme, A. Djire, P. Rasmussen, J. Penner-Hahn, L. T. Thompson, J. Power Sources, 289 (2015) 154-159.
10. L. Mayrand-Provencher, D. Rochefort, J. Phys. Chem. C, 113 (2009) 1632-1639.
11. P. Simon, Y. Gogotsi, Nature Materials, 7 (2008) 845.
12. S. Boukhalfa, D. Gordon, L. He, Y. B. Melnichenko, N. Nitta, A. Magasinski, and G. Yushin, ACS Nano, 8 (2014) 2495-2503.
13. J. T. Grant, Auger Electron Spectroscopy: Characterization of Materials, John Wiley & Sons, (2002).
14. P. Unwin, G. Barker, S. Macpherson, "Scanning electrochemical microscopy: beyond the solid/liquid interface" Analytica Chimica Acta, 385 (1999) 223-240.

15. J. Zhang, G. Barker, P. Unwin, Electrochemistry Communications, 3 (2001) 372-378.

16. M. Mirkin, S. Peng, Analytical Chemistry, 78 (2006) 6526-6534.

17. M. Mirkin, S. Peng Sun, L. O. Francois, Physical Chemistry Chemical Physics, 9 (2007) 802-823.

18. G. Wittstock, Topics in Applied Physics, 85 (2003) 335-366.

19. A. Bard, L. K. Fan, Analytical Chemistry, 61 (2) (1989) 132-138.

20. A. Bard, Scanning Electrochemical Microscopy. New York: Marcel Dekker (2001).

21. J. Huang, B. G. Sumpter, V. Meunier, Chem. Eur. J., 14 (2008) 6614-6626.